Characterizing the Evolution of Circumstellar Systems with the Hubble Space Telescope and the Gemini Planet Imager

by

Schuyler G. Wolff

A dissertation submitted to The Johns Hopkins University in conformity with the requirements for the degree of Doctor of Philosophy.

Baltimore, Maryland

July, 2017

Abstract

The study of circumstellar disks at a variety of evolutionary stages is essential to understand the physical processes leading to planet formation. As the earliest stage of planet formation, massive, optically thick, and gas rich protoplanetary disks give information about the distribution and composition of the dust grains that will eventually coalesce into planetesimal bodies, while the later stages of the planet formation process (debris disks) demonstrate the interactions that the dust particles in disks have with the planetary bodies. The recent development of high contrast instruments designed to directly image the structures surrounding nearby stars (e.g. Gemini Planet Imager) and coronagraphic data from the Hubble Space Telescope (HST) have made detailed studies of circumstellar systems possible. As a member of the Gemini Planet Imager (GPI) exoplanet survey team, I have developed the wavelength calibration for the lenslet-based integral field spectrograph. This work has enabled some incredible science, namely the spectral characterization of one of the lowest mass extrasolar planets ever discovered via direct imaging, 51 Eridani b. The second part of this work details the observations and characterization of three

ABSTRACT

systems. I obtained GPI polarization data for the transition disk, PDS 66, which shows a double ring and gap structure and a temporally variable azimuthal asymmetry. This evolved morphology could indicate shadowing from some feature in the innermost regions of the disk, a gap-clearing planet, or a localized change in the dust properties of the disk. Millimeter continuum data of the DH Tau system places limits on the dust mass that is contributing to the strong accretion signature on the wide-separation planetary mass companion, DH Tau b. The lower than expected dust mass constrains the possible formation mechanism, with core accretion followed by dynamical scattering being the most likely. Finally, I present HST observations of the flared, edge-on protoplanetary disk ESO Hα 569. Using a covariance-based MCMC software toolkit I developed, I combine the scattered light image with a spectral energy distribution to model the key structural parameters such as the geometry (disk outer radius, vertical scale height, radial flaring profile), total mass, and dust grain properties in the disk using the radiative transfer code MCFOST.

Primary Reader: Holland Ford

Secondary Reader: Marshall Perrin

Acknowledgments

This work could not have been possible without the constant support I have received from my family. I thank my parents, Kim and Vince Wolff for protecting me from perceived limitations related to gender or circumstances and for somehow implanting in me an appreciation for education. I am forever grateful to my sisters Ciara, London, and Annika for their enduring friendship. Without their constant love and encouragement, I would not have received the first (of many, I am sure) doctoral degrees in my family.

I have had several outstanding mentors throughout the years who have fostered my passions for learning and more recently, astrophysics. First and foremost, I must thank my advisor, Marshall Perrin, for his guidance in every aspect of this work; high contrast imaging, exoplanets, disks, programming, proposal writing, career development, office politics, and work life balance. I thank Louis-Gregory Strolger, my undergraduate research advisor, for recruiting me into the field of astronomy. Thanks go to Mr. Lauderbach for following through on our unusual 'adoption' scheme. Lastly, I would like to thank Mrs. Akers and Mrs. Johnson for my enjoyment of learning.

ACKNOWLEDGMENTS

I would also like to thank the members of my thesis committee; Holland Ford, Ron Allen, Kevin Schlaufman, and Morris Swartz.

These last six years would not have been the same without the surrogate family we have constructed in Baltimore. Alex, the Davids, the Katies, Carolyn, Devin, Rachael, Duncan, Raymond, Sumit, Erini, Kirsten, Jon, Bin, Zhilei, Alice, the Mikes, Pat, Lucie, Kirill, and the rest have kept me fed, sane, alive and well. Here's to many more adventures.

It has been a privilege and a pleasure to participate in several collaborations that have enriched my research and professional life. The high contrast imaging group at the Space Telescope Science Institute has provided an incredible and supportive home for my growth in the field. Special thanks go to Elodie Choquet, John Debes, Laurent Peuyo, Anand Sivaramakrishnan, Johan Mazoyer, Christine Chen, Remi Soumer, and Dean Hines. This work would not have been possible without the support of the disk radiative transfer modeling group including Francois Mênard, Gaspard Duchêne, Christophe Pinte, Karl Stapelfeldt and Deborah Padgett. The entire Gemini Planet Imager team has been an invaluable pool of knowledge in many areas of planet formation and high contrast imaging. Furthermore, I am constantly impressed by the Gemini Planet Imager team's commitment to its junior members and sensitivity to issues related to under-represented minorites. Thanks to the exo-files graduate students (Alex Greenbaum, Jonathan Aguilar, and Bin Ren) for allowing me to ask the basic questions. I would also like to thank the referee of the paper on

the PDS 66 disk, Joel Kastner, for his advice that helped strengthen this paper and Kim Ward-Duong for helpful discussion on the disks surrounding low mass stars in the Sco Cen star forming region.

This material is based upon work supported by the National Science Foundation Graduate Research Fellowship under Grant Nos. DGE-1232825 (SGW, AZG) and DGE-1311230 (KWD) and by NASA/NNX15AD95G. Additional funding to support an extended collaboration in Grenoble, France was provided by the NSF GROW program. Any opinion, findings, and conclusions or recommendations expressed in this material are those of the authors and do not necessarily reflect the views of the National Science Foundation. Much of this work was conducted at the Gemini South Observatory, and I thank the staff who were very helpful both with observing, and with entertainment on cloudy nights. The Gemini Observatory is operated by the Association of Universities for Research in Astronomy, Inc., under a cooperative agreement with the NSF on behalf of the Gemini partnership: the National Science Foundation (United States), the National Research Council (Canada), CONICYT (Chile), the Australian Research Council (Australia), Ministério da Ciéncia, Tecnologia e Inovaçāo (Brazil), and Ministerio de Ciencia, Tecnología e Innovación Productiva (Argentina). Portions of this work were supported by the STScI Director's Discretionary Research Fund. This study is based in part on observations made with the NASA/ESA Hubble Space Telescope (program GO 12228, 12514), obtained at the Space Telescope Science Institute, which is operated by the Association of

ACKNOWLEDGMENTS

Universities for Research in Astronomy, Inc., under NASA contract NAS 526555.

This research could not have been conducted without contributions from numerous funding sources supporting both myself and my many coauthors. We acknowledge financial support of Gemini Observatory, the NSF Center for Adaptive Optics at UC Santa Cruz, the NSF (AST-0909188; AST-1211562; AST-1413718), NASA Origins (NNX11AD21G; NNX10AH31G), the University of California Office of the President (LFRP-118057), and the Dunlap Institute, University of Toronto. Portions of this work were performed under the auspices of the U.S. Department of Energy by Lawrence Livermore National Laboratory under Contract DEAC52-07NA27344 and under contract with the California Institute of Technology/Jet Propulsion Laboratory funded by NASA through the Sagan Fellowship Program executed by the NASA Exoplanet Science Institute. We also acknowledge funding from ANR of France under contract number ANR-16-CE31-0013. C.C. acknowledges support from CONICYT PAI/Concurso nacional de insercion en la academia, convocatoria 2015, Folio 79150049. M.R.S. is thankful for support from the Milenium Science Initiative, Chilean Ministry of Economy, Nucleus RC 130007 and Fondecyt (1141269). H.C. acknowledges support from the Spanish Ministerio de Economía y Competitividad under grant AYA 2014-55840-P. The authors wish to thank Karl Schuster, director of IRAM, for prompt allocation of Director observing time on the NOEMA array. MRS acknowledges support from Fondecyt (1141269) and the Millennium Nucleus RC130007 (Chilean Ministry of Economy). C. P. acknowledges funding from the Eu-

ropean Commission's 7th Framework Program (contract PERG06-GA-2009-256513) and from Agence Nationale pour la Recherche (ANR) of France under contract ANR-2010-JCJC-0504-01. F. M. acknowledges funding from ANR of France under contract number ANR-16-CE31-0013.

Contents

List of Tables

List of Figures

Chapter 1

Introduction

The field of extrasolar planets and disks has received increased interest over the past decade as indirect detection methods have provided statistically robust samples of extrasolar planets, and new high contrast instruments have produced detailed images of circumstellar disks. The study of circumstellar disks at a variety of evolutionary stages is essential to understand the physical processes leading to planet formation. As the earliest stage of planet formation, massive, optically thick, and gas-rich protoplanetary disks give information about the distribution and composition of the dust grains that will eventually coalesce into planetesimal bodies, and about the gas content which contributes the majority of the mass to Jovian planets. Debris disks, the remnants of planet formation (our own Kuiper Belt for example), serve as signposts for the dynamical history of the circumstellar system.

Circumstellar disks provide key insights into the physics inherent in star and planet

formation. At the earliest stages, the disks supply the reservoir of material through which stars form. They provide the vector for angular momentum transport, hence enabling accretion and regulating the central stars rotation, possibly via a coupling with the stellar magnetic field. The disks also provide the material and energy to launch the powerful jets observed, themselves feeding back momentum, stirring, in the molecular clouds. Most importantly, and a pressing central question of modern astrophysics since the discovery of the first exoplanet 51 Peg b in 1995, the disks also provide the environment, literally the birthplaces, for planets to form! The question is how? How do gas and dust interact in protoplanetary disks? On what timescales do disks evolve, and how does this depend on the stellar mass, metallicity and environment? How do accreting planetesimals get past the 'meter scale barrier' set by gas drag? What is the relative role of core accretion versus gravitational instability in forming Jovian planets? What role does planetary migration play in the observed distribution of extrasolar planets? The answers to these questions depend on the disks estimated lifetimes, estimated total masses and, critically, on their internal densities. These quantities can be estimated today by ambitious, massive and coherent model fitting of observations coming from the best international telescope facilities and by using tailored and optimized radiative transfer codes running on dedicated powerful computers.

The ubiquity of circumstellar disks was revealed early on by near-infrared and millimetric surveys showing that most young stars harbour a near infrared excess

(Bertout et al., 1988) and dust continuum thermal emission (Beckwith et al., 1990), both interpreted in terms of dust located in a disk and heated by the central star and/or by the accretion process. For many years the disks were studied in the infrared and at millimeter wavelengths, but without the spatial resolution necessary to reveal their detailed structure. Since the first images of a disk viewed in scattered light, dating back to only 1984 with observations of a debris disks surrounding Beta Pictoris (Smith & Terrile, 1984), scattered light images have provided the highest spatial resolution global view of disks. With the advent of ground-based adaptive optics (AO) systems and most recently, dedicated Extreme AO systems like the Gemini Planet Imager (GPI), these disks can now be characterized with great detail in scattered optical and near-infrared starlight. These ground based facilities complement coronagraphs on-board the Hubble Space Telescope's NICMOS, STIS, and ACS instruments, which have produced many beautiful, detailed images of both protoplanetary and debris disks over the last several decades. Additionally, millimeter interferometers have made substantial gains in both resolution and sensitivity over time, with key contributions from CARMA, the SMA, and most recently ALMA. Together, these data provide unique information on disk structure and dust properties.

1.1 High Contrast Techniques

Modern extreme adaptive optics systems combine several technologies to suppress light from the central star, correct for atmospheric turbulence, and to distinguish exoplanets and disk features from speckles caused by residual aberrations to the wavefront. The largest complication with direct imaging lies in the monumental levels of contrast required to resolve planets and disks within less than 100 au ($\sim 33''$ at the location of the nearest disk, Eps Eri at 3 pc) and down to a few au (≤ 0.1") of a bright, young star. For example, direct detection of Jupiter would require a contrast of 10^{-9} with respect to the flux from the sun. More attainable, are younger, self-luminous $\geq$ Jupiter mass planets that require contrast levels of $10^{-5} - 10^{-6}$ (Macintosh et al., 2006). To suppress light from the central star, a coronagraph is used. The most basic type of coronagraph is the Lyot coronagraph. A Lyot system uses a single occulting spot to mask out the light from a central star. To remove any light diffracted around this occulter, a Lyot stop is employed in the pupil plane to remove this diffracted light. The final image contains only $\sim$ 5% of the original flux from the central star (Sivaramakrishnan et al., 2001) allowing nearby faint objects to be detected. The size of the occulting spot is often given in units of resolution elements λ/D. A larger spot size limits the diffraction of the starlight but also increases the inner working angle (ie. the innermost radius for planet detection). Additionally, there is a tradeoff in the shape of the Lyot stop between the collecting area (or total flux received by the detector) and the percentage of the diffracted light that is blocked. While many

high contrast instruments use more complicated coronagraph designs, the principle remains the same.

The Gemini Planet Imager (GPI) is a high contrast instrument developed for the Gemini Observatory to study the complex circumstellar environment. GPI was initially developed at the NSF Center for Adaptive Optics starting in 2004 and saw first light in November 2013 (Macintosh et al., 2014a). After four successful commissioning runs, GPI has been placed into the Gemini proposals cycle for public use in the fall of 2014 after a successful science verification run in April, 2014. GPI was designed to be the state of the art in direct planet detection through imaging, with 10 times the sensitivity to planets over previous generation instruments. It combines an extreme adaptive optics system with two deformable mirrors to correct for atmospheric turbulence (Poyneer et al., 2014), an apodized coronagraph to block the light from the central star (Soummer et al., 2009), and an Integral Field Spectrograph (IFS; Larkin et al., 2014) to achieve a $5-\sigma$ contrast of 10^{-6} at 0.75 arcseconds and 10^{-5} at 0.35 arcseconds. The IFS features both a dispersion prism for low resolution spectroscopy and a Wollaston prism for dual polarization measurements. It is expected that GPI will be able to detect $> 15\%$ of gas giants more massive than $\sim 2\ M_J$ around stars younger than 100 Myr and nearer than 75 parsecs ranging in separation from a few to hundreds of au (Nielsen et al., 2016). When optimizing the detector real estate, a tradeoff had to be made between the spectral resolution of each lenslet and the spatial resolution or lenslet plate scale. For an 8-meter telescope, a lenslet plate scale of 14.3

mas/lenslet is necessary for Nyquist sampling at GPI's shortest operating wavelength of 0.9 μm. The relatively low spectral resolution of GPI allows the 190 x 190 required lenslet spectra to fit on the detector while providing enough detail to distinguish between planetary atmospheric models. Furthermore, 'speckles' or wavefront errors vary in size and location with wavelength. As you step from one wavelength channel to another the speckles will move radially with wavelength while the planet candidate will remain stationary increasing our likelihood of detection.

While the direct imaging technique can't match the large exoplanet statistics produced by indirect detection methods (e.g. radial velocity and transits), it provides unmatched capabilities for spectroscopy of planets over a wide range of wavelengths and temperatures. Direct imaging complements the parameter space probed by these indirect detection methods, neither of which are sensitive to wide separation ($> 3-5$ au) planets. Radial velocity (RV) surveys use high precision stellar spectroscopy to detect variations in the locations of spectral lines caused by the motion of the planet due to the gravitational influence of its host star. Consequently, the RV method is sensitive to only the most massive planets and provides only a lower limit on the planet mass. The transit method uses precise photometry to observe the drop in brightness of the central star as a planet passes in front of it blocking the light. While transits allow for planetary spectroscopy in favorable cases, the sample is biased strongly towards hot irradiated planets at small orbital separations and requires much longer integration times. To gain an understanding of the full population of

extrasolar planets, information provided by all detection methods must be combined to understand both the demographics of planetary systems and the characteristics of exoplanetary atmospheres.

1.2 Evolutionary Stages of Circumstellar Disks

As early as the 1700's it was thought that the solar system was formed as a nebula collapsed into a disk with a central bulge, forming the sun surrounded by rings of material that eventually coalesced into planets (Kant, 1755). Generally, the gravitational collapse of dense regions in molecular clouds of gas and dust form protostars over a few millions of years. The leftover material surrounding the protostar (with some initial net angular momentum) collapses into a circumstellar disk and slowly accretes onto the star. As the radius of the surrounding nebula decreases, conservation of angular momentum forces the material to rotate more quickly and eventually flatten out into a circumstellar disk. The protostar phase is fairly short lived ($\approx$ 100,000 yrs.) and ends as Hydrogen fusion begins in the core and the star approaches the main sequence.

Most disks around young low- and intermediate-mass stars fall into one of two categories on the basis of their gross observational properties. Protoplanetary disks are optically thick at visible, near- and mid-infrared wavelengths, and are rich in molecu-

lar gas. Debris disks are optically thin at optical and near-infrared wavelengths, have only trace quantities of gas, and are found in older systems. In between, transition disks are found. These are disks where the gas content has largely diminished but not yet vanished and where a large central inner hole, several AU across, is found in the central region, leaving a clear signature in the spectral energy distribution, with a lack of near-infrared excess.

Our current understanding of the evolution of dust in these observational categories correspond to very distinct phases. During the few million year lifetimes of protoplanetary disks (e.g. Haisch et al., 2001), they undergo radical changes in their composition and structure. Initially surrounded by an optically thick disk of gas and dust supposedly of interstellar composition, (classified as class II systems, and often correlated with strongly accreting Classical T Tauri stars or CTTS as traced by Hα emission), as the system evolves, processes such as photoevaporation, magnetospheric accretion, grain growth, and planet formation all act to remove mass (gas and small dust) from the disk. The circumstellar disks become optically thin (becoming class III type disks, analogous to Weak-lined T Tauri stars or WTTS with smaller accretion signatures) and eventually disperse entirely, leaving only dust disks produced by 2nd generation dust from protoplanetary collisions, known as debris disks. This process is not a simple homologous reduction in disk mass for a fixed disk geometry. As the disk evolves, large changes in the disk structure are expected to occur (e.g. Kenyon et al., 1996; Armitage et al., 1999). Disk evolution through magnetospheric accretion and

photoevaporation will move the inner edge of the disk to larger radii, creating disks with large inner disk holes. Additionally, one of the key theoretically predicted stages of planet formation is dust settling, whereby large grains migrate preferentially to the disk midplane, causing dust disks to become geometrically thin (Weidenschilling, 1977; Garaud et al., 2004). These phases of dust growth are hypothesized to result in the production of planetesimals, which form rocky planets and the cores of gas giant planets. Both processes leave clear observational signatures in scattered light images and the spectral energy distribution (SED) of the disks, allowing multi-wavelength infrared surveys of young stars to investigate how far along the planet-formation process young stellar objects (YSOs) in the nearest star forming regions have gone.

1.3 Observational Signatures in Circumstellar Disks

Using the spectral information provided by direct imaging techniques of circumstellar systems we can begin to not only discover but characterize these complex structures. For resolved images of young, optically thick disks, the geometry of the disk (scale height, outer radius, vertical extent) can be directly measured. The vertical extent of the disk is related to the local disk temperature and grain distributions in the disk. Polarimetric images provide information on the size, and distribution of the dust particles in a disk (Graham et al., 2007). In general, at optical wavelengths

the disk flux is dominated by scattered light, but as you go out to longer wavelengths, the disk flux becomes dominated by thermal emission from grains within the disk. At a given wavelength, only the grains roughly larger than the wavelength will emit efficiently ($a > \lambda/2\pi$). Additionally, grain size distributions generally have steep slopes meaning that there are many more small grains than large. Thus, an image of a disk at a given wavelength will be dominated by thermal emission from grain sizes roughly the same size as the observed wavelength, unless it's at a wavelength where thermal emission is negligible given the dust's temperature, such as visible light, in which case it's dominated by scattered light from grains of the appropriate size. Protoplanetary disks are optically thick leaving much of the inner disk unseen by the observer. However, at millimeter wavelengths, even protoplanetary disks become optically thin. In this case, the flux at these higher wavelengths provides a measure of the degree of grain growth. In the case of older, evolved systems with both planets and disks, observations of the presence and structure of disks can provide evidence for lower-mass planets that are not directly imageable (i.e. Neptune to Saturn mass bodies). These data can also be combined with dynamical studies to constrain the planetary masses (Chiang & Choi, 2008). By combining the spectroscopic and polarization capabilities of the Gemini Planet Imager, the disk geometries and grain sizes and compositions may be studied and combined for a large population of disks to investigate this relatively short lived but critical stage in disk evolution.

The spectral energy distribution (SED) of a star+disk provides another valuable

diagnostic tool as it places constraints on the mass and distribution of grain sizes within a disk. SEDs are generally double peaked with the optical emission dominated by the blackbody emission from the central star and thermal emission from the disk peaking at 10s to 100s of microns. For the case of the SED, the flux at a given wavelength roughly correlates to the distance from the central star. If we assume the disk radiates as a blackbody at the local disk temperature, then the SED of the disk is a combination of blackbodies over the range in disk temperatures weighted by the amount of material in each bin. The closer an annulus of the disk is to the central star, the higher the mid-plane temperature of the disk. The hotter the grains, the shorter the wavelength of the emitted light. For the optically thin case of a debris disk, the wavelength of the peak of thermal emission for the disk gives the temperature of the disk and thus the distance of the disk from the central star.

Observations of disks at different evolutionary stages allow us to track the formation of planetesimals from the primordial disk dust grains. In order to build larger bodies, the dust coming from the original molecular cloud must grow by several orders of magnitude and gas must be present for the process to occur efficiently (e.g. Dullemond & Dominik, 2005; Heng & Kenyon, 2010). As grains grow, their observational signatures will change. With smaller albedos, larger grains will result in disks with fainter surface brightnesses when seen in scattered light for example (e.g. Dullemond & Dominik, 2004, 2005). A global change in the dust size distribution will also yield a change in the shape of the spectral energy distribution. Similarly, the shape of the

silicate features is strikingly different for small and large silicate grains (Dullemond & Dominik, 2005). When viewed edge-on, these young disks provide a unique view of the vertical structure. Millimeter observations of the HH 30 (Madlener et al., 2012) and HL Tau (Pinte et al., 2016) disks show significant dust settling of the larger grains to the disk midplane with very flat surface density distributions. The HH 30 disk in particular also shows a very sharp outer radius, likely due to a radial drift of particles due to gas drag.

As the remnants of the planet formation process, debris disks hold vital clues to the physical mechanisms that formed them. Debris disk geometries can intimate embedded planets, and the grain properties within the disk serve as signposts for the chemical and dynamical history of the circumstellar environment. Like their younger counterparts, the best angular resolution for debris disks is available using advanced AO systems with coronagraphs in the NIR. Images taken at several different wavelengths in the near-infrared will better constrain the color of the scattered light and therefore the particle composition and size. In addition, polarimetric images will allow us to break the degeneracy in forward scattering between particle size and porosity, and provide information on the size, composition and porosity of the dust particles in a disk (Graham et al., 2007). Spatially resolved, low resolution spectroscopy could point to chemical signatures within the disk and could reveal radial stratification of dust grains. Unlike protoplanetary disks, debris disks are flat, and optically thin, and thus the geometries can be directly measured along

with the eccentricity of parent rings, and dust properties, which help to inform our understanding of the processing, generation, and transporting of dust grains. The rich morphologies of debris disks can elucidate the dynamical history of the circumstellar environment. Radial gaps in the disk could indicate the presence of a planet below the contrast limit of our observations, or it could point to a change in the dust particle properties, as a localized change in the grain properties would change the opacity of the disk.

For now however, a very large fraction of our knowledge of disks remains based on model fitting of the spectral energy distributions only (D'Alessio et al., 2006). The information attainable by fitting images simultaneously with spectral information, has been exploited for only a few objects (e.g., HV Tau C, HH 30, HD 61005: Duchêne et al., 2010; Madlener et al., 2012; Olofsson et al., 2016; Esposito et al., 2016). Apart from optical and near-infrared images, radio (sub)millimeter aperture synthesis images must be used to constrain the total dust mass and the radial surface density distribution, polarimetry can be used to better assess dust properties, mid-infrared thermal emission must be used to probe the intermediate region between the surface and the equatorial plane and to probe larger grain sizes, etc.

1.4 Summary of Thesis Work

My research efforts during my graduate career have focused on the high contrast imaging of planetary systems, specifically the study of extrasolar planets and circumstellar disks of various ages. Circumstellar disks are modern day alchemists. They transform dust into astronomical gold: planets. But many specifics of planet formation remain a mystery today. I am driven by several key questions: What is the structure of protoplanetary disks? Can we reproduce all observables of a disk with a single model encompassing the innermost and outermost regions, the deepest layers and the thin surface? How and where in the disk do grains grow to form planets? On what timescale? The first two chapters of this thesis describe my work in software infrastructure development for one of the most powerful high contrast imaging instruments available today, the Gemini Planet Imager. The remainder of my thesis details work I've done to characterize individual circumstellar systems.

1.4.1 Gemini Planet Imager Exoplanet Survey

The Gemini Planet Imager (GPI) is a high contrast instrument designed for Gemini South to image extrasolar planets and disks around young, nearby stars (PI: Bruce Macintosh). The GPI Exoplanet Survey (GPIES) is a little over halfway through its (890 hour) campaign to search for planets and disks around 600 young (< 0.5 Gyrs), nearby (50–70 parsecs) stars. The survey targets include spectral types A - M with

apparent magnitudes brighter than 10 mags. By pre-selecting younger stars, the surrounding planets will be brighter as they are still radiating away the internal heat from gravitational collapse, providing a more favorable contrast ratio between the planet and its host star.

I was part of the team that commissioned GPI in 2014, and am one of the senior graduate students in the GPIES consortium. I have been on 5 observing runs at Gemini South, and have provided remote data pipeline support for the majority of all runs. I am also a leading contributor to the GPI data pipeline; the entire campaign and other GPI users from across the Gemini community have benefited from my improvements to the wavelength calibration of the Integral Field Spectrograph (Wolff et al., 2014, 2016a). I developed an algorithm to fit via forward modeling the four spectral parameters (x and y position, spectral dispersion, and orientation) in the 2D IFS detector frame for each of the $\sim$35,000 lenslets, and I developed software tools to account for gravitationally-induced flexure of the IFS and automatically produce calibrations for each set of observations (Wolff et al., 2014). This approach enables measurement of spectral positions to better than 1/10th of a pixel, which can be improved by a factor of 10 with the inclusion of a quadratic dispersion function (Wolff et al., 2016a). This yields a wavelength uncertainty of $\sim$0.2 nm across all filters, aiding in precise spectral characterization of planets. Because the integral field spectrograph is GPI's primary science mode, my work in ensuring an accurate calibration for the spectrograph directly helps enable the majority of science observations with GPI.

This work is described in Chapters 2 and 3.

In its third year, our GPIES campaign has already produced some major results. Most notable has been the discovery of the planet 51 Eri b (Macintosh et al., 2015; Rajan et al., 2017) shown in Figure 1.1. It is the first exoplanet discovered in the survey, and with a mass about twice the mass of Jupiter, it is among the lowest mass directly imaged exoplanets. Early predictions for the survey yield optimistically suggested detections of 20 to 50 exoplanets with masses ranging from $1-10\,M_J$. While the campaign is far from complete, it is clear that the planet occurrence rate for wide separation, massive planets is lower than expected. Thus far we have detected only 7 exoplanets, most of which were already known (e.g. Beta Pic b, HR 8799 c and d, HD 95086 b: Chilcote et al., 2015, 2017; Ingraham et al., 2014b; De Rosa et al., 2016). Consequently, there has been ample time to conduct followup observations for each of these targets allowing for spectral characterization of young exoplanet atmospheres. Low resolution spectroscopy in the $0.9 = 2.5$ μm range in which GPI operates, provides information about the temperature structure, gas composition (e.g. methane abundance) and cloud fraction of the atmospheres (Crossfield, 2015).

For survey targets with evidence for an infrared excess, GPI's polarimetric mode is used to take a quick 'snapshot' to search for scattered light from dusty disks. GPI has produced many exciting debris disks results (e.g., HD 106906, AU Mic, HD 131835 Kalas et al., 2015; Wang et al., 2015b; Hung et al., 2015) shown in Figure 1.2. These disks cover a wide range in morphologies including the HD 106906 'needle' which

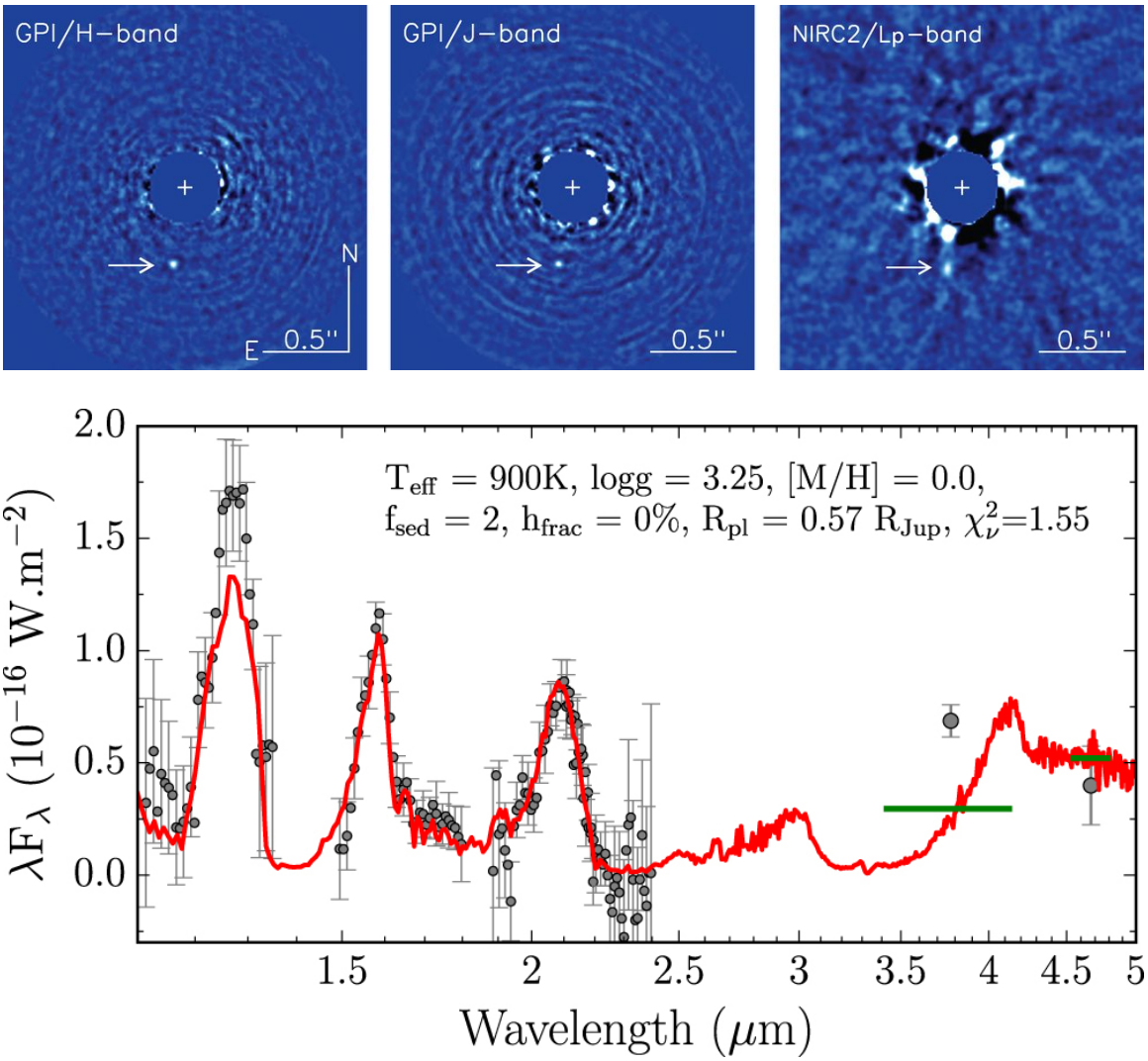

Figure 1.1 Top: PSF subtracted image for the 51 Eridani b planet via direct image with the Gemini Planet Imager in J and H-band and in Lp-band with Keck/NIRC2 from Macintosh et al. (2015). It is one of the lowest mass exoplanets ever detected via direct imaging, and the first new exoplanet of the GPIES campaign. Bottom: The spectrum of 51 Eridani b from Rajan et al. (2017). The planet is best fit by an effective temperature of $\sim$ 700 K, a surface gravity of log(g) = 3.5-4.0 dex, solar metallicity, and an atmosphere with patchy clouds. Here we show the best fit iron and silicate cloudy model in red.

could be the result of a planetary purturber, the radially moving clumps in AU Mic, and the inner clearing observed for the HD 131835 disk seen only in scattered light. I personally led a paper on the younger transitional disk PDS 66 using polarimetry data to reveal a bright inner disk component with a more diffuse disk extending to a bright outer ring (Wolff et al., 2016b). Based on the observed ring + gap structure, I placed limits on the physical mechanisms involved in shaping the disk. If the disk is optically thick, the morphology could result from a variation in the disk surface caused by either an embedded proto/planet, disk shadowing from an enhanced inner wall, or a local change in the dust properties that would effect the opacity. This work is described in Chapter 4.

1.4.2 DH Tau b Circumplanetary Disk

DH Tau is one of the few stars known to be associated with a planetary mass companion, DH Tau b, orbiting at large separation and detected by direct imaging (Itoh et al., 2005). DH Tau b is thought to be accreting based on copious Hα emission (Zhou et al., 2014). During a recent fellowship opportunity where I was a visiting student at IPAG in Grenoble for 3 months, I have estimated a circumplanetary disk mass limit for DH Tau b (Wolff et al., 2017). Using 230 GHz (1.3 mm) observations from the newly updated NOEMA interferometer at Plateau de Bure, we place constraints on the disk mass for both DH Tau b and the primary in a regime where the disks appear optically thin. We find a conservative disk mass upper limit of $0.31 M_{\oplus}$ for

DH Tau b, assuming that the disk temperature is dominated by irradiation from the central star. However, given the environment of the circumplanetary disk, variable illumination from the primary or the equilibrium temperature of the surrounding cloud would lead to even lower disk mass estimates. Planetary mass companions have the potential to offer unique insight into the early stages of extrasolar planet formation and to unveil, for the first time, the properties of circumplanetary disks. My work on DH Tau is described in Chapter 5.

1.4.3 Imaging Circumstellar Disks with Hubble

I also collaborate in studying several different sets of disks with the Hubble Space Telescope (HST), including both edge-on protoplanetary disks and older debris disks. Karl Stapelfeldt led a campaign (HST program 12514) that doubled the sample of edge-on protoplanetary disks imaged in scattered light, using the disk to occult the central star and resolve the disk vertical structure. I have led the modeling efforts for one of the 11 discovered disks, the T Tauri star ESO Hα 569 (Wolff et al. 2014, & 2017; submitted). I was able to test different models for disk structure, and found that the disks morphology matches the tapered outer disk model of Hughes et al. (2008). My modeling shows this disk appears to have an unusually high mass, which was recently reinforced with new ALMA measurements (Dunham et al. 2016). Chapter 6 presents this work.

Hubble's superb PSF stability and lower background also give it great sensitivity

for imaging faint debris disks. I'm also a contributing member of the Archival Legacy Investigation of Circumstellar Environments (ALICE) program (PI: Remi Soummer), which utilized state-of-the-art PSF subtraction methods to improve the contrast by an order of magnitude. We have obtained images of 11 disks that had never before been seen, plus new NICMOS images of 4 more disks previously imaged with other instruments (Choquet et al. 2016). My role in this project is to provide a model fitting toolkit capable of the systematic radiative transfer modeling of these disks. The radiative transfer modeling framework is described in more detail below.

1.4.4 Improving Methods for Fitting Circumstellar Disk Models to Observations

I have developed a statistically robust toolkit for deriving physical properties of circumstellar disks at various evolutionary stages from diverse datasets including spectral information, mutli-wavelength images, and polarimetry from several instruments (e.g. HST, GPI, WFIRST). My goal is to determine which set of model input parameters (disk geometry, distribution and composition of the dust particles, properties of the central star) provide the best fit to a given dataset. I employ the MCFOST Monte Carlo radiative transfer code (Pinte et al. 2006) to produce model images and spectral energy distributions for circumstellar systems. To efficiently sample parameter space, and to gain a better understanding of our uncertainties, we couple MCFOST with a

Monte Carlo Markov Chain using the emcee package (Foreman-Mackey et al. 2013). I have developed a suite of software tools in Python to interact with the observations, generate models, and calculate several 'goodness of fit' metrics to inform the MCMC iterations. This approach allows for a self-consistent and simultaneous fit to a variety of observables in order to place constraints on the physical properties (disk geometry, distribution and composition of the dust particles) of a given disk, while also rigorously assessing uncertainties in the derived properties.

A key innovation in my approach is for the first time handling covariances in the image fitting, using a Bayesian method based on the theory of Gaussian random processes (Czekala et al. 2015). Images of circumstellar disks exhibit complex structures with e.g. departures from axisymmetry and are therefore difficult to model. The covariance framework provides an advanced statistical methodology to overcome this problem, and can account for any global limitations of the model to fit the data. This enables more balanced χ^2 fitting of images and the SED simultaneously, and thereby optimizes our ability to constrain model parameters. These methods are described in more detail in Chapter 6.

A large effort has gone into making this package robust and applicable to data from different instruments (e.g. HST, GPI, WFIRST). I have made the code publicly available and it is increasingly used in several collaborations. I worked with STScI postdoc Johan Mazoyer to extend my fitting code to work with the GRATER model as well as MCFOST. I mentored Berkeley student Malena Rice to extend the code to

work with polarimetry data from GPI. Berkeley postdoc Tom Esposito and UCLA student Pauline Arriaga have now collaborated to add KLIP forward modeling, and Esposito is using my code in modeling the disk HD 35841.

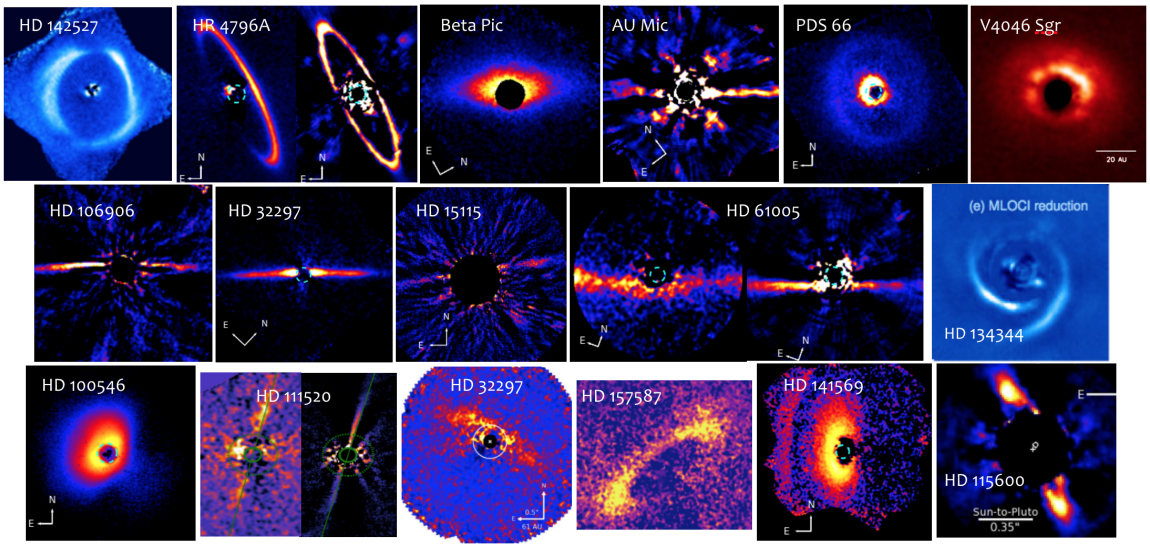

Figure 1.2 Gallery of disk detections with GPI demonstrating the incredible diversity in the morphologies of circumstellar disks. While most of these are debris disks, HD 100546 is a protoplanetary disk, and V4046 Sgr, HD 141569, HD 142527, and PDS 66 (Wolff et al., 2016b) are in the transitional phase.

Chapter 2

Gemini Planet Imager Observational Calibrations IV: Wavelength Calibration and Flexure Correction for the Integral Field Spectrograph

Abstract

We present the wavelength calibration for the lenslet-based Integral Field Spectrograph (IFS) that serves as the science instrument for the Gemini Planet Imager

(GPI). The GPI IFS features a 2.7" x 2.7" field of view and a 190 x 190 lenslet array (14.3 mas/lenslet) operating in *Y, J, H*, and *K* bands with spectral resolving power ranging from $R \sim 35$ to 78. Due to variations across the field of view, a unique wavelength solution is determined for each lenslet characterized by a two-dimensional position, the spectral dispersion, and the rotation of the spectrum with respect to the detector axes. The four free parameters are fit using a constrained Levenberg-Marquardt least-squares minimization algorithm, which compares an individual lenslet's arc lamp spectrum to a simulated arc lamp spectrum. This method enables measurement of spectral positions to better than 1/10th of a pixel on the GPI IFS detector using Gemini's facility calibration lamp unit GCAL, improving spectral extraction accuracy compared to earlier approaches. Using such wavelength calibrations we have measured how internal flexure of the spectrograph with changing zenith angle shifts spectra on the detector. We describe the methods used to compensate for these shifts when assembling datacubes from on-sky observations using GPI.

2.1 Introduction

The science instrument for the Gemini Planet Imager is the Integral Field Spectrograph (IFS) operating in the near-IR (James E. Larkin et al., 2014). The IFS uses a lenslet-based design and a HAWAII-2RG detector. The instrument has a $\sim$ 2.7" x 2.7" field of view partitioned by a $\sim$ 190 x 190 lenslet array. The GPI IFS

contains five bandpasses (*Y, J, H, K1* and *K2*) that has a spectral resolving power of $R \sim 35$ - 78 depending on the band. K band was split to allow all 36000 lenslet spectra to fit on the detector (Chilcote et al., 2014). The relatively low spectral resolution of GPI allows for the small lenslet plate scale of 14.3 mas/lenslet necessary for Nyquist sampling at the shortest wavelengths while providing enough detail to distinguish between planetary atmospheric models (McBride et al., 2011). A data reduction pipeline has been developed by the GPI team to process this complex array of micro-spectra and has been made publicly available (Perrin et al., 2014a,b).

The focus of this paper, and one of the main obstacles in calibrating the GPI IFS, is the wavelength calibration. Each reimaged lenslet has a unique position on the detector which changes with time and elevation resulting from gravitationally induced shifts due to flexure within the IFS, and distinct spectral properties. Calibrations for all Gemini South instruments are performed using the Gemini Facility Calibration Unit (GCAL; Ramsay Howat et al., 1997) that occupies one of the ports on the bottom of the Gemini Telescope. A fold mirror directs light from GCAL into GPI. The Gemini Planet Imager has no internal wavelength calibration source and must rely on GCAL for all wavelength calibrations. GCAL contains four arc line lamps, but only Ar and Xe are useful for spectral calibration for GPI; the spectral lines for the CuAr and ThAr lamps are too faint. While Xe has the advantage of fewer blended lines, the Xe lamp is 3 - 20 times fainter and requires more overhead time for calibrations. The performance of Xe and Ar lamps are discussed in Section 2.3.2.

GPI was installed at Gemini South in October 2013, and has now completed five observing runs as of May 2014 including a successful early science run. Throughout the runs, GPI has performed well and has already produced some interesting scientific results (Macintosh et al., 2014a,b). Here we present a wavelength calibration algorithm written as a module within the GPI Data Reduction Pipeline and tested using first light results of GPI. We aim to produce an accurate wavelength solution for each lenslet across the field of view for science data with the minimal amount of overhead calibration time. A description of the wavelength solution algorithm used for GPI is given in Section 2.2. Both centroid and least squared algorithms are presented. The performance and accuracy of the wavelength solution is discussed in Section 2.3. The observed flexure within the Integral Field Spectrograph is addressed in Section 2.4.

2.2 Wavelength Calibration

The Integral Field Spectrograph for GPI produces $\sim$ 36000 spectra each with a unique position and spectral properties that differ measurably across the field of view. Spectra are tightly packed on the detector plane, with a separation of approximately 4.5 pixels in the cross-dispersion direction. Furthermore, at the low resolving power of GPI the lines from the Xe and Ar lamps often appear strongly blended with few isolated peaks. All of these factors contribute to the need for a flexible and reliable wavelength calibration algorithm.

We begin with a dark subtracted and bad pixel corrected lamp image, and examine each lenslet spectrum individually. The wavelength as a function of position for a given lenslet is represented as a line and defined by Equation 2.1.

$$x = x_0 + \sin\theta \frac{\lambda - \lambda_0}{w} \quad \text{and} \quad y = y_0 - \cos\theta \frac{\lambda - \lambda_0}{w} \tag{2.1}$$

Here λ is the wavelength in microns, w is the dispersion in μm/pixel, x and y are pixel positions on the detector, λ_0 is some reference wavelength (in μm), and x_0 and y_0 gives the pixel locations for λ_0. These values are calculated individually for each lenslet and saved in a 281 x 281 x 5 datacube. These data cubes are later used to extract science spectral data into 37 wavelength channels. In the sections below, we describe the methods used to calculate these values for a given lenslet spectrum.

2.2.1 Centroiding Algorithm

The original algorithm developed for wavelength calibration for GPI worked by measuring the positions of individual spectral lines one at a time and then fitting Equation 1 to the derived positions of each line. The routine begins with a 2D detector arc lamp image, locates the brightest spectral peak in the central lenslet. For that lenslet, it measures the location of the spectral peaks for a predefined set of emission lines using a barycenter algorithm. After fitting the central lenslet, the code works its way outwards fitting each lenslet across the detector. The position of

each subsequent lenslet is estimated by calculating an offset from the prior fit lenslet based on assumed values for the separation and orientation of the lenslets. Once the positions of the individual spectra were calculated, the dispersion and tilts for each lenslet are reevaluated.

Using this method, we found that 99.9 % of spectra are detected with an accuracy better than 0.3 pixels and 80 % are detected within 0.12 pixels in lab testing of arc lamp data (Maire et al., 2012). However, we discovered that the asymmetric shape of the lenslet PSFs coupled with the spectral peaks being under Nyquist sampled led to errors in the spectral positions found using the center-of-mass centroiding algorithm. These errors result in different wavelength solutions between adjacent spectra causing the moiré pattern seen in Figure 2.1.

2.2.2 Least Squares Fitting Algorithm

In order to correct the issues with the centroiding algorithm, a new method was implemented designed to fit all the peaks in the lenslet spectrum simultaneously, and with increased sub-pixel sensitivity. The new algorithm uses a least squares fitting approach to compare an individual lenslet spectrum in the 2D detector plane to a modeled spectrum. We implement this using the mpfit2dfun IDL package written by Craig B. Markwardt, which fits parameters P for a user defined function $f(x_i, P)$ using the Levenberg-Marquardt algorithm. The Levenberg-Marquardt method is an non-linear least squares fitting technique which aims to minimize the error weighted

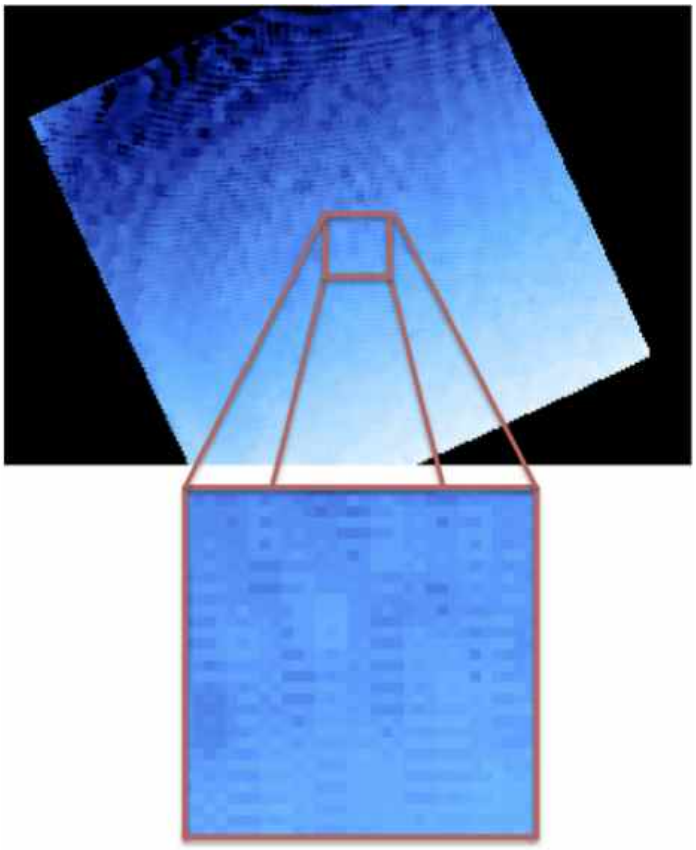

Figure 2.1 Illustration of the moiré pattern. The top image gives the dispersion of all 36000 spectra. This should be a smooth distribution, but the zoomed in region shows the moiré pattern caused by aliasing between adjacent lenslets.

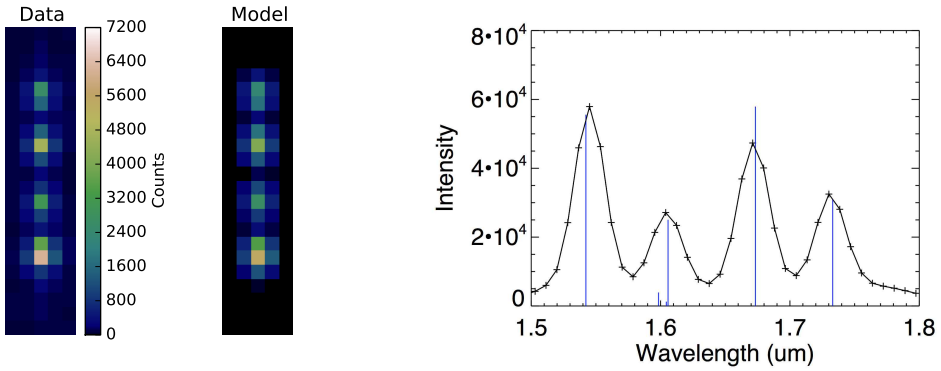

(a) H band Xe Arc Lamp

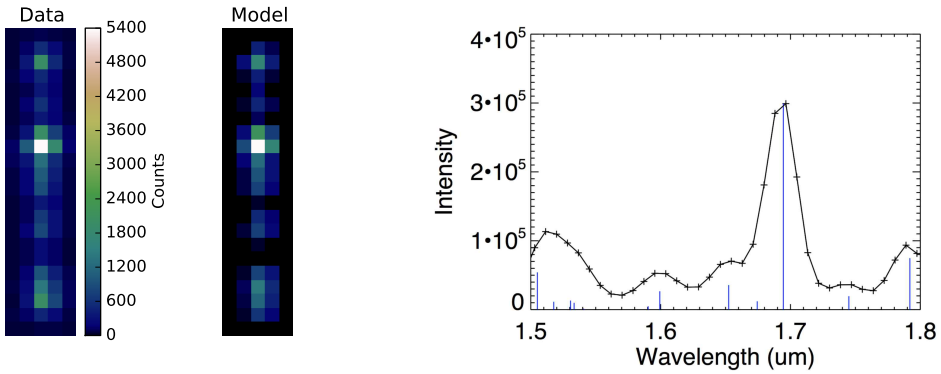

(b) H band Ar Arc Lamp

Figure 2.2 Illustration of the least squares fitting results. For each lenslet, the 2D observed spectrum and compared to a modeled lenslet spectrum. (a) H band + Xe arc lamp; On the left is an observed lenslet spectrum with best fit modeled spectrum plotted on the same scale. The spectrum used to model the Xe arc is given on the right. The GCAL emission lines are plotted in blue while the black line and points give the Xe spectrum binned to the resolution of the GPI IFS. (b) H band + Ar arc lamp; same as (b). The Ar lamp is much more difficult to fit because there are many blended emission lines and only a single sharp peak. The J band Ar arc lamp is even more difficult.

squared residuals (Levenberg, 1963; Marquardt, 1944).

$$\min_P \sum_{i=0}^{M} r_i(P)^2, \qquad \text{where } r_i(P) = \frac{y_i - f(x_i, P)}{\sigma_i} \tag{2.2}$$

In this case, the user defined function returns an array containing N Gaussian PSFs of varying peak flux and FWHM, where the number of peaks in a lenslet spectrum, N, varies with band and filter combination. For example, an H band Xe lamp exposure fits four Gaussians simultaneously at the four peak locations resolved in a lenslet spectrum shown in Figure 2.2(a). The more complicated case of an H band Ar lamp exposure is illustrated in Figure 2.2(b) with only one clear spectral peak and many blended lines. For this case, there are twelve emission lines in this band, which we approximating by fitting only the six brightest emission lines. The free parameters in the fit are the initial x_0 and y_0 values, the dispersion (w), the angle (θ) of rotation for the lenslet, the flux ratios of the peaks, and the total flux scaling for the lenslet. A previous wavelength solution is read in and used as an initial guess for the starting parameters of the fit. Constraints on acceptable values can be placed on each of the free parameters. The errors (σ_i) are given by the photon noise and weighted by the bad pixel map.

Empirically this algorithm does succeed in mitigating the problems which impacted the centroiding algorithm. Known bad pixels can be weighted to zero to avoid affecting the fits, and errors in fitting one lenslet do not propagate into erroneous starting guesses for subsequent lenslet fits. Statistical tests of the derived lenslet locations

show reduced statistical biases compared to the centroiding algorithm; specifically the histogram for position offsets is much more Gaussian and the bimodal distribution (Moiré pattern) is greatly reduced. The wavelength solution can be calculated by using the "2D Wavelength Solution" module in the GPI Data Reduction Pipeline.

2.2.3 Gaussian vs. Microlens PSFs

There has been substantial work done to determine the shape of the microlens PSFs for this instrument by GPI team members (see Ingraham et. al., these proceedings) (Ingraham et al., 2014a). High resolution microlens PSFs for each lenslet have been produced in all bands. Use of these microlens PSFs in place of the Gaussian PSFs for the wavelength solution fitting was tested. Figure 2.3 shows residual spectral images using both the Gaussian and microlens PSFs to fit an H band Xe arc lamp image. For the H band Xe spectra, we find that the empirical microlens PSFs result in $\chi^2_M = 9.1$ (Reduced χ^2 computed assuming the per-pixel noise σ_i is given by the photon noise), an improvement over the result using Gaussian PSFs of $\chi^2_G = 32.9$. However, when considering only the flux from the more brightly illuminated parts of the spectra by selecting the brightest third of the image pixels, the Gaussian PSFs provide a better fit with $\chi^2_G = 3.9$ and $\chi^2_M = 10.9$. This implies that the Gaussian PSFs provide a good fit to the cores of the emission line PSFs, though they do not fit as well the wings of the PSFs. The higher χ^2_G when computed over the full array is driven by the 68 % of less-illuminated pixels between the spectra that are less used in the spectral extraction but are well fit by the wings of the microlens PSFs. The distribution of positions, dispersions, and tilts produced in both of these wavelength solutions are roughly the same. Because we are simultaneously fitting multiple spectral peaks at once, the pixel phase errors introduced in the Gaussian PSF fits average out and the mean position of each lenslet does not vary between the two methods.

The main advantage of the microlens PSFs is an improvement in the accuracy of fitting a single peak and in distinguishing between blended peaks. For example, in Y band, the systematic error in fitting a Gaussian PSF is ~ 0.025 pixels, and for the microlens PSF it is ~ 0.0004 pixels (Ingraham et al., 2014a). This allows a more precise fit to the dispersion and tilts of the lenslets and will aid in future studies of the non-linearity of the wavelength solution. The microlens PSF implementation of the wavelength solution is not yet available in the public GPI Data Reduction Pipeline, but will be released for the 2014B observing semester.

2.2.4 Quick Wavelength Algorithm

The least squares fitting algorithm described above in Section 2.2.2 works well, but is very computationally intensive and takes several hours to run. In order to calibrate small changes of the position of lenslet spectra on the detector at a fast timescale (i.e. for corrections due to flexure in the IFS as discussed in Section 2.4), a quick wavelength solution algorithm was developed. The "Quick Wavelength Solution" GPI Pipeline primitive calculates changes in position of the lenslet spectra from an arc lamp image by fixing all parameters except the x_0 and y_0 positions for a user-selectable subset of lenslets across the field of view and computing an average shift. By default, this primitive uses a grid of lenslets spaced twenty lenslets apart in row and column. By combining information from multiple lenslets, we can achieve a good measurement of the x and y shifts with lower S/N arc lamp images to enable quick

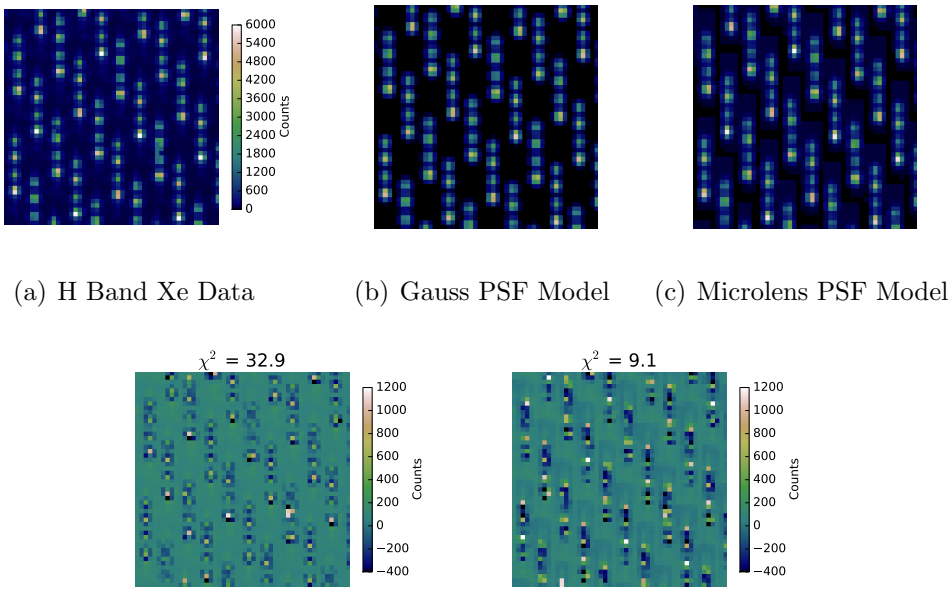

(a) H Band Xe Data (b) Gauss PSF Model (c) Microlens PSF Model

(d) Gauss PSF Residuals (e) Microlens PSF Residuals

Figure 2.3 (a) A 50 x 50 pixel cutout of an observed H band Xe arc lamp image. (b) A model Xe arc lamp image created using Gaussian PSFs. (c) A model Xe arc lamp image created using Microlens PSFs. (d) The residuals obtained by subtracting the observed lenslet spectrum array from a lenslet spectrum array created by simulating gaussian PSFs. The reduced χ^2 value for the full image (2048 x 2048 pixels; ignoring bad pixels) is given. (e) The same as (d) for the microlens PSFs. Though both the Gaussian and microlens PSFs fit the peak locations, dispersion and spectral rotation well, the microlens method does a much better job of fitting the image background, and the shape of the PSF.

nighttime calibrations. This algorithm executes in seconds, several hundred times faster than the full wavelength calibration algorithm.

2.3 Wavelength Performance

2.3.1 Accuracy of the Wavelength Solution

To achieve the science goals of GPI, we require an uncertainty in the spectral characterization of $< 5\%$ which requires the wavelength solution to be accurate to within 1%. To test the accuracy of the wavelength solution, we created an extracted datacube of a lamp image with 37 spectral channels and compared the theoretical location of the brightest spectral peak to a histogram of peak locations in the reduced cube. An example histogram using an H band Ar wavelength solution to fit a Xe arc lamp is provided in Figure 2.4. The histogram is sharply peaked at 0.0321 detector pixels from the expected location, demonstrating an accuracy in the wavelength solution of 0.032 %. Note that the discrepancy of 0.0321 pixels is the value of pixel-phase error that you would expect from Gaussian fitting (Ingraham et al., 2014a). Table 2.1 provides the accuracy in pixel location and percent (i.e. $\Delta\lambda/\lambda \times 100$) for all bands. In all bands, the peak wavelength was within a tenth of a pixel of the expected location and was accurate to within a tenth of a percent or less, well below the required accuracy.

Table 2.1 Derived accuracy of the wavelength solution using the Ar arc lamp. Column 2 gives the difference in the measured and expected wavelength of the emission lines in detector pixel. Column 3 gives the associated wavelength discrepancy in microns. Column 4 gives the accuracy of the wavelength solution in percentage ($\Delta\lambda/\lambda \times 100$).

Band	Pixel Offset	$\Delta\lambda\,(\mu m)$	$\Delta\lambda/\lambda$ %
Y	0.096	0.0013	0.14
J	0.084	0.00068	0.054
H	0.032	0.00049	0.032
K	0.095	0.0014	0.07

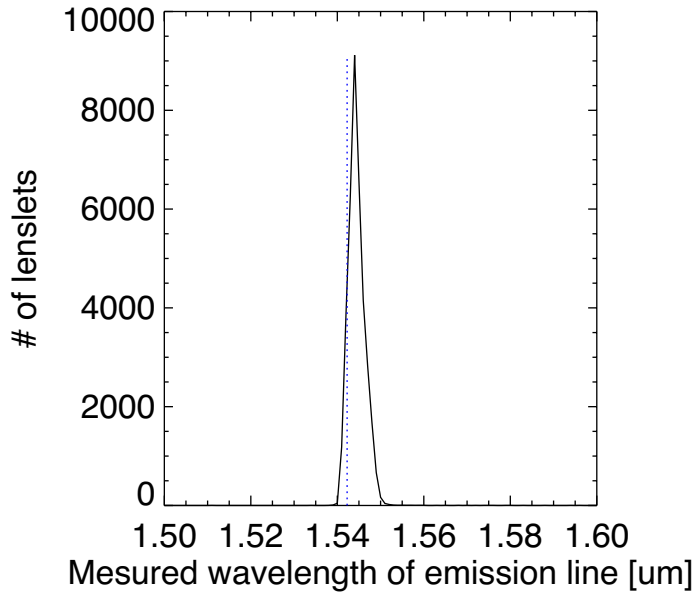

Figure 2.4 Histogram of the measured wavelength in μm of the brightest spectral peak for an H band Xe arc lamp spectral extraction using an Ar wavelength solution, for all the lenslets in the image. The dotted line represents the theoretical location of the peak. The histogram is strongly peaked at a value within 0.032 pixels of the correct wavelength.

2.3.2 Ar vs. Xe Lamps

The accuracy of the wavelength solution is limited by the calibration sources available in GCAL. At the spectral resolution of GPI, neither the Xe nor the Ar lamps provide multiple defined peaks to fit the spectral dispersion in all bands. Figure 2.5 provides a cutout of the detector images for both Xe and Ar arc lamps in all bands. To fit the wavelength solution as described in Eq. (1), a spectrum must have multiple sharp and unblended peaks. Multiple blended peaks at low signal to noise bias the dispersion estimate and consequently, the spectral positions. For all bands but Y, the Xe lamp provided the most accurate solution. However, the Xe lamp in GCAL is ~ 3 times fainter than the Ar lamp, requiring more time spent on overhead calibrations. With the new least squares algorithm, we are able to reproduce the results of the Xe lamp with the brighter Ar lamp by fitting many of the blended lines at once. The GPI pipeline is able to produce wavelength solutions with $< 1\%$ uncertainty for both lamps.

Figure 2.6 examines the disparities in the wavelength solution produced by the Ar and Xe lamps. Wavelength solutions for each band were calculated separately using both the Ar and Xe arc lamps. Histograms of the Xe - Ar values for the x and y positions, dispersions (w) and spectral tilt (θ) are given. The Ar and Xe wavelength solutions agree best in *K2* band with $\sigma < 0.02$, where both arc lamps have only two distinct peaks. The consequences of mixed emission lines is demonstrated well in the J band dispersion histogram in Figure 2.6. J band has only one easily distinguishable

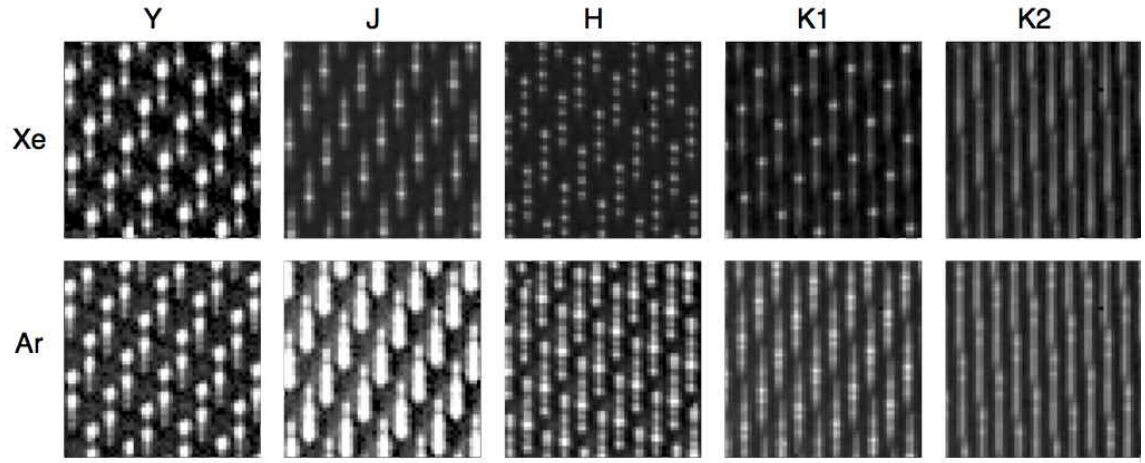

Figure 2.5 Examples of GCAL spectra for Xe and Ar for all GPI filters, for a 50x50 pixel subregion near the center of the detector. These are all shown displayed on a log scale from 0.1 to 50 counts per second per detector pixel. The Ar spectra are consistently brighter than Xe but generally have less well separated emission lines. In the K1 and K2 spectra, the thermal background continuum is visible and at K2 is the dominant source of light. Background exposures must be observed and subtracted prior to generating wavecals for K1 and K2 but are not needed at shorter wavelengths.

line and a faint clump of blended lines in both Xe and Ar. Due to uncertainties in the best fit location of the fainter, blended lines, the dispersion preferred by the Xe lamp wavelength solution is $\sim$ 0.2 nm/pixel greater than the Ar lamp solution, leading to a disagreement in the x_0 and y_0 locations. The x-axes of the histograms exacerbate the disagreements between the Xe and Ar lamps, however, the $\sim$ 0.2 nm/pixel discrepancy in dispersion only contributes to a $\sim$ 1 % uncertainty (average dispersion is $\sim$ 14 nm/pixel).

2.4 Flexure

The wavelength calibration algorithm described above is capable of tracking the motion of the lenslet spectra across the detector plane to an accuracy of 1/10th of a pixel. Therefore, it can be used to trace the flexure of the optics within the IFS causing shifts in the spectral positions with instrument position. These shifts are thought to be caused by motion of one or more of the optics between the lenslet array and the detector. Using the flexure rig at Gemini South Observatory during early commissioning, we examined the magnitude and direction of shifts due to IFS flexure from motions of GPI when the telescope moves in elevation, and from rotations of the Cassegrain Rotator about the telescope optical axis. The observed flexure appears to be a complex function of instrument current elevation, hysteresis from prior elevations, and occasional larger shifts which sometimes but not always correlate with thermal

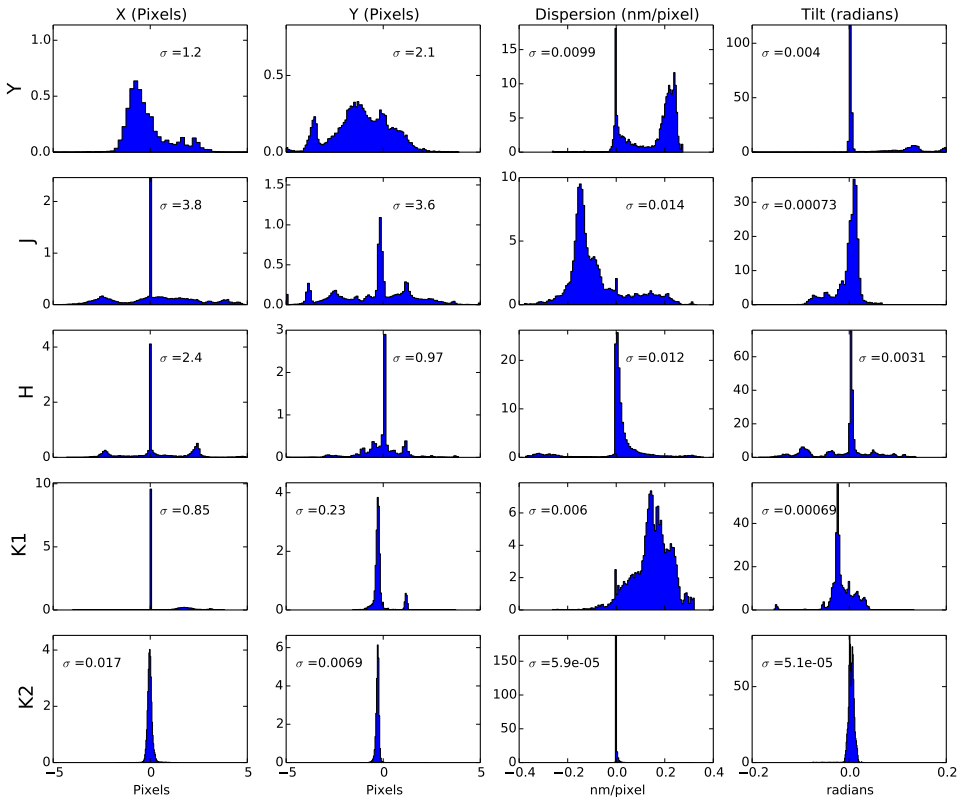

Figure 2.6 Performance of the Ar and Xe lamps. This figure gives histograms of the difference in the x and y positions, dispersions (w) and tilt (θ) values between the Ar and Xe lamps for each band. The bands are listed down the side and the spectral properties are listed across the top. Histograms were calculated using Xe - Ar values. The probability distribution (sum of the bin size times the number of lenslets in that bin) is normalized to one, with 100 bins per histogram. The variance σ is included with each plot. Differences between the Ar and Xe lamp wavelength calibrations are generally small, but there are biases in the solutions in the *Y, J,* and *K1* bands caused by the different sets of emission lines available between the two lamps.

cycling of the IFS. There is a reproducible general trend as a function of elevation but substantial scatter around this due to changing offsets as a function of time. These factors are not yet all fully understood. With changes in elevation from zenith to the horizon, the observed flexure follows an arc showing ∼0.8 pixels of motion along the X-axis and ∼0.4 pixels along the Y-axis. The motion is generally repeatable to within 0.1 pixels. Figure 2.7 shows the change in position on the detector over time due to flexure. The bulk shifts between observing runs are thought to be partially the result of motion about the rotational axis which occurs when other Gemini instruments that require compensation for field rotation are in use. Over the course of an observing run, only the elevation axis is expected to change with elevation of the target. The rotational axis is only affected when other instruments on Gemini South are observing.

The shifts due to flexure are not constant across the field of view of the detector. Figure 2.8 provides a vector plot illustrating the change in position of the lenslets over the detector resulting from a 30 degree change in elevation. The magnitude of the flexure shifts changes by $\sim$ 0.15 pixels across the detector. At most, this will cause flexure variations of $\sim$ 0.08 pixels from the mean shifts in x and y for an image which is below the threshold for uncertainties in the wavelength solution. Thus, deviations in the flexure correction for different regions of the detector are currently being ignored. It is sufficient to use only the mean shifts in the correction. In the future it may be possible to correct for flexure within the spectral extraction process by implementing a least square inversion flux extraction method (e.g. Draper,

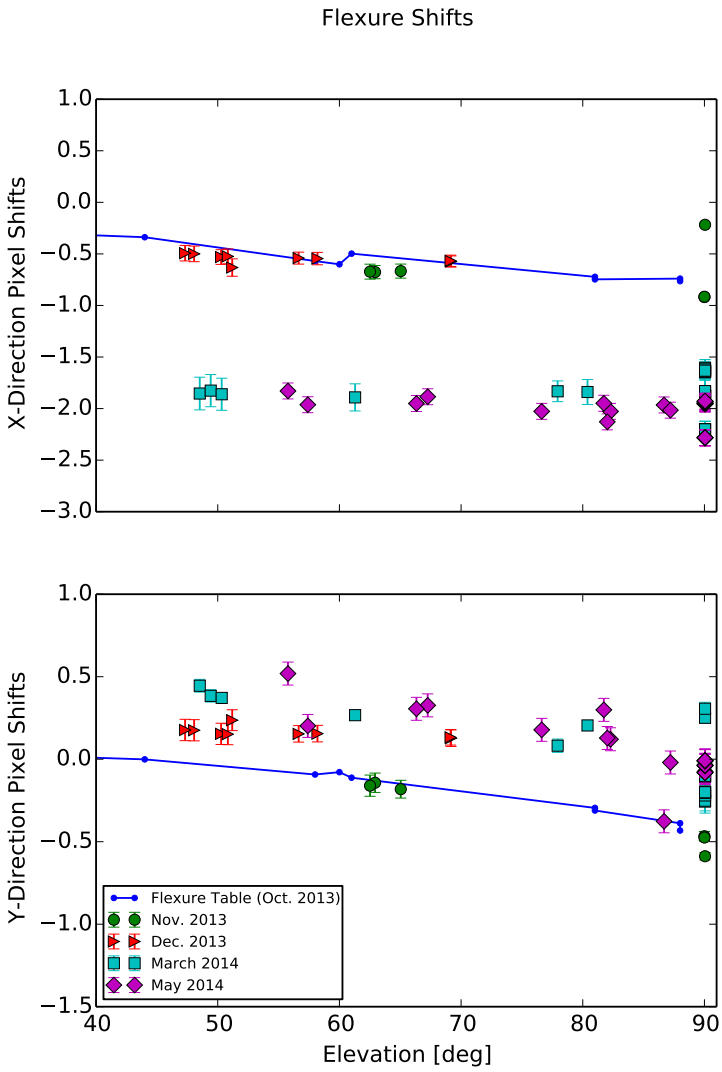

Figure 2.7 Gravitationally induced flexure shifts with varying elevation for the four GPI commissioning runs thus far. Top: x-shifts (roughly perpendicular to dispersion direction) as a function of elevation. Bottom: y-shifts (parallel to dispersion direction) as a function of elevation. The predicted shifts from the Flexure table calibration file constructed from October 2013 data is given by the blue dashed line. Data taken on different dates is color coded and described by the legend. During the course of a single night, the x and y shifts with elevation are repeatable. However, large shifts occur from night to night most likely due to rotation of GPI about it's rotational axis while other Gemini Instruments are in use.

Zachary H. & the GPI Team, 2014; Maire, Jérôme & the GPI Team, 2014).

2.5 Recommended Practices

Deep arc lamp exposures should be taken in all bands at least once an observing semester to calibrate the GPI Integral Field Spectrograph with a spectral accuracy of $< 1\%$. This requires Xe or Ar arc lamp images with SNR $\gg 20$ per pixel in the emission line wings, corresponding to SNR of $\sim$ 50 - 80 at the spectral peaks. In H and both K bands an Ar arc lamp is sufficient and requires less time spent on calibrations. We recommend using the Xe arc lamp for J and Y bands because the Ar lamp does not have sufficient bright and unblended peaks to perform an accurate calibration. To correct the spectral positions for flexure variations with elevation and from night to night, a single one-minute H band Ar arc lamp exposure is recommended contemporary with each science target, at the same elevation.

The GPI Data Reduction Pipeline (See Perrin et al., 2014b) includes modules (termed primitives) to create both the high S/N wavelength calibration files and a fast method for determining offsets from a short arc lamp exposure. The "2D Wavelength Solution" primitive performs the full wavelength solution for all lenslets. Because that this primitive is computationally intensive and takes several hours to run, the "Quick Wavelength Solution" primitive was developed to fit only the positions of a subset of the lenslet spectra over the field of view to calculate an average bulk shift.

For the quick look reductions produced at Gemini, If an arc lamp image in any band is taken directly before a science image, the GPI DRP will automatically run the quick wavelength solution algorithm, determine the positional shifts due to flexure, extrapolate those shifts to the band of the science observations and correct for these shifts when performing the spectral extraction. If an arc lamp image isn't taken prior to a science image, the pipeline will use the most recent arc lamp image for the correction.

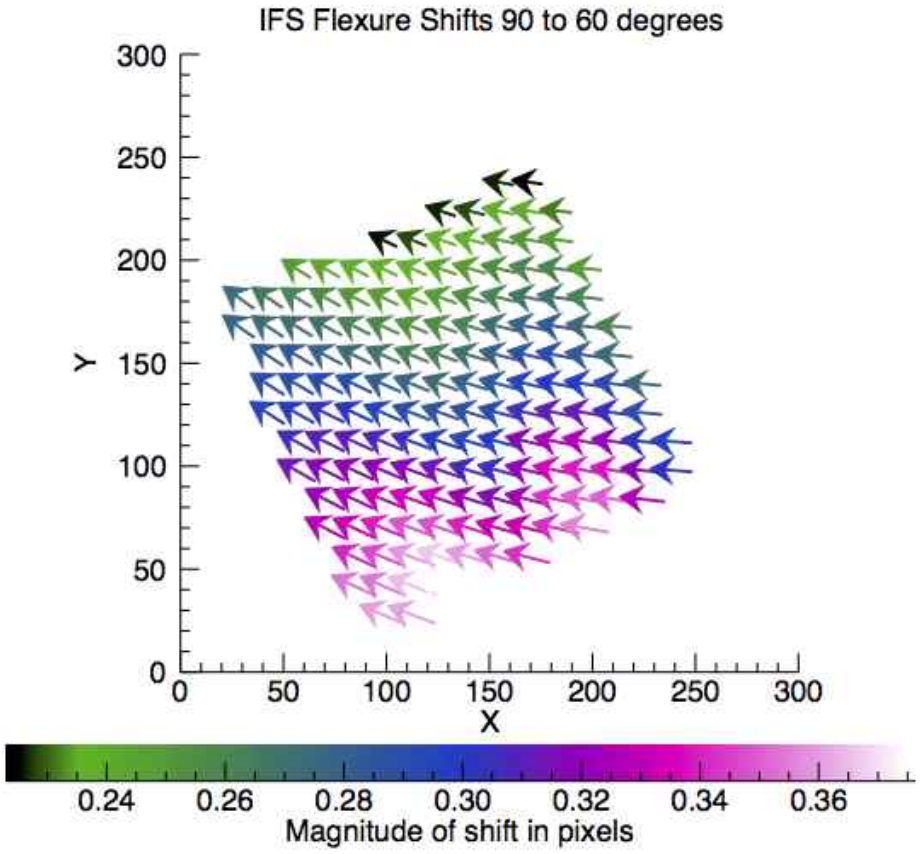

Figure 2.8 Flexure across the field of view. Using arc lamp images taken at zenith (90 degrees) and 30 degrees off of zenith, we track the variation in flexure over the detector area. There is a clear variation from top to bottom of the FOV, but at 30 degrees, the difference is $\pm$ 0.08 pixels.

Chapter 3

Gemini Planet Imager Observational Calibration XIII: Wavelength Calibration Improvements, Stability, and Nonlinearity

Abstract

We present improvements to the wavelength calibration for the lenslet-based Integral Field Spectrograph (IFS), that serves as the science instrument for the Gemini

Planet Imager (GPI). The GPI IFS features a $2.7'' \times 2.7''$ field of view and a 190 x 190 lenslet array (14.1 mas/lenslet) with spectral resolving power ranging from R $\sim$ 35 to 78. A unique wavelength solution is determined for each lenslet characterized by a two-dimensional position, an n-dimensional polynomial describing the spectral dispersion, and the rotation of the spectrum with respect to the detector axis. We investigate the non-linearity of the spectral dispersion across all *Y, J, H,* and K bands through both on-sky arc lamp images and simulated IFS images using a model of the optical path. Additionally, the 10-hole non-redundant masking mode on GPI provides an alternative measure of wavelength dispersion within a datacube by cross-correlating reference PSFs with science images. This approach can be used to confirm deviations from linear dispersion in the reduced datacubes. We find that the inclusion of a quadratic term provides a factor of 10 improvement in wavelength solution accuracy over the linear solution and is necessary to achieve uncertainties of a few hundredths of a pixel in J band to a few thousands of a pixel in the K bands. This corresponds to a wavelength uncertainty of $\sim$ 0.2 nm across all filters.

3.1 Gemini Planet Imager Wavelength Calibration

The Gemini Planet Imager (GPI) is a high contrast instrument located at Gemini South designed to directly detect and characterize exoplanets. The main science

instrument on GPI is an Integral Field Spectrograph (IFS) capable of obtaining low resolution spectroscopy with R $\sim$ 35 - 78 across all the *Y, J, H,* and *K* bands. The GPI IFS uses a lenslet based design to reproduce 190 x 190 microspectra in the narrow 2.7" x 2.7" field of view of the Hawaii 2RG detector (Chilcote et al., 2014). Each bandpass is split into 37 wavelength channels, with *K* band split into two separate bands to limit the overlapping of the microspectra for adjacent lenslets. The field of view and spectral resolution were carefully chosen to produce Nyquist sampling on the detector at the shortest wavelengths, while providing sufficient spectral resolution at the longer wavelengths to resolve important features in planetary atmospheric models (McBride et al., 2011).

A wavelength solution is determined for each lenslet individually, and is characterized by a 2D position, the dispersion, and the tilt (angle from vertical in radians) of the spectrum. Each set of parameters is different for the $\sim$ 36000 lenslets and vary widely across the field of view. A cutout of a single lenslet is modeled by placing 2D Gaussian PSFs at the predicted spectral peak locations for the GCAL (Gemini's calibration lamp unit; Ramsay Howat et al., 1997) Xe or Ar arc lamp sampled at the resolution of GPI. The data and model spectra are compared using the constrained Levenberg-Marquardt least-squares minimization algorithm to minimize the error weighted squared residuals of the two images over the free parameters above (Levenberg, 1963; Marquardt, 1944). This allows measurement of spectral positions to better than 1/10th of a pixel. For a full description of this algorithm, (see Wolff

et al., 2014).

In this paper, we present work completed on the wavelength calibration of the Gemini Planet Imager since 2014, and includes many lessons learned from $\sim$ 2 years on sky at Gemini South. In Section 1.1, we describe the recommended practices for the wavelength calibration of any spectral mode GPI science data for the general GPI user. In Section 1.2, we provide techniques for checking the quality of your data and troubleshooting any data quality issues. In Section 2, we discuss the stability of the wavelength calibration over time. In Section 3, we examine the non-linearity of the wavelength solution. Finally, we discuss ongoing work on the simultaneous wavelength solution across all filters.

3.1.1 Recommended Practices

For the ease of use of the general observer, the GPI team has provided a publically available Data Reduction Pipeline (DRP) for the calibration and analysis of both spectral and polarimetry modes of GPI (Perrin et al., 2014a,b). 'Recipes' are furnished for different types of data and are made up of 'Primitives' which handle the individual tasks (Ex. dark subtraction, bad pixel correction, wavelength calibration, generating the spectral datacubes, PCA post processing techniques etc.). There are several recipes devoted to wavelength calibration. These are dicussed in detail below. See Perrin et al. (these proceedings) for a full description of the data infrastructure developed for the GPI Exoplanet Survey Campaign, including the GPI DRP. Below

we discuss the steps for properly calibrating the spectra of a science target; both the data to be obtained, and the data reduction processes using the GPI DRP.

- As part of Gemini South's regular calibration program, a set of high signal-to-noise arc lamp images are obtained each time GPI is remounted on the bottom port of the Gemini South telescope using the Gemini Facility Calibration Unit (GCAL). The Argon arc lamp is used as it requires a shorter exposure time than the Xenon lamp to acheive the same SNR.

- The user should reduce these data using the **Wavelength Solution 2D** Recipe in the GPI DRP. With the new release of the GPI DRP in July 2016, the user now has the option to choose between a Gaussian PSF and a Microlens PSF (Ingraham et al., 2014a) to simulate the arc lamp spectra. The Microlens PSF generally does a better job in fitting the wings of the PSF and produces a better wavelength solution overall. Note that a full wavelength calibration is computationally intensive. We recommend using the parallelization option for faster computing time (Ex. $\sim$ 10 min. using 4 cores).

- At the beginning of each science sequence, a short 30 second H band Argon Arc lamp exposure should be taken at the elevation of your target. This will be later used to correct for any shifts of the lenslets on the detector due to internal flexure of the IFS. H band data are used to limit exposure time, and can also be used to provide an offset to other bands.

- These short arc lamp images should be reduced using the **Quick Wavelength Solution** Recipe in the GPI DRP. Instead of computing a solution for each lenslet individually, this recipe computes the locations of every 20th lenslet (by default) and computes the average shift across the entire field of view.

- When reducing a science sequence, the wavelength calibration is added in the *Load Wavelength Calibration* primitive. The files generated in the steps above should be selected automatically, but the user can manually input a file as well. To correct for the internal flexure of the IFS, we recommend using the 'BandShift' mode in the *Update Spot Shifts for Flexure* primitive. This primitive will use the short arc lamp image to correct for any shift in the lenslet spectra that occurred between the high SNR wavelength calibration images and the science data.

A description of each the steps above is available in the GPI pipeline documentation (`http://docs.planetimager.org/pipeline/`). In the next section, we discuss how to check the quality of a wavelength calibration file, and several suggestions for troubleshooting.

3.1.2 Quality Checks and Troubleshooting

For the general GPI user, we have included several tools to inspect the quality of the wavelength calibration in the GPI DRP. Before beginning to reduce any arc

lamp image files, we recommend inspecting them by hand. There is an issue in the communication software between the GCAL unit and GPI that occasionally causes a shutter to remain closed, allowing no photons to reach the instrument during an arc lamp exposure. Once you have confirmed that the raw files have counts, generate a wavelength calibration file using the steps outlined above. To check if the produced wavelength calibration file (extension 'wavecal') is a good fit to your science data, display both images using GPItv (display module used in the GPI DRP). First, open your science image in GPItv, and overplot the wavelength calibration file first by selecting it and then by using the 'Plot Wavecal/Polcal Grid' in the Labels menu of GPItv. This will draw a grid of lenslet spectra over-top of the observed spectra. A window allows the user to manually adjust the x and y positions of the lenslet spectra before drawing. Alternatively, the 'Move Wavecal Grid' Mouse Mode will allow the user to click and drag in the GPItv window to move the grid of lenslet spectra.

The *Quality Check Wavelength Calibration* Primitive is included in all Wavelength calibration recipes. It performs several checks that are often performed by eye in GPItv. First, the size of the wavelength calibration file is checked for the correct dimensions, and the primitive confirms that all of the lenslet positions are not the same. Histograms are generated for the x and y positions, dispersion (μm/pixel), and the tilt (orientation of the spectra on the detector in radians) of the lenslet spectra. If any two neighboring lenslets have values that are some threshold above the mean difference, the wavelength calibration file will fail the basic quality check. By default,

this occurs if the x or y positions vary by more than 2 pixels, the dispersion varies by more than 0.002 μm/pixel, or the spectral tilt varies by more than 0.1 radians ($\sim 5^{\circ}$). As the name implies, this is only a basic quality check. It is still recommended that the users display the wavelength calibration file overplotted with their science data in GPItv.

3.2 Stability of the Wavelength Calibration

After more than two years of on-sky science operations, we have a better understanding of how the stability of the wavelength calibration for the IFS changes with environment and time. Including both long exposure arc lamp images taken once per GPI run and short arc lamp images taken with each science sequence, we have generated over 1000 wavelength calibration files across all bands ($\sim$ 800 in H-band and 50 - 100 in each of the other filters), with data obtained as early as November 2013.

We examined the behavior of the lenslet positions, spectral dispersion, and tilt with several header keywords relating to the environment on Gemini South including the temperature in the IFS and the detector temperature, the telescope elevation, and the date of the observation. We found no correlation with temperature inside or outside of the instrument. While the tilt of the lenslet spectra varies across the field

of view, for a given lenslet the tilt is very stable with variations $< 10^{-3}$ radians in the entire sample.

The spectral dispersion was observed to change with time gradually by $\sim 4-5$ % in 1.5 years, with an apparent turning point at the beginning of 2015, and potentially another change at the beginning of 2016 (Figure 3.1). The direction and magnitude of the change varies with band, and the reason for this evolution remains unknown. It is unclear whether this is a gradual or discontinuous change. Some number of jumps with superimposed noise could mimic a gradual change in the data, and may be easier to explain with a mechanical change in the IFS. It is possible that a mechanical change in the prism could cause some angle to drift over time, but we have not identified an optic in the IFS that could reproduce this change in dispersion while conserving the tilt of the lenslet spectra.

Alternatively, the dispersion change could be an artifact of the aging of the GCAL arc lamps. Any changes in excitation associated with aging cathodes, gas contamination or leaks etc. could effect our ability to distinguish between the blended lines that make up the low resolution GPI spectra. This could explain why the effect is largest in J and H bands which have the fewest distinct spectral lines. We see no change in the trend between Xe and Ar lamp data, though we only have Xe arc lamp data in H-band. This could also be a data processing effect. We have not reduced all of the wavelength calibration files with the same version of the Data Reduction Pipeline. However, when re-processing a subset of older calibration files, we found no

change in the dispersion.

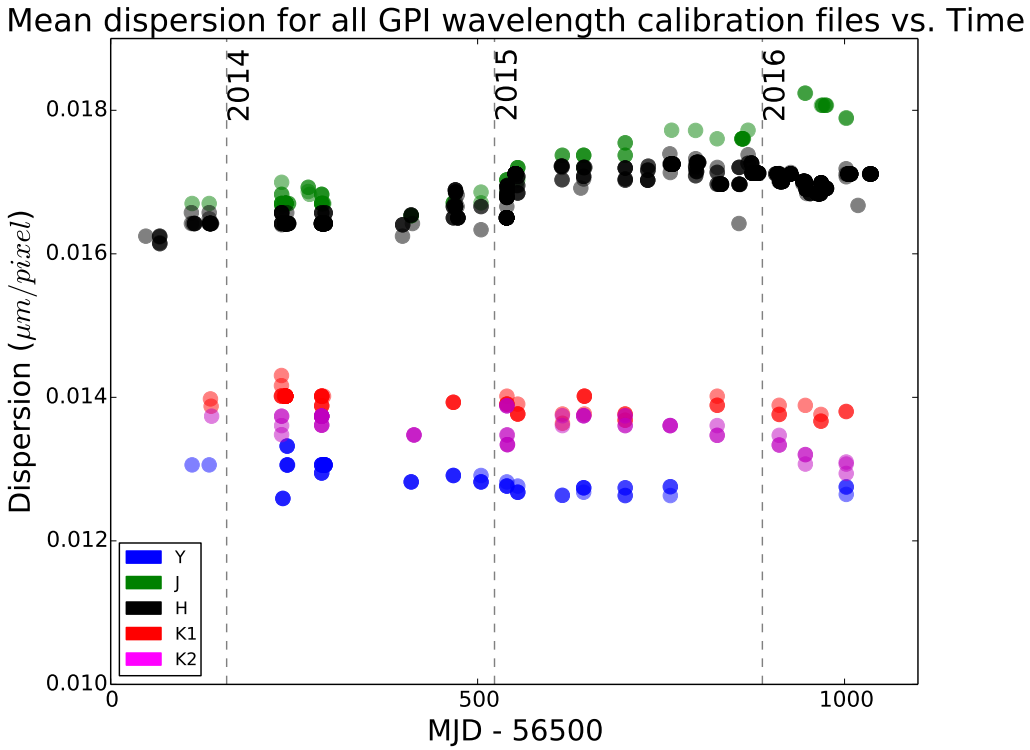

Figure 3.1 Mean spectral dispersion for all GPI wavelength calibration files as a function of time; colorcoded by filter. Beginning in 2015, there is a change in the spectral dispersion with time by $\sim 4-5$ % over 1.5 years.

As mentioned previously, the x and y positions of the lenslets vary with flexure. The internal flexure of the IFS has two components: (1) Repeatable sub-pixel shifts vary with the elevation of the telescope as the gravity vector on the IFS changes. This behavior is well defined by a hysteresis curve and can be easily corrected. (2) Occasionally, a large shift of $\leq \pm 3$ pixels in either x or y will result from the shifting of an unidentified optic within the IFS by a few millimeters. This is unpredictable and must be corrected using 30 second arc lamp images taken before each science

sequence.

Both behaviors are demonstrated in Figure 3.2, which gives the change in the x and y pixel locations for the central lenslet between the short arc lamp image (quick), and the long exposure arc lamp image (master) taken at the beginning of the run in the same bandpass, color coded with elevation. While there is some scatter, most points in the sample fall into three distinct regions. This is likely a result of the loose optic oscillating between two states, i.e. state (a) and state (b). For the largest population, both the master and quick wavelength calibration files were taken with the optic in the same state. The two other groups correspond to occasions when the master files were taken with the optic in state (a) and the quick files were taken with the optic in state (b) and vice versa. Within each of the three populations, there is a clear trend in elevation. Larger shifts occur as the telescope is moved away from zenith (90 °).

3.3 Nonlinearity of the Wavelength Solution

In this section, we investigate any departures from linearity of the wavelength solution. We examine any uncertainties in the spectral positions that could result from the assumption of a linear dispersion solution, and look for alternate expressions for the wavelength as a function of position on the detector. We first use simulations

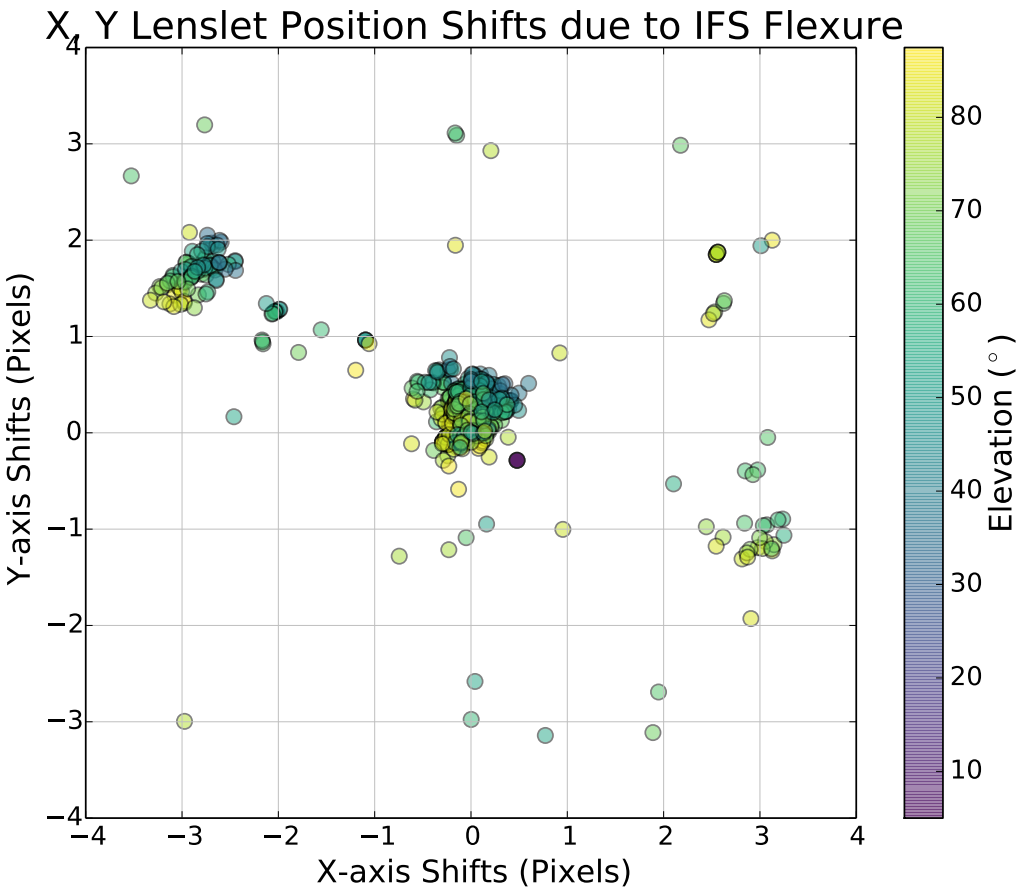

Figure 3.2 The change in the x and y pixel locations for the central lenslet between the quick arc lamp image, and the long exposure arc lamp image taken at the beginning of the run in the same bandpass. Color coded with elevation. Zenith is at 90°.

of the IFS output on the detector, and compare this to GCAL arc lamp observations. We also use GPI's Non-Redundant Mask mode for an independent measurement of the wavelength scaling.

3.3.1 Modeled Performance

Using the geometry of the optical path within the GPI IFS, we are able to examine the theoretical spectrum of each lenslet produced by the dispersing prism. We derived the theoretical pixel position as a function of wavelength, λ, by combining the optical path of the GPI IFS using Zeemax files with the Sellmeier approximations for the indices of refraction of both glass components of the dispersing prism. This was then propagated into pixel values using an estimate for the effective camera focal length of 232 mm and the pixel size of 18 μm.

We fit the resulting dispersion by several n-dimensional polynomials in λ with n = 1 - 4 for each band individually. In the case of a 4th degree polynomial, the residuals no longer show any obvious structure. However, given our ability to resolve spectral features on the detector plane, it is unlikely that we will be able to detect pixel positons below the 1/100th of a pixel level. A quadratic solution for position as a function of λ is required for uncertainties < 0.01 pixels. This gives an order of magnitude improvement in pixel uncertainties from a linear fit to the dispersion. An example for H-band is given in Figure 3.3, and this behavior is demonstrated in all filters.

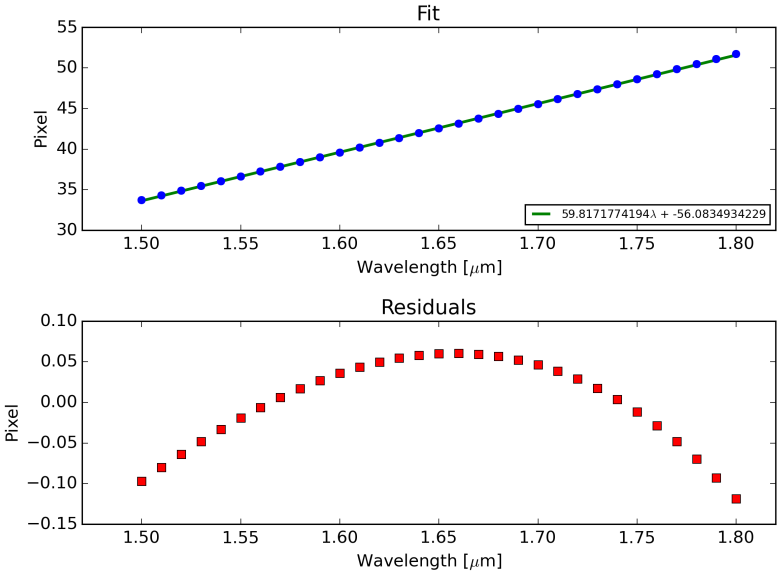

(a) Linear Dispersion

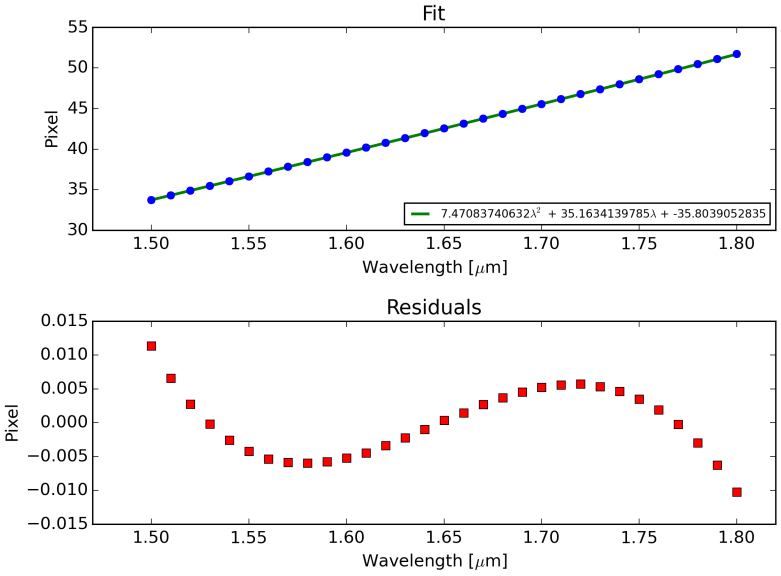

(b) Quadratic Dispersion

Figure 3.3 Theoretical fits to the dispersion of the GPI IFS using (a) a linear model for the position as a function of wavelength, and (b) a quadratic model. The quadratic solution results in errors that are an order of magnitude less than the linear case with uncertainties in the pixel position of < 0.01 pixels.

3.3.2 Non-Redundant Masking as an Independent Wavelength Check

GPI is equipped with a Non-Redundant Mask (NRM); an interferometric mask containing 10 holes separated by non-redundant baselines (Greenbaum et al., 2014). GPI's NRM mode complements GPI's coronagraph by accessing a smaller Inner Working Angle (R $\sim \lambda/2D$ where D is the longest baseline) at moderate contrast. The size of the NRM PSF directly depends on the wavelength and is a sensitive probe of changes to pixel sampling with changing wavelength. Consequently, the GPI NRM allows for wavelength calibration of the GPI IFS without requiring an external calibration source.

An independent measure of the wavelength (assuming a pixel scale) can be accomplished by cross-correlating NRM exposures with simulated PSFs at varying pixel scales. Reference PSFs can be generated numerically knowing the pupil geometry and varying the wavelength scaling around an expected value for the data. While the absolute wavelength calibration depends also on the pixel scale, the NRM can measure deviations from a linear wavelength function across a given filter. For each spectral channel, the NRM PSF is cross-correlated with each of the reference PSFs, and the data are fit to a parabola to determine peak correlation. The location of the peak corresponds to the best fit magnification for that spectral channel. Figure 4 shows the accumulation of several NRM datasets in various bands, comparing the measured

wavelength compared with the wavelength reported by the GPI pipeline solution. The residuals are generally 0.05 ?m which agrees well with what is predicted from the modeled performance and these errors could likely be reduced by an order of magnitude. Re-reducing the NRM images with updated non-linear corrections could help verify that a new solution is accurately representing the true dispersion.

3.3.3 Quadratic Wavelength Solution

With the 2D wavelength calibration algorithm, we provide a wavelength solution accurate to 1/10th of a pixel. This sensitivity allowed us to examine the departure of the IFS prism dispersion from linearity. The x and y pixel position for each lenslet is defined by a unique x_0 and y_0 position for a reference wavelength λ_0 (which varies with filter), the tilt (θ, angular orientation of the lenslet in radians from vertical), and a dispersion. In the linear case, the dispersion is assumed to be linear (with coefficient w), and the positions are defined by: $x = x_o + \sin\theta\frac{\lambda-\lambda_o}{w}$ and $y = y_o - \cos\theta\frac{\lambda-\lambda_o}{w}$ where the wavelength, λ, for a given pixel is given by $\lambda = w\sqrt{(x-x_0)^2 + (y-y_0)^2} + \lambda_0$. For the quadratic formalism of dispersion, we expand these equations in $(\lambda - \lambda_o)$ as shown in the Equations below.

$$x = x_o + \sin\theta\left[(\lambda-\lambda_0)/w + \boldsymbol{q(\lambda-\lambda_0)^2}\right]$$

$$y = y_o - \cos\theta\left[(\lambda-\lambda_0)/w + \boldsymbol{q(\lambda-\lambda_0)^2}\right]$$

NRM-Derived Wavelengths (Alex)

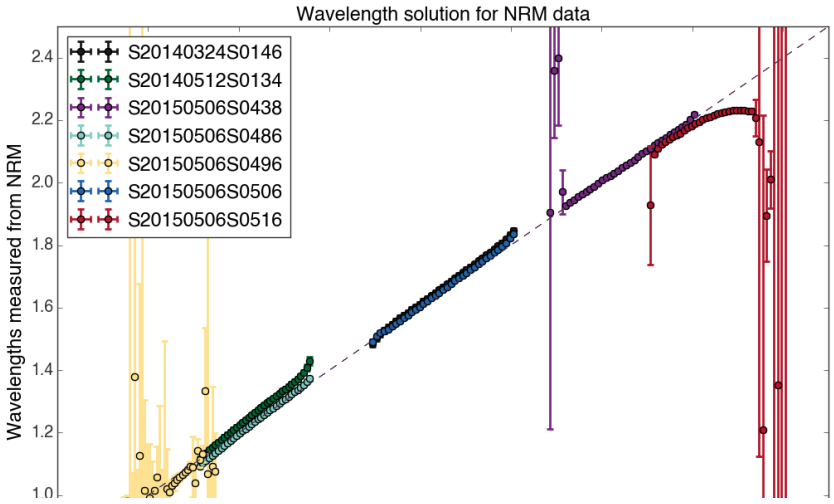

NRM-Derived Wavelengths (Alex)

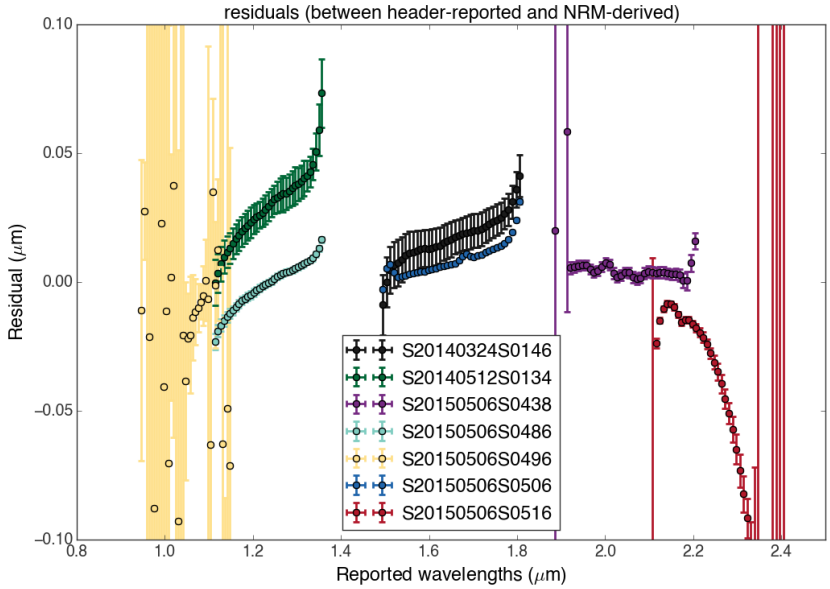

(b) NRM Residuals

Figure 3.4 (a) Wavelength solution derived using the NRM pupil for several datasets. (b) Residuals from a linear fit to the wavelengths derived from the arc lamp wavelength calibration to the wavelengths found in the fit the NRM PSF. All plotted datasets were taken before cryocooler upgrades and suffer vibrations, which blur out fringes. This is especially degrading for Y band data. Lower throughput in K2 could have contributed to the large error-bars measured.

The quadratic term is shown in bold. After some experimentation, the coefficient, q, was found to be well fit by a value of $w/10$. To limit computation time, we fix this value when determining the wavelength solution for each lenslet. The magnitude of the quadratic component varies with filter, but is generally less than 0.003 % of the linear term (ie. $\frac{q}{1/w} < 3 \times 10^{-5}$), and this serves as a small perturbation to the linear case.

The largest improvement was seen in the reduction of the H-band. A comparison between the linear and quadratic fits for a single lenslet in a Xe arc lamp dataset is given in Figure 3.5. The quadratic solution improved the reduced χ^2 by a factor of $\sim$ 2 above the linear case (both using the microlens PSF), and gives an position accuracy of 0.012 pixels, which is approaching the theoretical limit of 0.01 pixels (Figure 3.6). In other bands, the improvement is less pronounced. In *K1* band for example, the quadratic solution only provided a factor of 1.05 improvement over the linear case. This is likely a consequence of our inability to resolve spectral lines in the Argon arc lamp data, rather than a failure of the quadratic dispersion solution to accurately define the data. While the Argon arc lamp available at Gemini South provides the best SNR with the shortest exposure times, the spectral lines in all filters are blended and difficult to distinguish at the resolution of GPI. The Xenon lamp provides better distinction between spectral lines in some filters, but the count rate of the lamp is prohibitively low (Ex. Ar exposure for K2 bands takes $\sim$ 2 hours, and Xe would require at least twice the exposure time to achieve the same SNR).

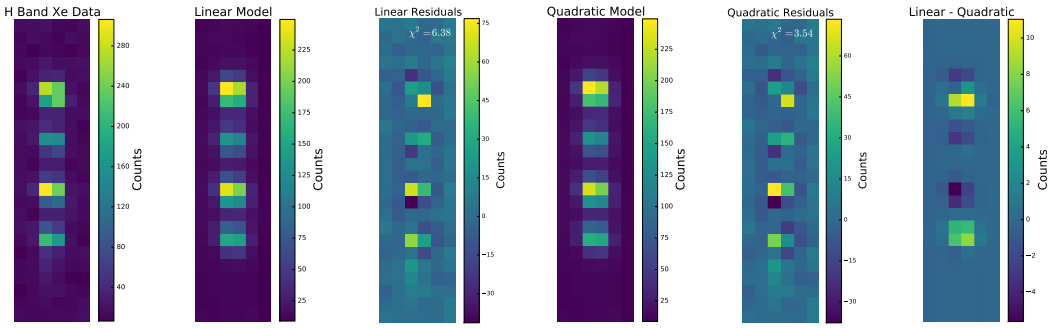

Figure 3.5 (a) A single lenslet cutout of an observed H band Xe arc lamp image. (b) A model Xe arc lamp image created using a linear dispersion model. (c) The residuals obtained by subtracting the observed lenslet spectrum array from the linear dispersion modeled lenslet array. (d) A model Xe arc lamp image created using a quadratic dispersion model. (e) The same as (c) for the quadratic dispersion model, and (f) shows the linear model subtracted by the quadratic model. Note the scale of the residuals. These are largely a consequence of the microlens PSFs being too narrow in the peak than the actual instrumental PSF, and less a result of our uncertainty in the locations of the spectral peaks.

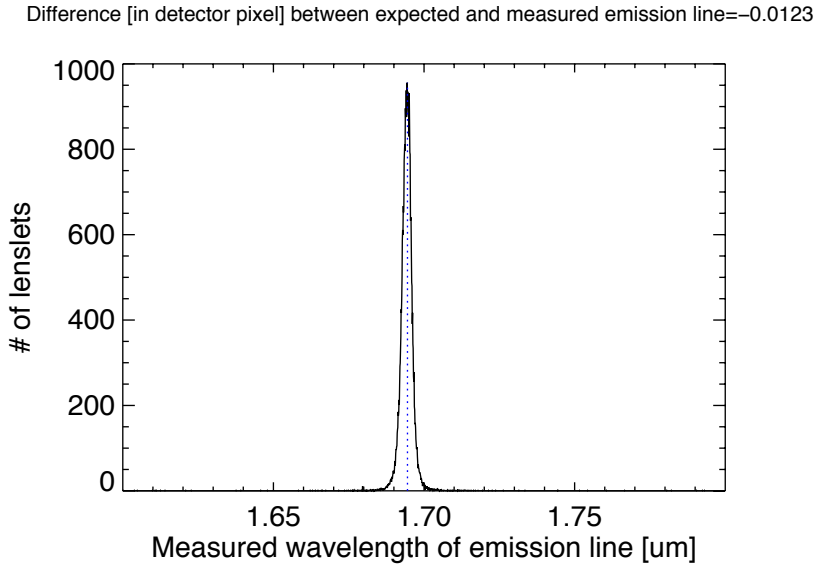

Figure 3.6 Histograms of the measured wavelength in μm of the spectral peak for an H band Ar image for all the lenslets in the image for a quadratic dispersion solution. The dotted line represents the theoretical location of the peak. The quadratic solution peaks at a value within 0.012 pixels of the correct wavelength.

3.3.4 Simultaneous Wavelength Calibration of all Bands

We have shown the improvement afforded by including a quadratic term to the wavelength solution for a single GPI filter, particularly in H-band. Furthermore, it should also be possible to fit the wavelength solutions over the full GPI bandpass simultaneously ($Y-K2$, corresponding to 0.9–2.4μm), assuming separate linear and/or higher-order fits to each of the individual bands. By defining wavelength vs. position across the full bandpass, this would provide small, yet non-negligible improvements to datacube extraction at different wavelengths. As described previously, quick H-band Argon arcs are taken as part of standard GPI observing sequences to calibrate observations at other bands, given the expediency of H-band arcs as opposed to the longer integrations required for arcs at different wavelengths, in particular $K1$ and $K2$. This bootstrapping process, with either a look-up table of flexure shifts, or in 'BandShift' mode, involves extrapolating the shifts due to flexure from the H-band arcs to the band of the science observations, using the x- and y-positions from the most recent wavelength calibration. For this procedure, a higher fidelity spectral extraction may be possible if the extrapolation also incorporates a functional relationship between the wavelength solutions at different bands.

In an initial attempt to fit the full bandpass simultaneously, independent linear solutions for each of the five filters were stitched together and fit with a single poly-

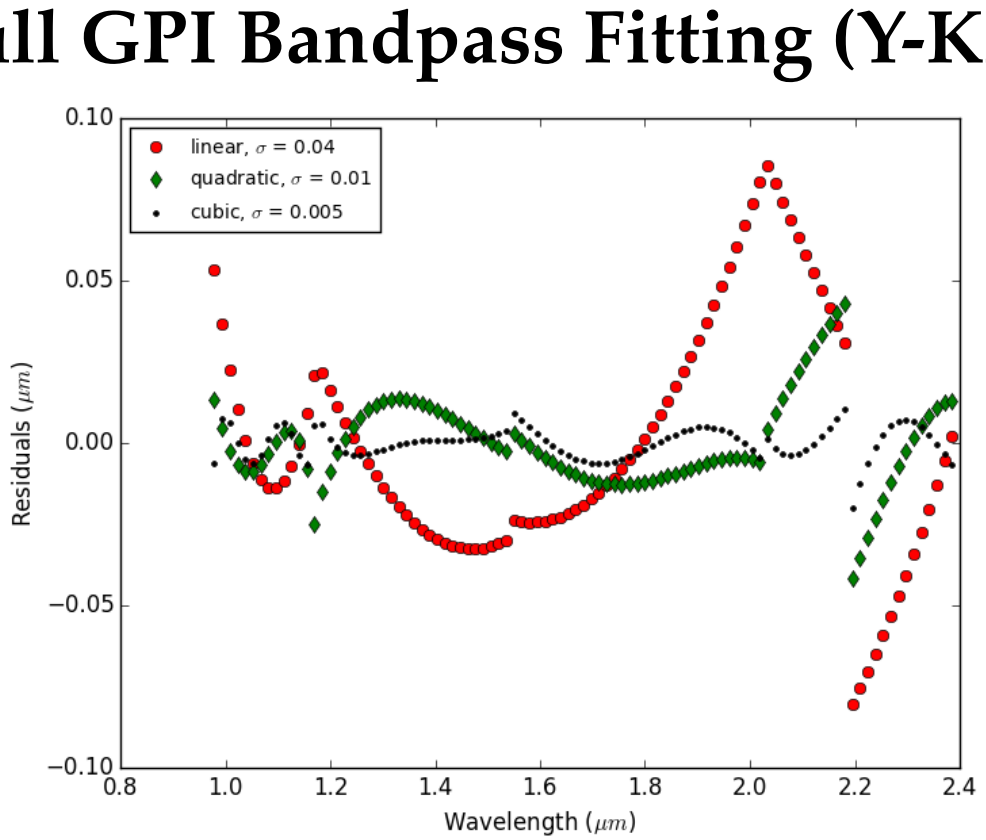

Figure 3.7 Residuals in μm from an overall polynomial fit to each of the independent linear solutions for the five GPI bands ($Y-K2$). The cubic polynomial fit over the full bandpass, shown with black circles, provides the minimal residuals to the wavelength solution in two dimensions, and will be implemented in efforts to improve the fidelity of using quick H-band arcs to calibrate data taken in other bands.

nomial, with results from using polynomials of different orders shown in Figure 3.7. The residuals in μm from the different polynomial fits show that a higher-order polynomial, at least a cubic fit, is required to describe the full bandpass simultaneously in a self-consistent manner. Implementation of a multi-filter and full bandpass wavelength solution option into the existing GPI DRP wavecal primitives is ongoing, with future work involving comparison of the extracted datacube quality with science observations at different wavelengths.

Chapter 4

The PDS 66 Circumstellar Disk as seen in Polarized Light with the Gemini Planet Imager

Abstract

We present H and K band imaging polarimetry for the PDS 66 circumstellar disk obtained during the commissioning of the Gemini Planet Imager (GPI). Polarization images reveal a clear detection of the disk in to the $0.12''$ inner working angle (IWA) in H band, almost 3 times as close to the star as the previous *HST* observations with NICMOS and STIS ($0.35''$ effective IWA). The centro-symmetric polarization vectors confirm that the bright inner disk detection is due to circumstellar scattered light.

A more diffuse disk extends to a bright outer ring centered at 80 AU. We discuss several physical mechanisms capable of producing the observed ring + gap structure. GPI data confirm enhanced scattering on the East side of the disk which is inferred to be nearer to us. We also detect a lateral asymmetry in the South possibly due to shadowing from material within the inner working angle. This likely corresponds to a temporally variable azimuthal asymmetry observed in *HST*/STIS coronagraphic imaging.

4.1 Introduction

Classical T Tauri stars (cTTS) with optically-thick, gas-rich protoplanetary disks provide valuable knowledge of the precedent conditions for planet formation. By comparing the observed intensity in scattered light to radiative transfer models, we can infer the grain properties (size, density, composition) and the geometry at the surface of the disk (e.g. Graham et al., 2007; Murakawa, 2010).

The Gemini Planet Imager (GPI) was designed to overcome the contrast problem inherent in the detection of circumstellar material within $\sim 1.5''$ from their host stars. GPI combines an advanced adaptive optics (AO) system, an apodized coronagraph, and an IR integral field spectrograph with both spectral and polarimetric modes (Macintosh et al., 2014c; Larkin et al., 2014; Perrin et al., 2015).

PDS 66 (MP Muscae) is one of the closest T Tauri stars. It was identified as part

Table 4.1. Gemini Planet Imager observations of PDS 66

Date	Mode	Band	Exp. Time (s)	# of Exposures	Coronagraph Spot Size (")	Field Rotation (°)	Notes
2014 May 14	Spectral	H	59.6	10	0.246	3.5	0.5 – 0.8″ seeing, high winds
2014 May 15	Polarization	H	59.6	32	0.246	13.3	0.7 – 1.0″ seeing
2014 May 15	Polarization	$K1$	59.6	16	0.306	11.4	0.7 – 1.0″ seeing

of the Pico Dos Dias Survey (Gregorio-Hetem et al., 1992). Mamajek et al. (2002) classified PDS 66 as a member of the Lower Centaurus Crux (LCC) subgroup with a mean age of 17 ± 1 Myrs. Mamajek et al. (2002) list PDS 66 as a K1 spectral type star with a kinematic parallax distance of 86^{+8}_{-7} pc and age estimates ranging from 7 – 17 Myrs. PDS 66 was the *only* cTTS found in their sample of over 100 pre-main-sequence stars. Torres et al. (2008) first suggested that PDS 66 is more likely a member of the ϵ Cha Association. Murphy et al. (2013) reinvestigated the membership of PDS 66 and found that the proper motion is more consistent with ϵ Cha (age: 5 – 7 Myrs, kinematic distance: 101 ± 5 pc). The membership of PDS 66 remains somewhat uncertain between LCC and ϵ Cha. Given that the disk properties of PDS 66 appear to be inconsistent with the LCC, and the younger age of ϵ Cha is below the typical disk dissipation timescale of 10 Myr (Haisch et al., 2001), in this paper, we adopt the age and distance appropriate for eps Cha.

The PDS 66 disk is in an interesting evolutionary stage. The spectral energy distribution (SED) lacks signs of large-scale evolution or an inner clearing. Based on the 1.2 mm continuum flux Carpenter et al. (2005) estimated a total dust mass of $5.0 \times 10^{-5} M_{\odot}$. Schütz et al. (2005) modeled the PDS 66 mid-infrared spectra and SED and infer an inner disk radius consistent with the dust sublimation radius of 0.1 AU. However, Cortes et al. (2009) compare the PDS 66 SED to the median Taurus SED and find a flux decrement between 4-20 microns, indicating a partial clearing of material in the disk. CO measurements by Kastner et al. (2010) show

a molecular gas disk extending out to 120 AU with a lower limit for the gas mass of $9.0 \times 10^{-6}\,M_{\odot}$. Although uncertain, this suggests a lower gas-to-dust ratio limit of ≥ 0.2. Even though the accretion rate inferred for PDS 66 is small for a cTTS (estimates range from 5×10^{-9} to $1.3 \times 10^{-10}\,M_{\odot}/yr$ Pascucci et al., 2007; Ingleby et al., 2013), the implied accretion timescale is short, $< 10^5$ yrs. (based on the disk mass inferred from CO).

The PDS 66 circumstellar disk was first resolved in *HST*/NICMOS imaging by Cortes et al. (2009). They detected a disk with an outer radius of 170 AU, and an inclination of $32^{\circ} \pm 5^{\circ}$. The authors also provide evidence for grain growth through an analysis of the spectral energy distribution. Likewise, Bouwman et al. (2008) obtained Spitzer spectroscopy ($8 - 13\,\mu m$) and found that the dust grain properties are well fit by a model consisting of amorphous olivine and pyroxene with average particle sizes of a few microns. Schneider et al. (2014) obtained deep *HST*/STIS coronagraphy showing consistent geometry, albeit with detection of faint halo extending out to beyond 520 AU.

PDS 66 was observed during the commissioning of GPI to test instrument performance on a typical bright, nearby disk. Our GPI observations are described in Section 2. The morphology of the PDS 66 disk as seen in polarized light with GPI is discussed in Section 3. We place limits on our sensitivity to planetary companions in Section 4. Section 5 discusses the results.

4.2 Observations

Coronagraphic imaging polarimetry and spectroscopy of PDS 66 were obtained in 2014 May (Table 1). The GPI Integral Field Spectograph (IFS) has a plate scale of 0.014 arcseconds/pixel, a FOV of 2.8 X 2.8 arcsec^2, and an angular resolution of $\sim 0.05''$ in H band (Macintosh et al., 2014c; Larkin et al., 2014). Data were reduced using the GPI Data Reduction Pipeline; see Perrin et al. (2014c) and references therein. Data were obtained in high wind conditions with the AO system operating at 500Hz. For the spectral mode data, the raw frames were dark subtracted, corrected for bad pixels, destriped to correct for variations across read-out channels, and Fourier filtered to remove microphonics noise. A wavelength calibration using arc lamp data taken before the sequence is used to convert the raw images to 3D spectral datacubes (Wolff et al., 2014). The location of the star behind the coronagraphic mask was measured from the satellite spots (Sivaramakrishnan & Oppenheimer, 2006; Wang et al., 2014) and the data were corrected for spatial distortion.

In polarimetry mode, frames are taken in sets of four different half-wave plate rotations and combined to form Stokes cubes with slices *I, Q, U,* and *V*. Data are dark subtracted, destriped, and a thermal sky background is subtracted (in *K1* band only). The individual frames are converted into two orthogonal polarization states using a spot location calibration file that has been corrected for elevation-induced flexure. Each cube is divided by a low pass filtered flat field to correct for low frequency variations (Millar-Blanchaer et al., 2015). The mean stellar polarization

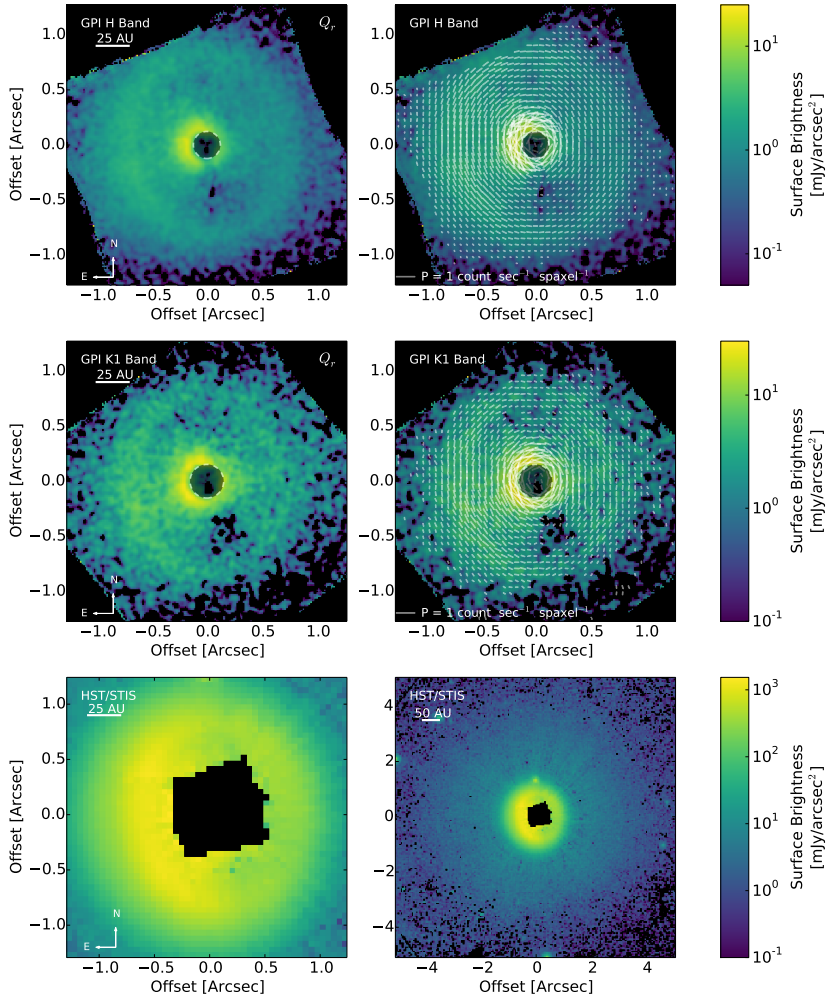

Figure 4.1 Polarimetry data for PDS 66 in *H* band (top) and *K1* band (middle), and white light optical STIS data at two spatial scales for comparison (bottom; data from Schneider et al. 2014). Polarized intensity is shown on the left for the GPI data, while the right panels show the same polarized intensity over-plotted with polarization vectors. The vector orientation gives the position angle for the polarized electric field. Grey inner regions represent the coronagraphic spot size.

and instrumental polarization are subtracted and the polarization pairs are cleaned via a double difference algorithm (Perrin et al., 2015). The satellite spots are again used to determine the location of the occulted star and to calibrate the flux of the disk using a conversion factor of 1 ADU coadd^{-1} s^{-1} = 7.4 ± 2.6 mJy arcsec^{-2} in *H* band and 31 ± 10 mJy arcsec^{-2} in *K1* band (Hung et al., 2015).

Figure 1 shows the *H* and *K1* band polarimetry for PDS 66 with the Stokes vectors giving the orientation. Here the Stokes parameters have been transformed to radial Stokes parameters (Schmid et al., 2006). The $+Q_r$ image contains the polarization oriented in the tangential direction in the disk, $-Q_r$ contains the radial polarization and U_r contains the polarization oriented ±45° from Q_r. For an optically thin disk, the U_r image should contain no polarized flux from the disk and can be treated as a noise map. For an optically thick disk like PDS 66, multiple scattering events can result in non-negligible brightness, at a few % of the Q_r signal for low-inclination disks (Canovas et al., 2015). Given this small amplitude, we adopt the U_r channel as a measure of our errors, recognizing that the contribution of both noise and potential signal renders it a conservative estimate.

The spectral mode data were PSF-subtracted using the pyKLIP software (Wang et al., 2015a)[1]. pyKLIP combines both Spectral Differential Imaging (SDI: for spectral mode data) and Angular Differential Imaging (ADI) using the Karhunen-Loeve Image Projection (KLIP) algorithm (Soummer et al., 2012). Due to the face-on nature of the

[1]https://bitbucket.org/pyKLIP/pyklip

disk, recovery of the total intensity is difficult via ADI. We leave forward modeling of the disk's total intensity surface brightness, and calculation of the polarization fraction, to future work.

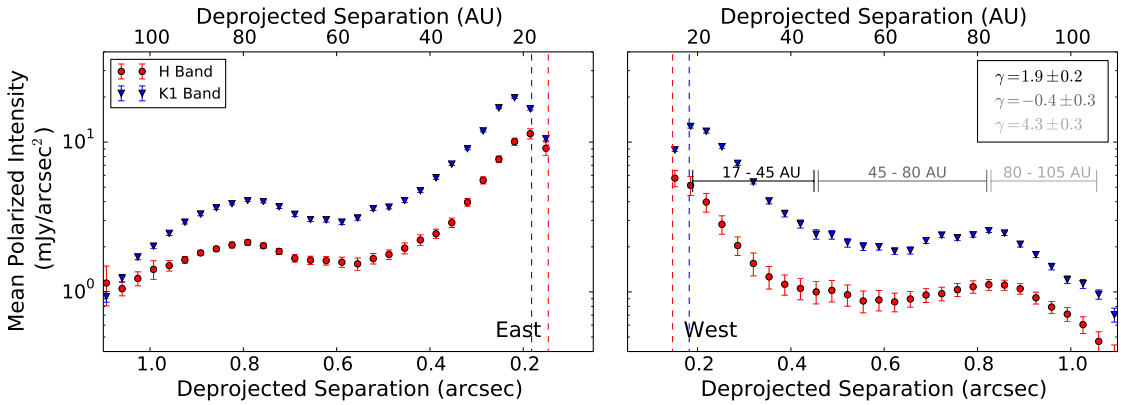

Figure 4.2 Radial brightness profile of the tangential polarized intensity for *H* and *K1* bands for the East (left) and West (right) sides of the disk. Vertical dashed lines indicate the outer edge of the coronagraphic spot in *H* and *K1* bands. Fits to the power law slopes (γ) are given in the legend (E/W slopes agree). Error bars are drawn from the U_r error maps. The profile shows the bright inner ring of material and a peak at $\sim 0.8''$ (80 AU) corresponding to the outer ring.

4.3 Disk Morphology

The GPI data reveal a bright disk interior to a more diffuse disk extending to an outer ring, and an azimuthal asymmetry indicative of interesting structure close in to the central star (Figure 1). We also show the STIS data provided by Schneider et al. (2014) to illustrate the fainter outer halo outside the field of view of GPI. The inner disk likely extends from the sublimation radius to the change in the power law

slope at 45 AU. The region between the inner disk and outer ring (45 – 80 AU) is not entirely cleared, as evidenced by the azimuthal orientation of the polarization vectors.

We fit an ellipse to the brightness contours in the outer disk ring using the constrained, linear, least squares method described in Fitzgibbon & B. (1996). We find a position angle for the disk major axis of $10^\circ \pm 3^\circ$ E of N, an axial ratio of 0.86 ± 0.02, and a disk inclination of $31^\circ \pm 2^\circ$ from a face on viewing geometry. These values agree well with the STIS results (minor:major axial ratio 0.889 ± 0.026, inclination 27.3 ± 3.3 degrees: Schneider et al., 2014). We measure no stellocentric offset to within 30mas, consistent within errors with the offset in the STIS observations of 33 ± 10 mas (Schneider et al., 2014). Low SNR in the satellite spots of these observations limits our knowledge of the obscured star's location to within ~ 2 pixels.

We deproject the disk and calculate a radial brightness profile (Figure 2) separately for the East and West sides of the disk. Note that the peak in surface brightness is slightly offset from the edge of the coronagraphic mask. This is likely due to a lower throughput from an instrumental effect rather than a decrease in the surface density of the disk (See also Rapson et al., 2015b). The East side of the disk is brighter in both total intensity (STIS/NICMOS) and polarized intensity (GPI). Since we expect the dust particles in the disk to be predominately forward scattering, we conclude that the East side is the nearer side. We fit power laws $\propto r^{-\gamma}$ to the surface brightness profile in the inner disk, the central region, and the outer ring (see Figure 2). The power law slope in the inner disk is consistent with an optically thick, gas-rich disk.

For the outer component (80 – 105 AU), the GPI power law fit agrees well with the STIS and NICMOS result (Cortes et al., 2009).

After correcting for extinction ($A_V = 0.7 \pm 0.2$ mag; Cortes et al. (2009)) and stellar color (assuming a K1 spectral type with intrinsic H-K = 0.14), the azimuthally-averaged apparent color of the disk is $H\text{-}K = 0.45 \pm 0.17$ in polarized intensity, implying that the dust in the disk is $\sim 50\%$ more effective at reflecting *K1* band light than *H* band light. In *H* band, the East side of the disk is 2.1 times brighter than the West side, while the East side is only 1.6 times brighter than the West in *K1* band. The E/W flux ratio is much lower than seen in total intensity in the visible (Schneider et al., 2014), which suggests either more isotropic scattering and/or a high polarization fraction on the (fainter) W side.

A region within the south side of the disk appears depleted in polarized intensity in both *H* and *K1* bands. Figure 3 shows the azimuthal brightness variations for two disk annuli (35 – 50 AU and 70 – 90 AU) computed from the mean and standard deviation in 12° wedges. In the 35 to 50 AU region, there is a $\sim$ 35 % decrease in the surface brightness from PA $160° - 220°$ (measured E from N). Schneider et al. (2014) also saw brightness asymmetries of $\sim 30\%$ between two epochs of data spaced three months apart. Though at a different parallactic angle, the drop in brightness subtends approximately the same angular fraction of the disk.

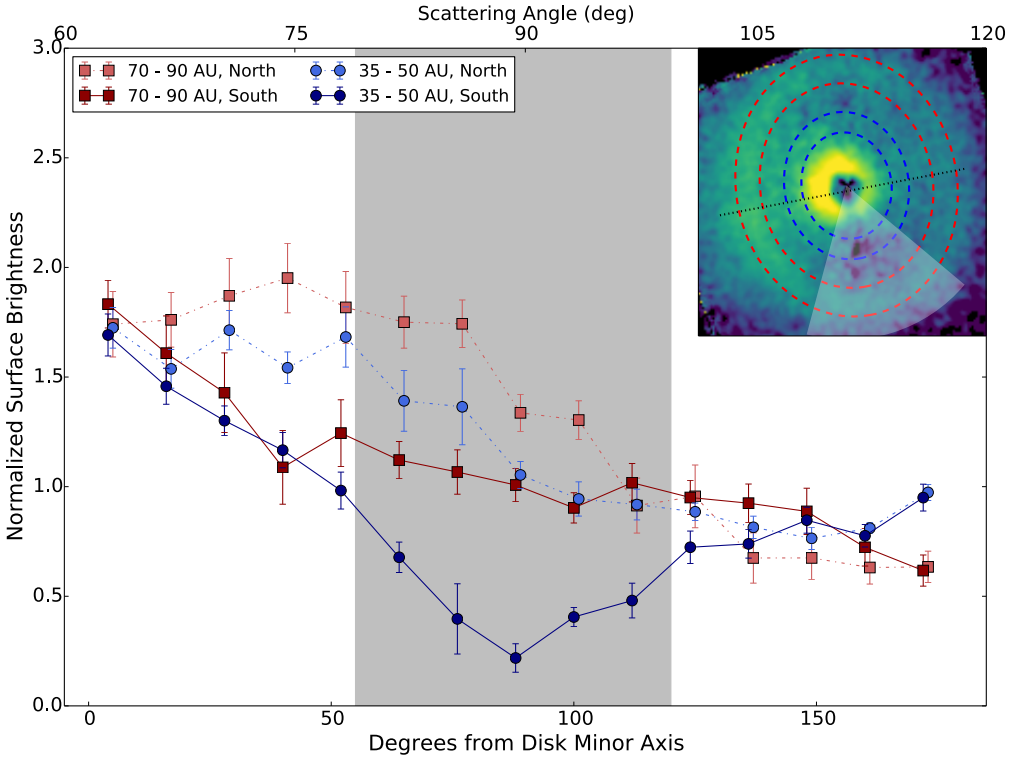

Figure 4.3 The azimuthal variation of the median polarized intensity as measured for the H band GPI data in an annulus in the gap from 35 to 50 AU and for the bright ring from 70 to 90 AU. The North and South polarized intensities are plotted separately to emphasize the drop in flux seen on the South side of the disk. Polarized intensity values have been normalized to the mean separately for each ring. The inset shows the H band image (North up). The dashed blue/red lines represent the annulus used to measure the azimuthal variation. The black dotted line gives the location of the disk minor axis. The gray shaded region corresponds to the shaded inset wedge.

4.4 Planetary Companion Limits

Our spectral data constrain planetary companions of a given mass and age. We compute a 5σ contrast curve assuming a methane dominated planetary spectrum. We achieve a contrast of $\sim 10^{-5}$ outside of $0.3''$ and $\sim 2 \times 10^{-6}$ outside of $0.4''$. We detect no planetary candidates, but we recover a bright source in the north at 50σ, which was previously confirmed as a background source (Schneider et al., 2014; Cortes et al., 2009).

Planet sensitivities are calculated following Nielsen & Close (2010) and Nielsen et al. (2008) (Figure 4). The contrast curve is used to set companion brightness limits with radius. The brightness of a planet with a given mass and age are set by the hot start evolutionary tracks of Baraffe et al. (2003). For an age of 7 Myr and a distance of 100 pc (ϵ Cha membership) there is a 90 % confidence that we would have detected a 8 M_{Jup} planet at $\sim$ 20 AU or a 3 $M_{\rm Jup}$ planet outside of 40 AU. At 17 Myrs and 86 pc (LCC membership), the 90 % confidence limits increase to a 10 $M_{\rm Jup}$ planet at $\sim$ 20 AU. Planetary companions may exist, but lack a methane absorption feature, or could be low-mass enough to remain hidden below the opaque disk surface.

4.5 Discussion

PDS 66 joins the class of pre-transitional disks (Espaillat et al., 2010) with an optically thick inner disk separated from an outer disk by a dip in surface brightness

around 0.5″ that could indicate a partial clearing of the disk. The gap/ring structure observed in our GPI data, combined with the detection of orbiting CO (Kastner et al., 2010) confirm that PDS 66 closely resembles the V4046 Sgr and TW Hya systems. All are nearby cTTS that have retained their molecular gas to late ages and show multi-ringed structures. GPI polarimetry was used to confirm the presence of scattering dust in the gaps of the V4046 Sgr multi-ringed structure (Rapson et al., 2015a). TW Hya is multi-ringed with partially filled gaps as well (Debes et al., 2013).

If the disk is optically thick, the ring/gap structure is a result of a variation in the disk surface that could be caused by a change in the surface density, the local scale height, or the dust properties of the sub-micron sized grains in the disk. Here we discuss possible sources for a change in the disk surface properties:

1. *Gap Opening Planets:* A planet/(s) in the low surface brightness region could induce a gap in the dust disk and deplete the gas (Dong et al., 2015). Dust filtration is efficient at piling up larger dust particles (mm-sized) into a ring at the pressure bump outside of a gas gap (Zhang et al., 2015), while smaller grains (responsible for scattered light) could still populate the gap. Given the observed width ($\sim$ 35 AU) and the shallow depth (ring:gap = 1.4), this is most likely a planetary system with several sub-jupiter mass planets.

2. *Disk Shadowing:* A scale height enhancement in the inner part of the disk shadows the outer disk, until the flaring of the disk eventually brings the disk surface above the penumbra. Dong (2015) find that a puffed up inner wall can

create a three part broken power law in the radial brightness profile, as seen in the GPI data. A shadow cast out to 80 AU would require a flat disk and/or a low flaring exponent.

3. *Dust Particle Properties:* A localized change in the dust properties would change the opacity of the disk. Dust settling due to grain growth could induce a change in the scale height, which would change the height of the scattering surface relative to the disk midplane, producing the bright ring. Gaps in the HL Tau disk have been ascribed to the effects of snowlines (Zhang et al., 2015). However, given the large radius of the observed ring (80 AU), this seems unlikely.

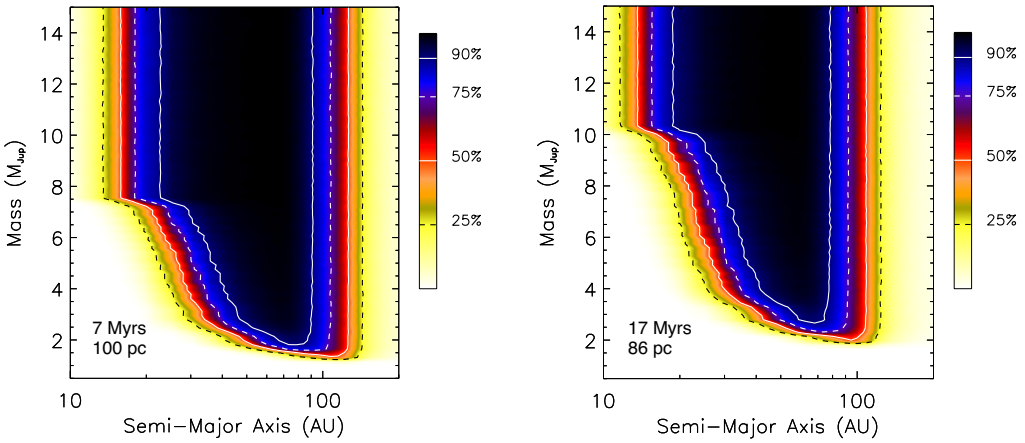

Figure 4.4 Companion sensitivity as a function of separation and mass for membership in ϵ Cha (Left) and the LCC (Right) with ages and distances as shown.

For an inclined disk that is optically thick vertically and axisymmetric, a ring with

a higher surface height would appear as an offset structure relative to the central star (Lagage et al., 2006). Combining the offset measured in the STIS image with the ring radius, we infer that the scattering in the ring occurs 4 AU above the disk midplane. The expected scale height for gas in vertical hydrostatic equilibrium at the location of the ring is about 4–5 AU (assuming $T_{eff} = 5000\,\mathrm{K}$, $L = 1.1 L_\star$ and $T_{80\mathrm{AU}} = 10-15\,\mathrm{K}$), i.e. similar to the height where scattering occurs. In optically thick disks, the disk surface is typically located 2–4 times higher than the gas scale height (e.g., D'Alessio et al., 1999). This suggests that the PDS 66 disk is flatter and/or less flared than primordial disks, i.e., possibly significantly settled as was originally suggested by Cortes et al. (2009). A flattened disk could favor the "shadowing" scenario above, but only a more complete SED+image modeling effort can confirm this.

From this dataset, no clear conclusions can be drawn on the origin of the gap + ring structure. ALMA dust continuum observations would help distringuish between the scenarios above. For scenario (1), we would expect to see a significant pile up of mm-sized grains right outside the NIR ring, due to the dust filtration effect, which would generate at least a factor of ~ 10 or higher in continuum flux. In scenario (2), the shadowed region would have a slightly lower temperature, which would result in less flux in the optically-thin mm continuum as well, though only on the order of $\lesssim 50\%$. ALMA gas observations may be able to detect gas depletion in the scenario (1), however given the shallowness of the gap this may not provide sufficient contrast between shadowed and unshadowed regions.

We detect an azimuthal departure from axisymmetry, seen as a dimmer region in the disk's southern side at around a 40 AU radius. Schneider et al. (2014) observed that the east/west asymmetry of the disk is variable on timescales as short as three months (Schneider et al., 2014). Since this is much shorter than the dynamical timescales at the relevant orbital separations, Schneider et al. (2014) hypothesized that the changes could be due to either time-variable shadowing from material in the inner disk hidden behind the coronagraphic mask, or localized accretion hot spots on the stellar photosphere. It is possible that the azimuthal asymmetry seen in the GPI data (at $\sim$ 40 AU) is due to such an effect, rotated around to affect the illumination over a different range of position angles. Density enhancements in the disk caused by accreting protoplanets might cast shadows on the outer regions of the disk, though the shadowed areas predicted by simulations for planets as massive as 50 M_{Earth} are only $\sim 7\,AU^2$ (Jang-Condell, 2009). Alternatively, cold spots on the stellar surface which are darker due to magnetic suppression of convection typically cover 5 - 30% of the stellar surface and could cause an azimuthal modulation of the stellar illumination incident on the outer disk on stellar rotation timescales (Venuti et al., 2015).

If the azimuthally variable disk surface brightness distribution is due to nonuniform brightness on the stellar surface, it will change on timescales of the rotation period (5 days). If instead it is due to material orbiting at the estimated inner radius (10.5 days at 0.1 AU) or embedded in the bright inner ring the shadowing will vary over a longer period. More data is needed to elucidate the timescales of the

azimuthally variable disk surface brightness.

Chapter 5

An upper limit on the mass of the circum-planetary disk for DH Tau b

Abstract

DH Tau is a young (∼1 Myr) classical T Tauri star. It is one of the few young PMS stars known to be associated with a planetary mass companion, DH Tau b, orbiting at large separation and detected by direct imaging. DH Tau b is thought to be accreting based on copious Hα emission and exhibits variable Paschen Beta emission. NOEMA observations at 230 GHz allow us to place constraints on the disk dust mass for both DH Tau b and the primary in a regime where the disks will appear optically thin. We

estimate a disk dust mass for the primary, DH Tau A of $17.2 \pm 1.7\,M_{\oplus}$, which gives a disk-to-star mass ratio of 0.014 (assuming the usual Gas-to-Dust mass ratio of 100 in the disk). We find a conservative disk dust mass upper limit of $0.42 M_{\oplus}$ for DH Tau b, assuming that the disk temperature is dominated by irradiation from DH Tau b itself. Given the environment of the circumplanetary disk, variable illumination from the primary or the equilibrium temperature of the surrounding cloud would lead to even lower disk mass estimates. A MCFOST radiative transfer model including heating of the circumplanetary disk by DH Tau b and DH Tau A suggests that a mass averaged disk temperature of 22 K is more realistic, resulting in a dust disk mass upper limit of $0.09 M_{\oplus}$ for DH Tau b. We place DH Tau b in context with similar objects and discuss the consequences for planet formation models.

5.1 Introduction

With well over 3000 confirmed extrasolar planets now known, the focus of exoplanet science is shifting from their discovery to understanding the details of their formation and evolution. However, increasing our understanding of this complex process can only be achieved with unambiguous detections of planetary mass bodies still in formation. Today, a handful of good candidates are known (Kraus & Ireland, 2012; Sallum et al., 2015; Biller et al., 2014; Reggiani et al., 2014; Quanz et al., 2015), but they are still embedded deeply in the circumstellar disk and also located close to the

central objects. These are challenging conditions to study the processes that lead to their formation.

Fortunately, a small population of planetary mass companions (PMCs) has recently been discovered that offers a much better opportunity to study the planet formation process in greater details with current instruments. These PMCs, identified by direct imaging surveys in the NIR, orbit very young host stars (T Tauri stars) and they do so at large enough separations to be easily observable, typically several hundred au ($\sim$ 1 arcsec) (e.g., Neuhäuser et al., 2005; Lafrenière et al., 2008; Schmidt et al., 2008; Ireland et al., 2011; Bailey et al., 2014).

While planets at separations of $<$ 100 au are thought to be the consequence of either core accretion (Lissauer & Stevenson, 2007) or gravitational instabilities (Boss, 1997, 2011) acting at the Class II stage (i.e., T Tauri stage), planets at larger separations are believed to be products of disk fragmentation at an earlier stage (Class 0 or I stage, Kratter et al., 2010). All these mechanisms require that a forming planet builds up from its own circumplanetary disk that formed either from the surrounding cloud, or from the massive disk around the host star. Indirect evidence for the presence of such disks is provided by the fact that planet-mass companions in young systems are powerful Hα emitters, e.g., OTS 44, GSC 06214-00210 b, GQ Lupi b, FW Tau c, DH Tau b (Joergens et al., 2013; Zhou et al., 2014). The Hα emission, or some portion of it, being the trace of accretion from the disk onto the companion. The more direct detectability of these circumplanetary disks was recently demonstrated

when ALMA measured the continuum and CO emission around the PMC orbiting the TTauri binary FW Tau (Caceres et al., 2015). The disk around FW Tau C (the PMC) has an estimated disk mass of 2-3 $M_{\oplus}$. Attempts have been made to resolve the circumplanetary disks around several other PMCs with radio interferometer (e.g., GSC 0614-210 B; Bowler et al. 2015, GQ Lupi; Dai et al. 2010, MacGregor et al. 2016), but no other detections exist to date.

The DH Tau System

DH Tau is a binary system with a projected separation of 330 AU (2."3). The system is located in the Taurus star forming region at a distance of 140 pc, with an extinction in the J band of $A_J = 0.3 \pm 0.3$ (Itoh et al., 2005), and a mean age of 2.3 Myrs (Bertout et al., 2007). The primary is a classical T Tauri star with an M1Ve spectral type (Herbig, 1977) with $\log(T/K) = 3.5688 \pm 0.0170$ and $\log(L/L_{\odot}) = -0.262 \pm 0.110$ (Andrews et al., 2013). DH Tau b was initially discovered by Itoh et al. (2005), who classified it as a L2 spectral type brown dwarf with a mass of $30 - 50\,M_{Jup}$. Luhman et al. (2006) later compared bolometric luminosities to updated evolutionary tracks and gave a revised mass estimate of $11^{+10}_{-3}\,M_{Jup}$, placing it near the exoplanet/brown dwarf boundary. Patience et al. (2012) modeled the atmosphere using *J, H,* and *K* spectra, and inferred a radius for DH Tau b of $2.7 \pm 0.8\,R_{Jup}$, and a temperature of 2350 ± 150 K. Bonnefoy et al. (2014) give a spectral type for DH Tau b of M9.25±0.25 (corresponding to $15\,M_{Jup}$).

DH Tau b is the youngest PMC known to date. It is known to be actively accreting,

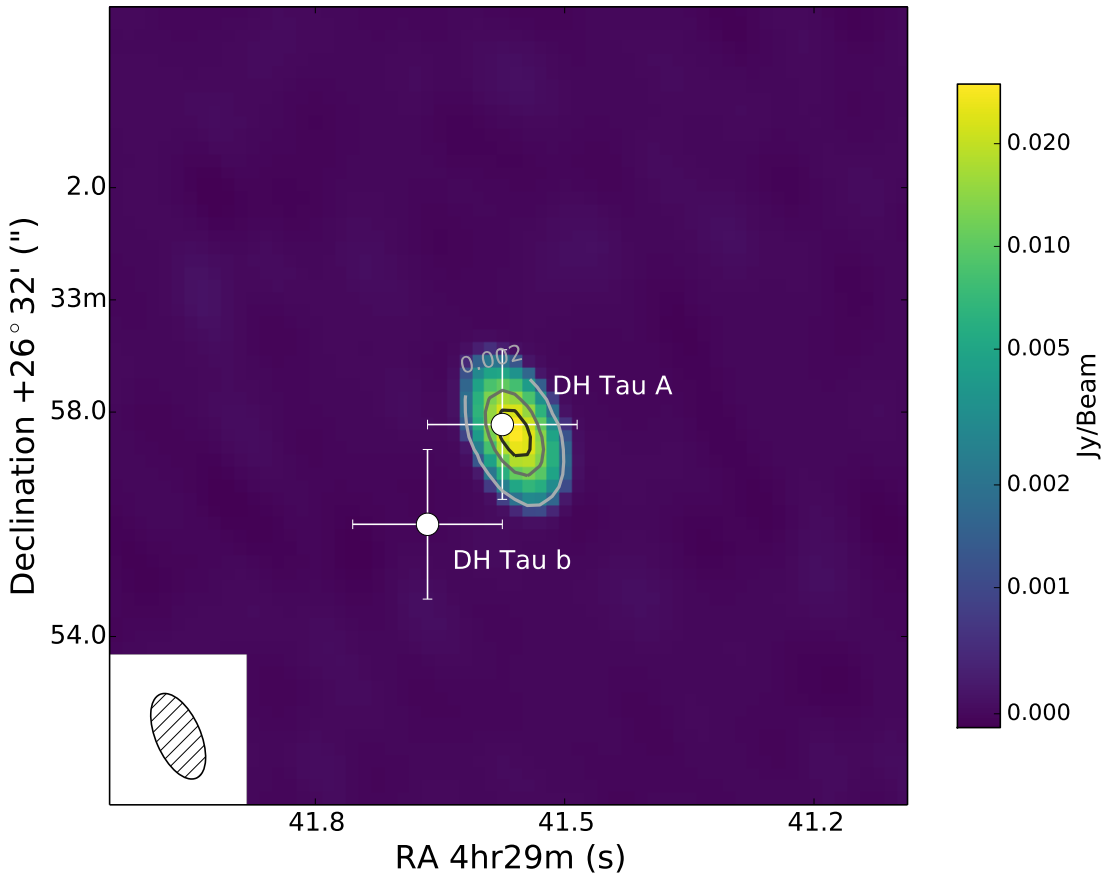

Figure 5.1 1.3 mm continuum NOEMA observations of the DH Tau system. The disk of DH Tau A is clearly detected, but is unresolved. The disk of DH Tau b is undetected. Contours are drawn beginning at 0.002 Jy/beam in intervals of 0.01 Jy/beam. The errors in the positions of the DH Tau A and b components are dominated by the proper motion uncertainties. The symmetric sidelobes are an artifact of the baseline configuration. The inset shows the beam with a PA of 27.8°, a major axis of 1.61," and a minor axis of 0.79."

as traced by very strong Hα emission (Zhou et al., 2014). The Paβ line of Hydrogen is also reported, in emission, by Bonnefoy et al. (2014) further supporting the idea that DH Tau b is still accreting. DH Tau as a system also displays unresolved MIR excess which, given the accreting nature of DH Tau b, is likely caused in part by the circumplanetary disk. Harris et al. (2012) reported a 47 mJy detection around the DH Tau primary at 0.88 mm. Their observations with the SMA only provided a 3σ upper limit of 10 mJy at 0.89 mm for DH Tau b. The circumplanetary disk has remained undetected to date.

In Section 5.2, we present the NOEMA observations of the DH Tau system and the VLT/SINFONI spectroscopy of the Paβ Hydrogen line. Section 5.3 presents the upper limits on the disk mass of DH Tau b, an estimated disk mass for DH Tau A, and the disk model used. Finally, in Section 5.4 we discuss the disk mass results and place them in context with other observations of circumplanetary disks.

5.2 Observations

5.2.1 NOEMA 1.3mm continuum imaging

The data presented in Fig. 5.1 were obtained with NOEMA, the NOrthern Extended Millimeter Array. The observations were carried out on December 10th, 2015. At that time the array was in the 7C compact configuration, with 6 antennas operating. Station W09 was off-line. Antennas were based on stations E12, N17, N11,

E18, W12, and E04. The resulting 15 baselines ranged from 48m to 240m in length (unprojected). DH Tau and its companion were observed for a total of 6.5 hours between hour angle -0.3h and +6.0h, of which 4.5 hours we spent on-source. The rest of the time was used for calibration.

We used 0400+258 and 0507+179 as phase calibrators. The atmospheric conditions were excellent and the rms phase noise was measured between 12^o on short baselines and 29^o on long baselines, at 1.3 mm. This phase noise introduces a position error of less than 0.1 arcsec. The source LkHa 101 was used for the flux calibration, while 3C84 was used for the bandpass calibration. We consider an absolute flux uncertainty of 10%. The total bandpass for the 230.5 GHz continuum measurement was 3.2 GHz in each polarisation. We excluded a short range (80 MHz) that included the CO(2-1) line. The GILDAS software package was used to reduce the data.

The continuum map was produced using natural weighting of the visibilities to favour signal-to-noise over angular resolution. The resulting beam size is $1.''61 \times 0.''79$ at P.A. 28^o. High signal-to-noise on DH Tau A allows for phase self-calibration. This allowed us to correctly remove side-lobes that remained present after the first reduction steps. We do not perform amplitude self-calibration in order to preserve the absolute flux measurement. The phase self-calibration stopping criteria was set to 1000 iterations. From the visibilities, we compute the stable thermal noise limit (absolute flux limit) to be 0.0653 mJy. Any residuals after self-calibration correspond to a lack of uv coverage that is impossible to correct.

We find a 1σ flux limit of 0.0653 mJy/beam for the 1.3 mm continuum data, which corresponds to a 3σ upper limit for the DH Tau b circumplanetary disk flux of 0.196 mJy. Primary beam attenuation was not taken into account because of the small separation between DH Tau A and DH Tau b (beam attenuation <2% at the position of DH Tau b). We detect the central component of the system, DH Tau A, at $> 100\sigma$, with an integrated disk flux of 30.8 ± 0.2 mJy.

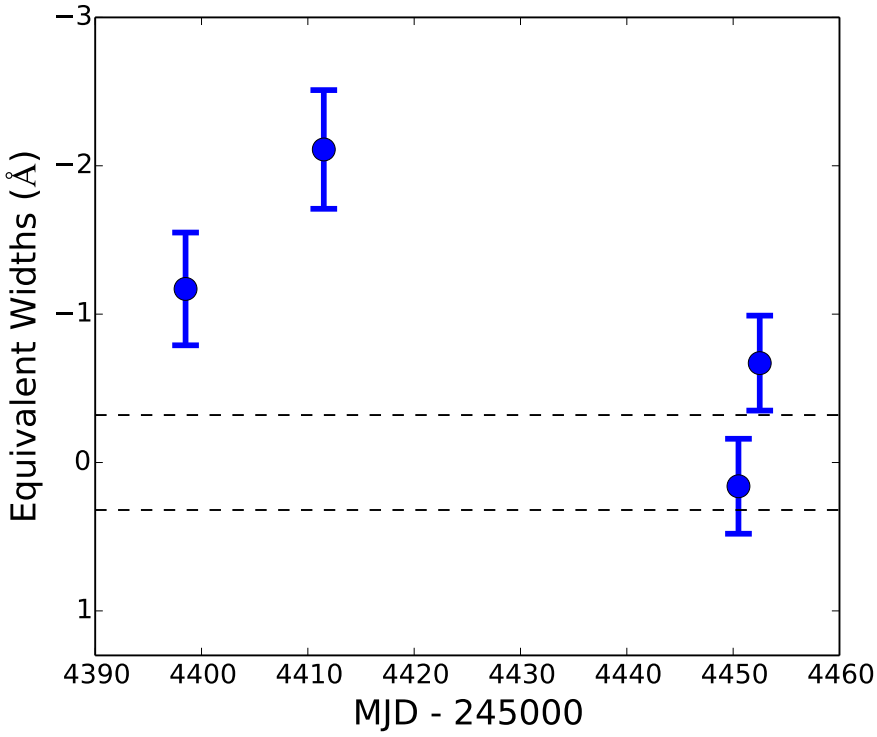

Figure 5.2 Variability of the Pa β equivalent width with time provides further evidence of an accreting circumplanetary disk surrounding DH Tau b. The dashed lines represents the mean 1σ error for the equivalent width measurements.

5.2.2 VLT/SINFONI spectroscopy of the Paschen β Hydrogen line

DH Tau b was observed with the VLT/SINFONI instrument on Oct. 25th, Nov. 7th, Dec. 16th, and Dec. 18th, 2007 (program ID 080.C-0590(A)). SINFONI is composed of an integral field spectrograph SPIFFI fed by the adaptive optics module MACAO (Eisenhauer et al., 2003; Bonnet et al., 2004). The instrument was operated with the J-band grating yielding a spectral resolution of ∼2000 over the 1.1-1.35 μm range. The pre-optics was sampling the 0.8×0.8" field-of-view with a spaxel size on sky of 12.5×25 mas. Each sequence is composed of 8×300s exposures with small dithering and one acquisition on the sky at the end to ensure a proper removal of the sky emission. Telluric standard stars were observed after DH Tau on each night to estimate the contamination by telluric features in the companion spectra. Because the Paschen β line is not significantly affected by telluric lines in our spectra, we decided not to correct for telluric features in order to avoid adding noise to our spectra. The October, November, and December 16 data were published in Bonnefoy et al. (2014). We reduced the December 18 data with the same tools as used in Bonnefoy et al. (2014) in order to get a homogeneous set of extracted spectra of the companion.

A Paschen β emission line is detected in the November observations, marginally detected in October, and not detected in December. All spectra have a comparable estimated S/N between 1.29 and 1.31 μm[1]. We estimated the equivalent width of the

[1]The S/N was computed in a two step process. We first interpolated the IRTF spectrum of the

Table 5.1 Equivalent width of the Paschen β line

MJD Date - 245000	S/N	Eq. Width (Å)
4398.5	16	-1.17±0.38
4411.5	18	-2.11±0.40
4450.5	20	0.16±0.24
4452.5	19	-0.67±0.32

line following the method of Sembach & Savage (1992). The continuum was estimated in a range adjacent to the line, between 1.277 and 1.281 μm, and between 1.283 and 1.287 μm. The equivalent width is computed between 1.281 and 1.283 μm. The values are reported in Table 5.1 and their evolution in time is shown in Figure 5.2.

Assuming the Paβ line in emission is tracing accretion of material onto DH Tau b, then the results presented in Table 5.1 and Figure 5.2 provide indications that the accretion process itself may be variable in time. This is reminiscent of the well documented variability of the accretion process in more massive T Tauri stars, e.g., Sousa et al. (2016). The poor time coverage for the spectral variations of DH Tau b forbids a deeper analysis. We do not discuss further the variability of accretion in DH Tau b, but note it is very likely present.

M9 dwarf LP 944-20 on the SINFONI wavelength grid and normalized it in flux to the flux of the pseudo-continuum of DH Tau b over the 1.29-1.31μm range. We used this template spectrum to approximate, then remove, all the intrinsic features of the DH Tau b (FeH lines mostly) and compute the local level of the noise.

5.3 Circumplanetary Disk Models and Results

In this section we present models for the dust mass estimates extracted from the 1.3 mm continuum NOEMA data. We will consider three cases: the disk of DH Tau b is heated by DH Tau b only; the disk is heated by DH Tau A; and the disk is in equilibrium with the ambient cloud (assumed at 20 K). To test the dominant source of the disk dust temperature, we combine the contributions from DH Tau A and DH Tau b using a radiative transfer model.

We expect the disk to be optically thin at 1.3 mm. In this case, the disk dust mass can be expressed as

$$M_{dust} = \frac{F_\nu D^2}{\kappa_\nu B_\nu(T_{\rm disk})}$$

where F_ν is our measured $\nu = 230\,GHz$ (1.3 mm) 3σ flux limit, D is the distance (140 pc), κ_ν is the dust opacity, and $B_\nu(T_{\rm dust})$ is the Planck function evaluated at the disk temperature. We use the dust opacity law from Beckwith et al. (1990); $\kappa_\nu = 10\,(\nu/10^{12}Hz)^\beta\,cm^2g^{-1} = 2.3\,cm^2g^{-1}$ for frequency, ν, and power law index, $\beta = 1$.

Typical disk temperatures are ~ 20 K, but this varies with stellar luminosity. For DH Tau b, we calculate a luminosity of 0.0021 $L_\odot$ using the radius and stellar temperature (Zhou et al., 2014). van der Plas et al. (2016) provide a scaling relation between

stellar luminosity and disk temperature for low mass stars; $T_{\rm disk} = 22(L/L_{\odot})^{0.16}\,K$, which gives a disk temperature for DH Tau b of 8.2 K.

It is worth noting here that the temperature of molecular clouds is typically in the range of 10 - 20 K (Goldsmith, 1987). In this case, the temperature of the disk may depend more on the ambient temperature from the Taurus SFR than the central source. Likewise, DH Tau b is located nearby to the much more luminous DH Tau A primary, with a luminosity of $0.55\,L_{\odot}$ and an effective stellar temperature of $T_* = 3706$ K (Andrews et al., 2013). If we treat the dust as a blackbody in thermal equilibrium with the central star, DH Tau A, at the distance of DH Tau b (330 au) with a circumplanetary disk albedo of a = 0.5, we expect the equilibrium temperature to be $T = T_*(1-a)^{1/4}\sqrt{R_*/2D} = 11\,K$. Depending on the orientation of the disk relative to the central star and/or the optical depth of the disk, there could be some additional heating due to illumination from the primary, DH Tau A. Viscous heating due to accretion could also raise the temperature of the disk and serve as another source of uncertainty in the dust mass estimate.

We reproduce the effect of the host star on the disk dust temperature by generating an MCFOST radiative transfer model of the system (Pinte et al., 2006, 2009). MCFOST is a Monte Carlo Radiative Transfer code designed to study circumstellar disks. At each grid location in the modeled disk, the temperature and scattering source function are computed via a Monte Carlo method: photon packets are propagated stochastically through the model volume following the equations of radiative

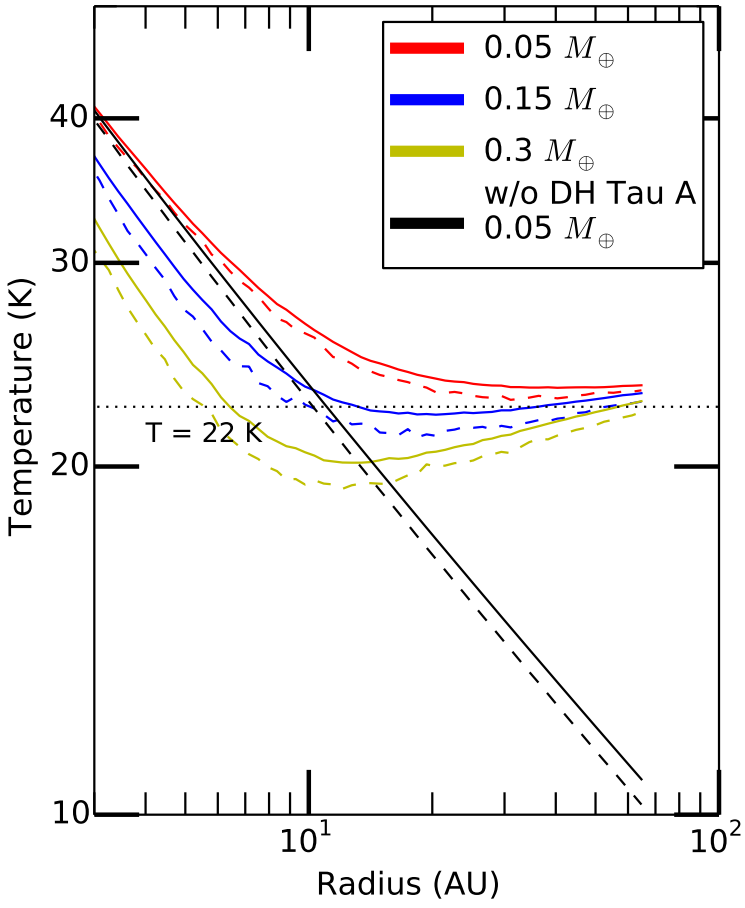

Figure 5.3 Dust temperature profile for the set of MCFOST radiative transfer disk models with different disk dust masses. The dashed lines show the radial profile of the disk midplane temperature, while the solid lines show the radial profile of the mass-averaged dust temperature. As the mass increases, the disk becomes more optically thick to radiation and the temperature decreases. At the outer edges of the disk, all dust mass models converge to a mass-averaged dust disk temperature of 22 K (as indicated by the dotted line).

transfer. MCFOST allows the user to include multiple radiative sources, allowing the inclusion of the DH Tau A primary located 330 au from the circumplanetary disk. DH Tau A was modeled using an effective temperature of 3700 K and a low surface gravity of $\log(g) = 3.5$, while DH Tau b was assumed to have an effective temperature of 2300 K with $\log(g) = 3.5$. For DH Tau b, we assume an axisymmetric disk model with a gas supported flaring exponent of 1.125, and a surface density described by a power law in radius with an index of -0.5. The grains are comprised of astronomical silicates with a grain size distribution defined by an ISM-like -3.5 power law exponent and grain sizes ranging from 0.1 to 1000 μm. The resulting dust opacity is 2.29 cm^2/g, similar to the dust opacity of 2.3 cm^2/g predicted above for an optically thin disk. We assume a gas-to-dust mass ratio of 100 and a distance of 140 pc. For simplicity DH Tau b receives light directly from DH Tau A without attenuation, as if DH Tau b was located out of plane from the disk of DH Tau A.

The typical value for the outer radius of a circumplanetary disk is not well constrained. Numerical simulations of embedded circumplanetary disks suggest that the radii truncate at a fraction of the Hill radius due to interactions with the viscous, young circumstellar disk (Ward & Canup, 2010). For DH Tau b, the Hill radius is $R_{\rm Hill} = a(\frac{M_p}{3M_*})^{1/3} \simeq 70$ au for the planetary mass and separation ($M_p = 11\,M_{Jup}$, $a = 330$ au respectively) given in the introduction, and the primary star mass (M_*) of $0.37 \pm 0.12\,M_\odot$ from Itoh et al. (2005). Alternatively, if the DH Tau b disk formed from the collapse of the surrounding cloud, it would be expected to have a larger

radius. Schaefer et al. (2009) survey the disks of young, low mass stars in the Taurus-Auriga star-forming region and find a range in disk outer radii of $R_{\rm out} \sim 100 - 1000$ au from resolved CO emission. However, a larger disk would be truncated due to the presence of the primary at a $\sim$ 0.3 - 0.5 fraction of the 330 au separation (Papaloizou & Pringle, 1977). A disk truncated at 110 au (diameter $\sim 1.6''$) is roughly the same size as the beam along the major axis ($1.61''$). In either case, this is below the beam size, and we treat the disk as a point source in our data. For the MCFOST model, we define the disk outer radius to be the Hill radius of 70 au.

The model was tested for several disk dust masses covering the range predicted for the various dust temperatures, and for different orientations of the circumplanetary disk with respect to DH Tau A. We found that the disk orientation (e.g., face-on, edge-on, or intermediate illumination from the central star) has no measurable effect on the azimuthally averaged dust temperature. Figure 5.3 shows the mass-averaged temperature profile for three assumed disk masses and includes for comparison a disk model without the host star included. As the disk dust mass increases, the mid-plane temperature of the disk decreases as the disk becomes more opaque to radiation. In the outer regions of the disk, all MCFOST models converge on a dust disk mass-averaged temperature of $22 \pm 2\,K$, corresponding to a disk dust mass upper limit of $0.09 \pm 0.01\,M_{\oplus}$. This temperature and associated mass estimate is more consistent with what is expected for a disk in a young star forming region. We caution that assumptions in the disk model and the uncertainty in the separation of DH Tau b

could result in a lower dust temperature.

Table 5.2 gives the estimated disk mass upper limits for DH Tau b for the various temperatures described above. On the most conservative end, we provide an upper limit on the circumplanetary disk mass of 0.42 $M_{\oplus}$. However, the dust disk mass can likely be constrained further given the circumplanetary environment and as suggested by radiative transfer models of the system to be 0.09 $M_{\oplus}$. We adopt this upper limit for future discussion.

The temperature derived disk masses quoted above assume that the disk is optically thin at the 1.3 mm wavelength. If the disk were optically thick, i.e., $\tau > 1$ where $\tau = \int \rho \kappa_{\nu} ds = \kappa_{\nu} \Sigma > 1$, then the observed flux can be used to set a lower limit on the extent of the disk. Using the dust opacity law given above with $\beta \simeq 0$ for the optically thick case, the DH Tau b disk dust mass of 0.09 $M_{\oplus}$, and assuming a flat surface density we can constrain the radius of the disk: $R < \sqrt{\kappa_{\nu} M_D / \pi} < 2.9$ au. Therefore, if the disk were optically thick, it would have to be compact.

Using the same formalism with a midplane disk temperature of 20 K as predicted from the van der Plas et al. (2016) stellar luminosity relation for low mass stars, we estimate a disk dust mass for the primary, DH Tau A of $17.2 \pm 1.7\, M_{\oplus}$. The uncertainties are based on the absolute flux uncertainty and do not include errors in the assumed distance and disk opacity.

Table 5.2 DH Tau b Disk Dust Mass Upper Limits

Temp.	Dust Mass Limit	Source
20 K	$0.11 \pm 0.01\,M_\oplus$	Ambient cloud Temp.
8.2 K	$0.42 \pm 0.04\,M_\oplus$	DH Tau b Luminosity
11 K	$0.26 \pm 0.03\,M_\oplus$	Illumination from primary
22 K	$\mathbf{0.09 \pm 0.01\,M_\oplus}$	**MCFOST model**

5.4 Discussion

We are able to place an upper limit on the circumplanetary disk mass of the DH Tau b PMC. While the dust mass limit of $0.09\,M_\oplus$ is clearly not massive enough anymore to form planets, it still provides ~ 8 lunar masses of solid material to form satellites or minor bodies orbiting DH Tau b. The circumstellar disk surrounding DH Tau A has a dust mass of $17\,M_\oplus$, which is above the limit required to form giant planet cores ($\sim 10\,M_\oplus$), and could still support the formation of several terrestrial planets. The circumstellar disk mass is comparable to other Taurus disk masses for this spectral type, with a disk to star mass ratio of 0.014, assuming a gas to dust ratio of 100. The equivalent disk to star mass ratio for DH Tau b would require a total disk mass of $\sim 48\,M_\oplus$, which is not reproduced by even our most conservative detection limit for an uncharacteristically low mass averaged dust temperature.

For DH Tau b, the mass accretion rate predicted from Hα observations is $3.2 \times 10^{-12}\,M_\odot/yr$ (Zhou et al., 2014). Using the disk mass limit derived from the MCFOST model gives a disk dissipation timescale of 9.1 Myrs assuming a gas-to-dust ratio of 100.

5.4.1 Comparison to Known PMC Disk Masses

While there are not yet many disk mass estimates using millimeter continuum data for planetary mass objects, we compare these estimations for DH Tau b with the results for three other known wide separation PMCs: FW Tau C, GSC 6214-210 B, and GQ Lup B.

FW Tau The FW Tau primary is actually a binary system with two M5 stars orbiting at 11 AU, while the companion, FW Tau C has a mass of 7 M_{Jup} (Kraus et al., 2015). It is also in the Taurus SFR, with a similar age to DH Tau. Millimeter observations of the FW Tau system do not detect the circumbinary disk, but do detect the circumplanetary disk with an estimated dust mass of $\sim 2\,M_{\oplus}$ (Caceres et al., 2015). This dust mass is well above the average dust to stellar mass ratio for the Taurus SFR. The non-detection of the primary disk is unusual, though it is possible that the binary system caused the circumbinary disk to dissipate more quickly.

GQ Lup GQ Lup is in the Lupus 1 SFR, with a slightly older 3 Myr age (Lombardi et al., 2008; Alcalá et al., 2014). Dai et al. (2010) conduct SMA 1.3 mm observations of GQ Lup (a young, 1 Myr old T Tauri star) and detect the primary circumstellar disk with a mass of 3 M_{Jup}, but were unable to detect any disk signature around the secondary component. Recently published ALMA observations (MacGregor et al., 2017) detect a compact ($R_{\rm out} = 59 \pm 12$ au)

circumprimary disk with a higher dust mass estimate of $\sim 15\,M_{\oplus}$ from 870 μm continuum observations. The circumplanetary disk is not detected with a 3σ noise floor of 0.15 mJy/beam (equivalent to DH Tau b uncertainty) with a corresponding dust mass limit of $< 0.004\,M_{\oplus}$ calculated assuming that the dominant disk heating source is the primary. MacGregor et al. (2017) also obtain ^{12}CO and ^{13}CO emission showing a gas disk that extends outside of GQ Lup b. A recent multi-wavelength study of the GQ Lup system using both ALMA continuum observations and MagAO optical photometry of the companion show that the circumstellar disk of GQ Lup A is misaligned with the spin axis, possibly due to interaction with GQ Lup b (Wu et al., 2017).

GSC 0614-210 The circumplanetary disk around the 10 Myr old GSC 0614-210 B was not detected in ALMA continuum observations at 880 μm with a 3σ rms noise level of 0.22 mJy/beam (Bowler et al., 2015). This is comparable to the noise floor in these DH Tau observations, implying a similarly low disk mass ($< 0.15\,M_{\oplus}$). The circumstellar disk for the primary was not detected.

The dust masses and stellar/planetary masses for the objects listed above are shown in Figure 5.4. In the event of a non-detection in the millimeter, 3σ upper limits are provided. Included for comparison are the disk dust masses and stellar masses for a collection of objects in the Taurus (Andrews et al., 2013), Lupus (Ansdell et al., 2016), and Sco Cen (van der Plas et al., 2016) star forming regions. While the authors report the dust masses for the Lupus and Sco Cen circumstellar disks, the Taurus

dust masses were computed from the provided mm fluxes using the stellar luminosity and temperature relation described in Andrews et al. (2013).

5.4.2 Formation Mechanism?

We use the ensemble of known PMCs to place constraints on the planet formation process. Different formation pathways should produce different signatures in both the accretion rates and the planet to dust disk mass ratios as compared to their environments. Here we discuss the implications of the possible formation of these wide separation PMCs.

– Disk Instability:

  Models of giant planets produced via disk instabilities have difficulty producing massive planet cores outside of 100 au in all but the most massive disks. Vorobyov (2013) find that a protostellar disk mass of $\simeq 0.2\,M_{\odot}$ is needed to produce planetary embryos with masses in the range of 3.5 - 43 M_{Jup}. DH Tau A and GQ Lup A have dust disk to star mass ratios below average, while the circumstellar disks for FW Tau A/B and GSC 6214-210 A were not detected at all. As the oldest system, it is possible that the GSC 6214-210 A disk has already dissipated in its 10 Myr lifetime. However, this formation scenario is difficult to support with the current low disk mass estimates.

– Core Accretion + Scattering:

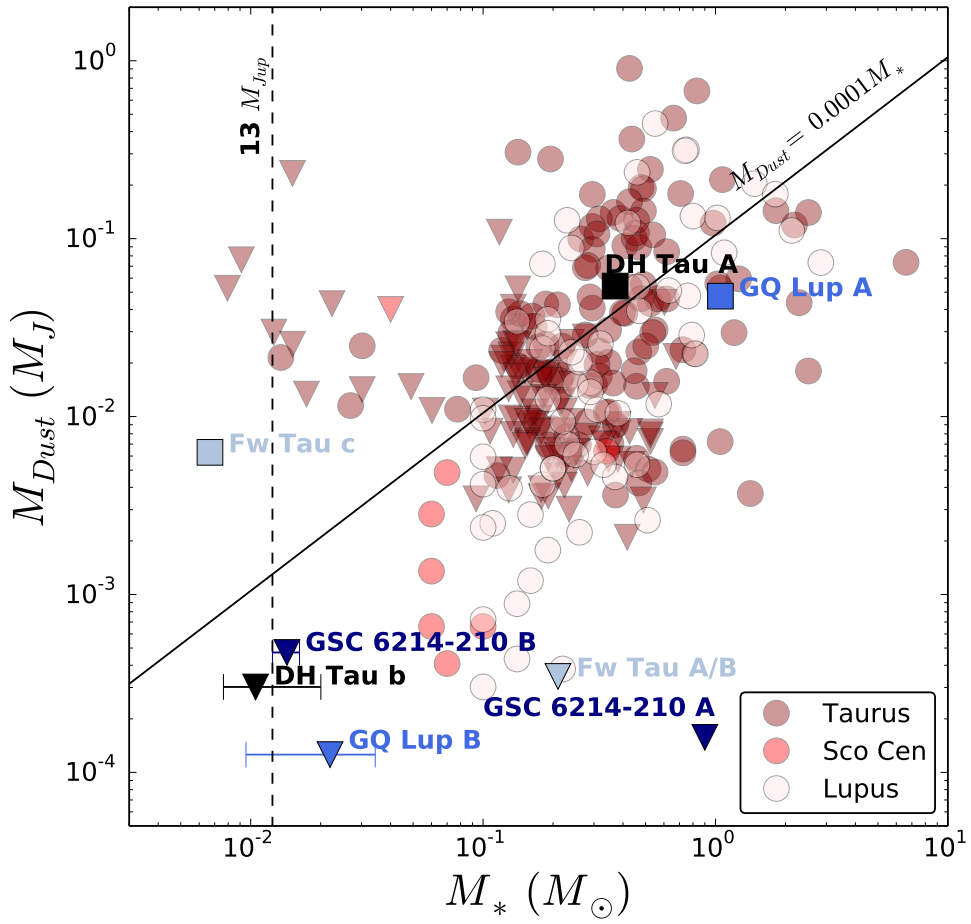

Figure 5.4 The disk dust mass and stellar mass are shown for a collection of labeled PMCs with dust mass estimates from mm observations. Dust to star mass ratios are shown in red for a collection of stars in the Taurus (Andrews et al., 2013), Lupus (Ansdell et al., 2016), and Sco Cen (van der Plas et al., 2016) star forming regions. 3σ upper limits are represented with triangles. The dashed vertical line represents the 13 M_{Jup} mass deuterium burning limit, while the solid diagonal line represents a 0.0001 $M_{\rm dust}/M_{\rm star}$ ratio. The disk dust mass estimates for the PMCs are generally lower than expected for the mass of the object with the exception of FW Tau C which has an exceptionally large dust mass.

The most commonly employed formation mechanism for gas giant planets is via core accretion of pebbles in the parent protoplanetary disk. However, generating giant planet cores massive enough to accrete gas in situ at wide separations requires timescales longer than the lifetimes of the gas in the disk (Lissauer & Stevenson, 2007). Alternatively, these planets could have been formed closer to their central stars and been dynamically scattered out to wider separations. None of the PMCs discussed here show evidence for a massive companion capable of dynamically scattering the PMC to wide separations. Indeed, direct imaging surveys of other wide separation PMCs do not find evidence for additional massive scattering companions and the core accretion + scattering event seems unlikely (e.g. Bryan et al., 2016). Surveys for scattering companions are limited by observational biases and this scenario cannot be ruled out.

A planet formed closer in but that has experienced such a dynamical scattering event that would now place it at a wide separation could potentially disrupt any circumplanetary disk. This scenario is supported by the low dust disk masses measured for all PMCs except FW Tau C, though their accretion signatures indicate that these disks are not entirely disrupted. Further monitoring of these systems to look for companions and/or signatures in their orbital properties indicative of a turbulent past could provide support to the core accretion + scattering model.

– Turbulent Fragmentation of the molecular cloud:

Through the process of turbulent fragmentation, filaments within dense molecular clouds gravitationally collapse to form protostellar/planetary cores as small as a few Jupiter masses (Low & Lynden-Bell, 1976). While this formation mechanism is capable of forming low mass objects and has been invoked to explain the formation of free-floating brown dwarfs, it is difficult to produce close binaries with such extreme mass ratios such as those between a host star and a planet (Bate, 2009, 2011). If the PMCs are formed from the gravitational collapse of the surrounding molecular cloud itself, and not formed in a circumstellar disk, we could expect the PMC to follow the same trend in planet to disk mass ratio as the parent star forming region. However, the relative disk to star/planet mass ratios do not appear to be correlated in binary systems, where the viscosity of the disk dictates the evolutionary timescales (e.g. Wu et al., 2017; Akeson & Jensen, 2014). This mechanism is not clearly supported by the DH Tau b and GQ Lup b observations. While the circumstellar disks are detected, with median disk to stellar mass ratios indicative of a young age, the PMC disks are less massive than expected. Turbulent fragmentation is also not a good fit for FW Tau C whose disk mass is well above the disk mass for the host binary, though photoevaporation from the binary may have removed the circumbinary disk, explaining the discrepancy in the disk masses.

Accretion rates provide another valuable indicator of formation mechanism. Bowler et al. (2011) provides a picture of accretion rates for PMCs in agreement with the

accretion rate-mass relation found for low-mass stars and brown dwarfs. In fact, the reported accretion rate for GSC 0614-210 B was above average when compared to a sample of similarly low mass brown dwarfs from Herczeg et al. (2009). Assuming these high mass accretion rates are indicative of large disk masses would seem to support formation via turbulent fragmentation. In addition, it seems that most PMCs located in young (< 10 Myrs), nearby star forming regions are accreting as has been seen for field brown dwarfs (e.g. Manara et al., 2015). Evidence of circumplanetary disks from accretion signatures alone rejects core accretion and subsequent scattering as a possible formation pathway, as it would cause a disk to dissipate. If indeed future observations using a larger sample size of PMCs show that they have "normal" accretion rates for their mass but small disk masses, this could serve as a valuable marker for formation scenario.

Unfortunately, no single planet formation model is capable of explaining the observed disk masses (and upper limits) for the ensemble of known wide separation planetary mass companions. Nonetheless, these are very exciting results as we are likely witnessing the very first stages of gaseous planet assembly. PMCs in general have the potential to offer unique insight into the early stages of extrasolar planet formation and to unveil, for the first time, the properties of circumplanetary disks. The observations of this type completed to date support discrepant formation scenarios. Millimeter continuum observations for more of these systems are required to pin down the mechanism capable of generating these massive companions at wide

separations.

Chapter 6

HST Scattered Light Imaging and Modeling of the Edge-on Protoplanetary Disk ESO-Hα 569

Abstract

We present new HST ACS observations and detailed models of a recently discovered edge-on protoplanetary disk around ESO Hα 569 (a low-mass T Tauri star in the Cha I star forming region). Data was obtained as part of an HST campaign to image new edge-on disks around young stars in nearby star forming regions by following up candidates identified using Spitzer and WISE data. Using radiative transfer models, we probe the distribution of the grains and overall shape of the disk (inclination,

scale height, dust mass, maximum particle size, flaring exponent and surface/volume density exponent) by model fitting to multiwavelength (F606W and F814W) observations from the Hubble Space Telescope (HST). The spectral energy distribution can place constraints on the mass and distribution of grain sizes within a disk, while the scattered light images place constraints on the geometry of the disk. We developed a new tool set for finding optimal fits of MCFOST radiative transfer models using the MCMC code `emcee` to efficiently explore the high dimensional parameter space. We are able to self-consistently and simultaneously fit a wide variety of observables in order to place constraints on the physical properties of a given disk, while also rigorously assessing the uncertainties in those derived properties. We confirm that ESO Hα 569 is an optically thick nearly edge-on protoplanetary disk. We find that the shape of the disk is well described by a flared disk model with an exponentially tapered outer edge, consistent with models previously advocated on theoretical grounds and supported by millimeter interferometry. The scattered light images and spectral energy distribution are best fit by an unusually high total disk mass (gas+dust assuming a ratio of 100:1) with a disk to star mass ratio of 0.16. The large disk mass, even when coupled with a relatively steep surface density power law distribution, places the disk on the verge of instability in the inner few au.

6.1 Introduction

We seek to understand the initial conditions for planet formation and the physical processes that contribute to the assembly of planets by measuring the properties of young protoplanetary disks. The unique geometry of edge-on circumstellar disks provides a valuable opportunity to study detailed disk structure, as the bright central star is occulted from view and thus does not pose a contrast problem. The width of the disk's darklane (the vertical extent of the $\tau = 1$ surface), outer radius, and degree of flaring can be directly measured, and the scale height of the disk can be related to the local disk temperature (Watson et al., 2007). See Stapelfeldt (2004) for a review of the observational advantages of targeting edge-on disks. Previous studies of edge-on disks have measured disk inclinations and dust masses from a combination of scattered light images and millimeter continuum maps (Wolf et al., 2003; Sauter et al., 2009). Additionally, the change in the dust lane thickness with wavelength allows dust grain properties to be derived (Cotera et al., 2001; Wood et al., 2008; Duchêne et al., 2010; McCabe et al., 2011). However, the sample of edge-on disks with high resolution observations remains relatively small.

ESO Hα 569, a young M2.5 star embedded in the Chameleon star forming region (SFR), was imaged as part of an HST observation program designed to double the sample of edge-on protoplanetary disks for which we have high resolution images. The sample for the survey was chosen from WISE and Spitzer surveys of nearby star forming regions (SFRs) which allow identification of new candidate edge-on disks

from their characteristic double peaked spectral shape. HST program 12514 in Cycle 19 obtained high resolution optical imaging of the top 21 candidates, leading to the imaging of many disks including the data we present here (Stapelfeldt et al., 2014).

Several of the targets in this sample of edge-on protoplanetary disks, including ESO Hα 569, are known members of the Chameleon (Cha) SFR. Distances to Cha, one of the nearest SFRs, have been determined in a variety of ways including zero-age main sequence fitting and Hipparcos parallaxes of members. Whittet et al. (1997) provide a review of the results and combine measurements to arrive at a distance of 160 ± 15 pc. Bertout et al. (1999) confirm this distance after cross-correlating the Herbig & Bell and Hipparcos Catalogues. See Belloche et al. (2011); Appendix B1 for a more detailed review of Cha I distance measurements. Age estimates for Chamaeleon range from 1 - 2 Myrs (Baraffe et al., 1998; Chabrier et al., 2000). The Cha I SFR is characterized by a relatively high extinction with an observed maximum of $A_V \sim 10$ (Cambresy et al., 1997). Such a high extinction would suppress the blue side of the spectral energy distribution of a young stellar system. The initial mass function for Cha I has a maximum mass of $0.1 - 0.15\,M_\odot$ (Luhman, 2007), while the total mass of Cha I is $\sim 1000\ M_\odot$ (Boulanger et al., 1998).

The remainder of this introduction summarizes prior observations of ESO Hα 569 and summarizes the context and challenges with radiative transfer modeling of complex disk structures. In section 6.2 we present high resolution HST scattered light observations of the ESO Hα 569 protoplanetary disk and a spectral energy distribu-

tion (SED) compiled from the literature. In section 6.3 we present radiative transfer modeling efforts to fit these observations to a variety of disk properties. Both a grid and Monte Carlo Markov Chain (MCMC) approach were used to explore parameter space, and results are given in Sections 6.3.3 and 6.3.5. Section 6.4 discusses these results including the stability of the system and places ESO Hα 569 in context with previous disk observations. Lastly, Section 6.5 provides a Summary and Conclusions.

6.1.1 Prior Studies of ESO Hα 569

ESO Hα 569 (2MASS J11111083-7641574) was first identified as a target of interest in the Comerón et al. (2004) European Southern Observatory survey of young stars with strong Hα emission in Cha I SFR. Comerón et al. (2004) classified the central star as K7 using ground-based spectroscopy. The authors noted that this object is severely under-luminous for a K7 star (by $\sim$ 2 orders of magnitude), which made it a prime candidate for our edge-on disks survey. The Luhman (2007) survey of the stellar population in Chamaeleon obtained an R$\approx$5000 spectrum from 0.6-0.9 μm, which gave a spectral type of M2.5, an effective temperature of 3488 K, and an apparent bolometric luminosity of $L_{bol} = 0.0030\ L_{\odot}$. More recently, broad-band spectroscopy with VLT/X-Shooter provides a spectral type of M1 $\pm$ 2 subtypes (Manara et al., 2017, their table 3), and confirms that the target appears underluminous. Because ESO Hα 569 is heavily extincted by the disk, the apparent luminosity is an unreliable estimator for the true bolometric luminosity of the central star. For stars of the

same spectral type in the Luhman (2007) survey, the average bolometric luminosity is $0.34 \pm 0.08 L_{\odot}$. We adopt this luminosity and the $\sim$ 3500 K effective temperature. Using the theoretical evolutionary models of Baraffe et al. (1998) for low mass stars with solar metallicity gives a mass for the central star of $0.35 M_{\odot}$. The associated stellar radius is $1.13 R_{\odot}$.

Prior attempts have been made to infer the disk properties based on the spectral energy distribution. Luhman (2007) noted that the X-ray nondetection of this star indicates an extinction of $A_K \geq 60$, consistent with obscuration by an edge-on disk, assuming its X-ray luminosity is that of a typical T Tauri star. Robberto et al. (2012) combine published 2MASS and Spitzer photometry, with unresolved HST fluxes to fit properties of the disk and central star using the online library of 20,000 models of young circumstellar systems compiled by Robitaille et al. (2006). These models include the central star, a diffuse envelope and an accreting disk (Whitney et al., 2003a,b, 2004). The authors find the disk is best fit by an inclination of $\sim$ 87.1 degrees, $L_{bol} = 0.8 \pm 0.4 L_{\odot}$, $M_{star} = 0.33 \pm 0.03 M_{\odot}$, $R_{\rm star} = 2.5 \pm 0.6 R_{\odot}$, and give an upper limit for the sub-mm disk mass of $0.005 M_{\odot}$. Rodgers-Lee et al. (2014) included Herschel data and found a best fit inclination of 81.4 degrees. More recently, Pascucci et al. (2016) provide 1.3 millimeter continuum data which corresponds to a disk mass estimate of $0.0046\, M_{\odot}$, where we've assumed an opacity of $\kappa = 2.3 cm^2/g$, a gas to dust ratio of 100, and a disk temperature of 20 K.

6.1.2 Radiative Transfer Modeling and Model Fitting of Circumstellar Disks

Circumstellar disks are complex objects: mixtures of gas and dust, containing solid bodies from the smallest planestimals to giant Jovian planets, shaped by many dynamical forces across evolutionary states from the youngest protoplanetary disks through transitional regimes to second-generation debris disks. We can now probe this complexity with powerful observational capabilities across the entire electromagnetic spectrum, with especially detailed views provided in the visible by the Hubble Space Telescope, in the infrared by 8-10 m telescopes with adaptive optics and soon by JWST, and in the millimeter and submillimeter by ALMA and other interferometers. In some cases a particular physical property of interest can be directly measured from a given observation, but more typically we may need to fit a numerical model to the data in order to derive constraints on the underlying physics. This is particularly necessary for observations of disks at wavelengths where they are optically thick, which is the case for observations of protoplanetary disks at visual and near-IR wavelengths.

The general outline of such inference is well known: Start from a model of the system's properties and physics with some number of free parameters. Construct synthetic observables using that model, for instance through Monte Carlo radiative transfer calculations. Then compare the synthetic observables to data in order to

constrain the free parameters and draw conclusions about their most likely values and the ranges of uncertainty. This process sounds simple enough in theory, but is often a practical challenge due to several confounding factors, among them the complexity of the underlying physics (which inevitably requires simplifications in the models), the nonetheless high dimensionality of the model parameter space, and the need to confront heterogenous and multi-wavelength observations in order to resolve model degeneracies.

In this work we use the MCFOST radiative transfer code (Pinte et al., 2006), one of a broad class of class of Monte Carlo Radiative Transfer (MCRT) programs designed to study circumstellar disks (for a review of radiative transfer codes see Steinacker et al., 2013). In short, such a code begins with a numerical model of the physical properties within the disk, such as the density of dust in each grid cell, and the mineralogical composition and size distribution of dust particles. It then computes the temperature and scattering source function everywhere in the disk via a Monte Carlo method: photon packets are propagated stochastically through the model volume following the equations of radiative transfer, and information on their properties is retained along their path. The radiation field, and quantities derived from it (for instance temperature, radiation pressure, etc) are obtained by averaging this Monte Carlo information. Observable quantities (SEDs and images) are then obtained via a ray-tracing method, which calculates the output intensities by formally integrating the source function estimated by the Monte Carlo calculations.

This approach naturally allows simulation of disk images which are dominated by scattered starlight, thermal emission from the dust, or a combination thereof.

Comparison of the simulated images and SEDs against observations then allows inference about which ranges of model parameters are compatible. There are a couple different approaches to performing such comparisons. One option is to compute a grid of models spanning the parameter space of interest (e.g. Robitaille et al., 2006; Woitke et al., 2010; Pinte et al., 2008). Bayesian techniques allow derivation of uncertainty ranges around the best fit grid point (e.g. Chiang et al., 2012). However, even with hundreds of thousands of models computed, given the high dimensionality of the parameter spaces, each parameter must often be quite coarsely sampled at just a few discrete values, which can limit the results achieved. The grid technique is also computationally inefficient because it blindly allocates equal effort to both the best- and worst-fitting portions of parameter space. As is well known the Monte Carlo Markov Chain (MCMC) paradigm improves on this; the MCMC algorithm allows efficient exploration of parameter space and yields detailed information on parameter posterior probability distributions and correlations.

However, most disk model-fitting efforts to date have concentrated on fitting either SEDs alone (e.g. Huélamo et al., 2010; Ribas et al., 2016) or images or interferometric visibilities alone (e.g. Millar-Blanchaer et al., 2015; Ricci et al., 2015; Pohl et al., 2017). This is broadly the case independent of the choice of grid fitting versus MCMC fitting. But fits to SEDs alone are notoriously degenerate (Chiang et al., 2001; Woitke,

2015), and spatially resolved image data or interferometric visibilities are required in order to place robust constraints on many properties of interest. Only a handful of disk studies have successfully and rigorously fit models to heterogenous observables including SEDs and images or interferometric visibilities, but when this has been achieved it has often yielded particularly powerful constraints and detailed insights into disk structures (e.g. Pinte et al., 2008; Lebreton et al., 2012; Duchêne et al., 2010; Carmona et al., 2014; Milli et al., 2015; Cleeves et al., 2016).

Such works have most often used the grid fitting approach rather than MCMC, perhaps due to the increased technical complexity of integrating the MCMC framework with heterogenous observables. A detail – but an important one in this context – is that the MCMC approach necessarily assesses a single goodness-of-fit metric which must combine both SED and image data together, such as a sum of χ^2 values from the SED and image (or more generally from any combination of distinct observables). In the case where the best-fitting χ^2 for one observable is systematically much higher than for the other observable(s), the model fitting will be driven by that first observable, and will likely not deliver an adequate simultaneous fit to the others. Models must necessarily simplify, and imperfect models lead to correlated systematic residuals that increase the minimum χ^2. Consider for instance attempting to fit a simple axisymmetric model to an eccentric disk. This problem is generally worse for images than for SEDs, because the one-dimensional nature of SEDs collapses much of the parameter space. In other words, the well-known degeneracies of SEDs can hide

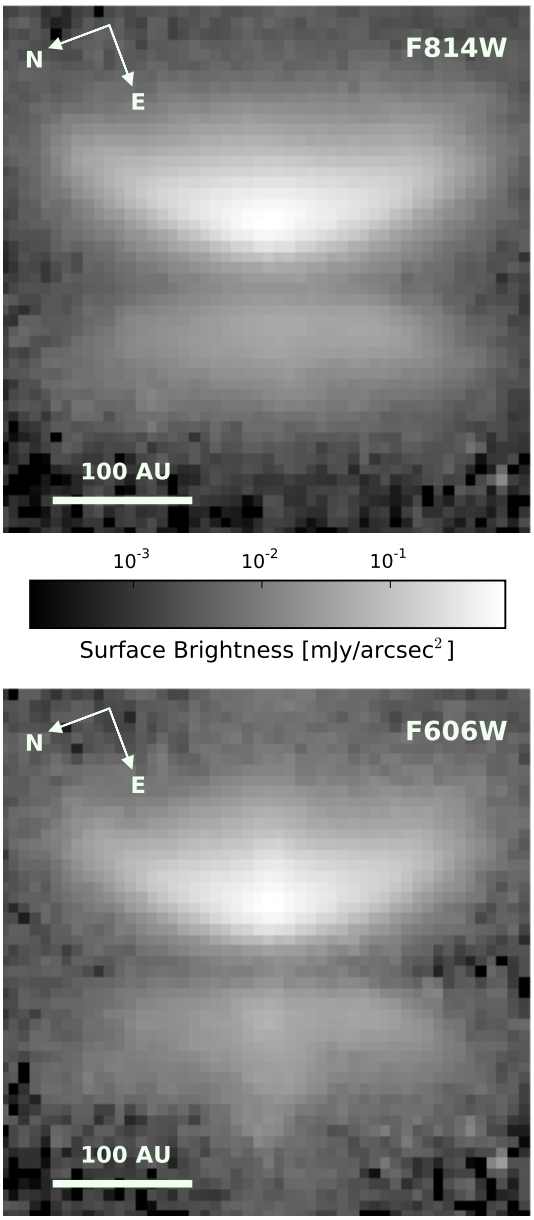

Figure 6.1 HST images of the protoplanetary disk ESO-Hα569. Top: F606W. Bottom: F814W. Both images show the dark dust lane and asymmetries between the top and bottom of the disk, while only F606W establishes the presence of an outflow jet. The 100 au scale bar corresponds to an angular scale of 0.625″.

disk offsets, eccentricities, spiral arms, and other asymmetries that are immediately apparent in sufficiently high resolution images. As a result, it becomes difficult to develop a good metric that combines both images and SEDs in a well-balanced manner for the purposes of a simultaneous MCMC fit.

To address this difficulty in fitting disk observations, we have developed a new method that explicitly takes into account the covariant and correlated residuals in the image fitting. Czekala et al. (2015) introduced this approach in the context of 1D spectral fitting. We extend that approach to work on heterogenous disk datasets including 2 dimensional images, and use that to implement an MCMC fitting process that balances both the image and SED data for ESO Hα 569. This is described in detail in Section 3 below.

6.2 Observations

Here we present our new HST scattered light imaging of ESO Hα 569 obtained as part of our edge-on disks survey. We also provide a spectral energy distribution compiled from the literature.

6.2.1 HST Scattered Light Images

Table 6.1: Spectral energy distribution photometry and references.

$\lambda(\mu m)$	Flux (mJy)	Source	Instrument	Bandwidth (μm)	Angular Resolution	Date
0.551	0.030 ± 0.004	Robberto et al. 2012	HST WFPC2	0.14	0.0996″	2009-04-27
0.606	0.058 ± 0.001	This work	HST ACS	0.27	0.05″	2012-03-09
0.814	0.21 ± 0.01	This work	HST ACS	0.31	0.05″	2012-03-09
1.235	0.66 ± 0.05	Skrutskie et al. 2006	2MASS	0.16	∼5″	2000-01-25
1.662	0.97 ± 0.08	Skrutskie et al. 2006	2MASS	0.25	∼5″	2000-01-25
2.15	0.98 ± 0.09	Skrutskie et al. 2006	2MASS	0.26	∼5″	2000-01-25
3.6	0.58 ± 0.03	Luhman et al. 2008	Spitzer IRAC	0.75	∼2″	2004-07-04
4.5	0.57 ± 0.05	Luhman et al. 2008	Spitzer IRAC	1.02	∼2″	2004-07-04
5.8	0.58 ± 0.05	Luhman et al. 2008	Spitzer IRAC	1.43	∼2″	2004-07-04
8.0	0.67 ± 0.05	Luhman et al. 2008	Spitzer IRAC	2.91	∼2″	2004-07-04
3.4	0.63 ± 0.02	Cutri et al. 2012	WISE	0.66	6.1″	2010-02-13,20
4.6	0.71 ± 0.02	Cutri et al. 2012	WISE	1.04	6.4″	2010-02-13,20
12	0.65 ± 0.07	Cutri et al. 2012	WISE	5.51	6.5″	2010-02-13,20
22	7.5 ± 0.89	Cutri et al. 2012	WISE	4.10	12.0″	2010-02-13,20
24	8.36 ± 0.77	Luhman et al. 2008	Spitzer MIPS	5.3	6″	2004-04-08
70	107 ± 10.8	Luhman et al. 2008	Spitzer MIPS	19	18″	2004-04-08
70	200 ± 100	Winston et al. 2012	Herschel PACS	25	5.8″	2011-06-23
160*	200 ± 200	Winston et al. 2012	Herschel PACS	85	12.0″	2011-06-23
250*	100 ± 100	Winston et al. 2012	Herschel SPIRE	25	18″	2011-06-23

Table 6.1: Spectral energy distribution photometry and references.

$\lambda(\mu m)$	Flux (mJy)	Source	Instrument	Bandwidth (μm)	Angular Resolution	Date
350*	50 ± 50	Winston et al. 2012	Herschel SPIRE	25	25″	2011-06-23
500*	50 ± 50	Winston et al. 2012	Herschel SPIRE	25	37″	2011-06-23
870	72 ± 14	Belloche et al. 2011	APEX/LABOCA	150	19.2″	May 2008
2830	3.2 ± 0.1	Dunham et al. 2016	ALMA	55	∼2″	2013-11-29 to 2014-03-08

Photometry at wavelengths marked with an * represent only upper limits and are not included in the spectral energy distribution modeling.

Scattered light images of the ESO Hα 569 disk were obtained using HST ACS/WFC in both the F814W and F606W broad band filters on March 9th, 2012 as part of program GO 12514. The total exposure times were 1440 s for F606W and 960 s for F814, with each filter's exposure split as two integrations for cosmic ray rejection. The reduced and calibrated data produced by the HST pipeline were retrieved from the Mikulski Archive for Space Telescopes (MAST).

Figure 6.1 provides the reduced images, rotated to place the disk major axis horizontal. The bipolar appearance unequivocally demonstrates the edge-on nature of ESO Hα 569. The western side is much brighter than the eastern (by $\sim 20\times$ comparing their peak surface brightnesses) and, along with the curvature of the nebula, indicates this side is tilted slightly toward us. There is no sign of starlight directly peeking through as an unresolved point source. The position angle of the disk's minor axis was evaluated to be 65 $\pm$ 1 degrees. This was computed as the position angle for which mirroring the image across the minor axis minimized the flux difference between the left and right sides. The disk is close to left/right symmetric, though the southern side (right side as shown in Fig. 1) is very slightly brighter.

The disk is very red (much brighter in F814W than F606W). We measure the disk's flux density in both filters using a 50 pixel aperture, which corresponds to a spatial scale of 2 x 2" and was chosen to encompass all disk flux with surface brightness $\geq 3\sigma$ above the background noise. We measure a flux density of 0.058 $\pm$ 0.001 mJy in F606W and 0.21 $\pm$ 0.01 mJy in F814W which gives a color [F814W]-[F606W] =

1.4 AB magnitudes.

The disk has an apparent outer radius of 0.80 ± 0.05″ which corresponds to 125 ± 8 au at a distance of 160 pc. Here, the outer radius is inferred as the offset at which the flux declines to less than 10 % the peak value for the widest part of the disk.

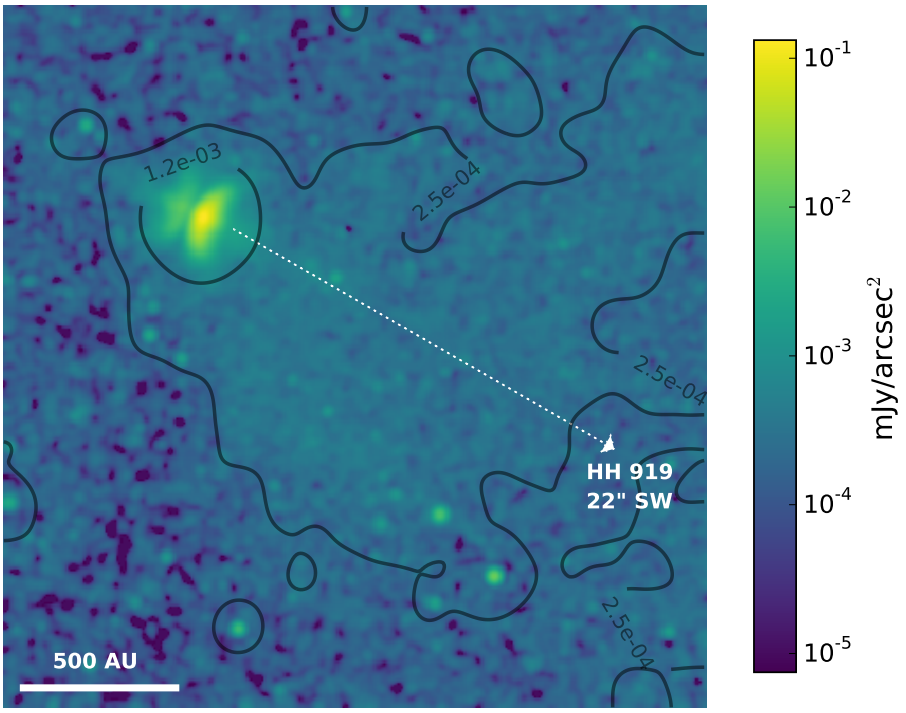

Figure 6.2 A wider F606W filter image displaying the diffuse nebula extending outward from the disk. The location of the Hα filament HH919 is shown by the arrow. The jet lines up well with the reported position of HH 919, consistent with ESO Hα 569 being the origin of this outflow. The 500 au scale bar corresponds to an angular scale of 3.125″.

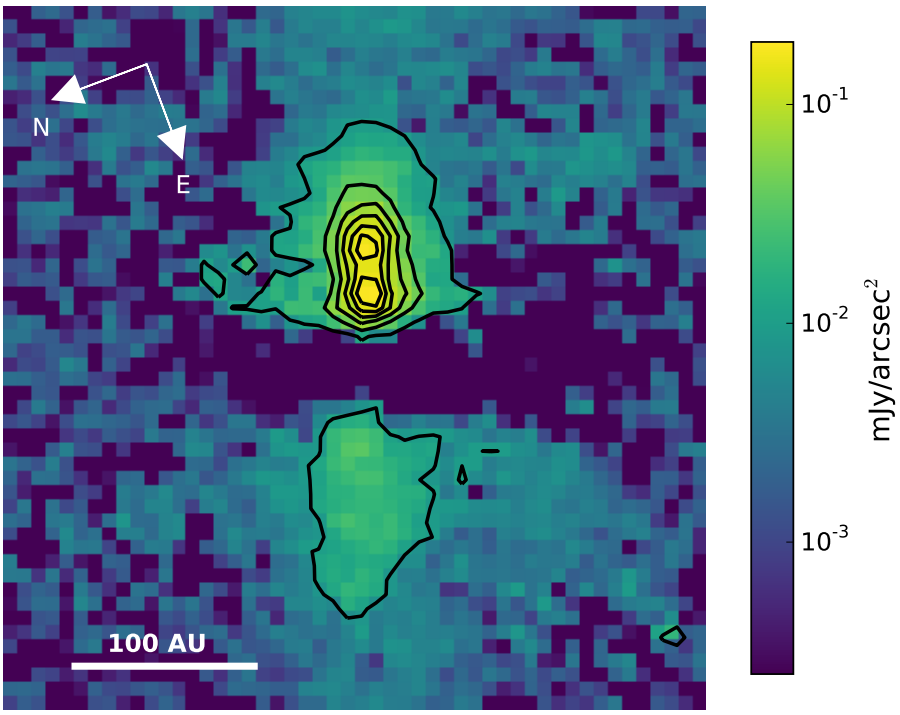

Figure 6.3 An image of the jet created by subtracting the F814W image from the F606W image. Contours are drawn from 0.01 to 0.19 mJy/arcsec^2 in intervals of 0.03 mJy/arcsec^2. The 100 au scale bar corresponds to an angular scale of 0.625″.

6.2.2 Jet Outflow

The strong Hα emission in the spectra of this young object indicates ongoing accretion onto the central star, which is often associated with launching of outflow jets. Bally et al. (2006) suggest ESO Hα 569 as the possible source for the Herbig Haro object 919. HH 919 is an arcminute long filament with a PA of $\sim$ 60 - 75 degrees and is located 22$''$ (0.05 pc) southwest of ESO Hα 569. A jet is visible in the F606W scattered light image extending vertically from the disk and is $\sim$ 0.25$''$ wide. A line connecting ESO Hα 569 with HH 919 would have a PA of $\sim 63^{\circ}$, giving an orientation consistent with the ESO Hα 569 jet serving as the culprit for the HH 919 filament.

Figure 6.2 presents a wider field of view showing the interaction of this disk with the surrounding ISM. Diffuse nebulosity is visible extending outward from the disk. An image of the jet was created by subtracting the F814W image (scaled by a factor of 2.5) from the F606W image (Figure 6.3). The flux from the jet is difficult to decouple from the disk flux, but we estimate the jet accounts for roughly 50 % of the local surface brightness from the disk. This value is taken from an average of the flux over 9 pixels with the jet superimposed on the disk and compared to the flux in 9 neighboring pixels with no jet signature. The peak surface brightness of the jet is $\sim$ 0.19 mJy/arcsec^2. Our ability to measure color variations in the shape of the disk and width of the dark lane between the F606W and F814W bands is hindered by the presence of this bright jet.

6.2.3 Spectral Energy Distribution

A spectral energy distribution (SED) for the disk was compiled from the literature, including data from HST, 2MASS, Spitzer, WISE, Herschel, ALMA, and the LABOCA instrument on the APEX telescope. See Figure 6.4. Table 6.1 provides the SED values with photometric errors and references for each value. The SED shows the characteristic double-peaked shape of edge-on disks with contributions from both the scattered light from the central star peaking at about 1.5 μm and the thermal emission from the surrounding optically thick disk peaking at roughly 70 μm. Data at similar wavelengths from different epochs show variability at the $10-20\%$ level, consistent with variability seen in other young disks (Espaillat et al., 2011; Flaherty et al., 2012; Muzerolle et al., 2009).

ESO Hα 569 was imaged with Herschel as part of the Gould Belt survey in the PACS 70 and 160 μm bands and the SPIRE in the 250, 350 and 500 μm bands (Winston et al., 2012). The source is barely detected in the PACS bands, hence the large uncertainties reported by Winston et al. (2012). There seems to be a very marginally-detected point source in the SPIRE bands (100 ± 100 mJy at 250 μm and 50 ± 50 mJy at 350 and 500 μm), but given the coarse angular resolution, it's hard to exclude contamination from dust emission from the surrounding cloud itself. Given the low significance of these detections, the Herschel fluxes are not included in our SED fits.

An ALMA Band 3 continuum (2.8 mm, 106 GHz) measurement was obtained by

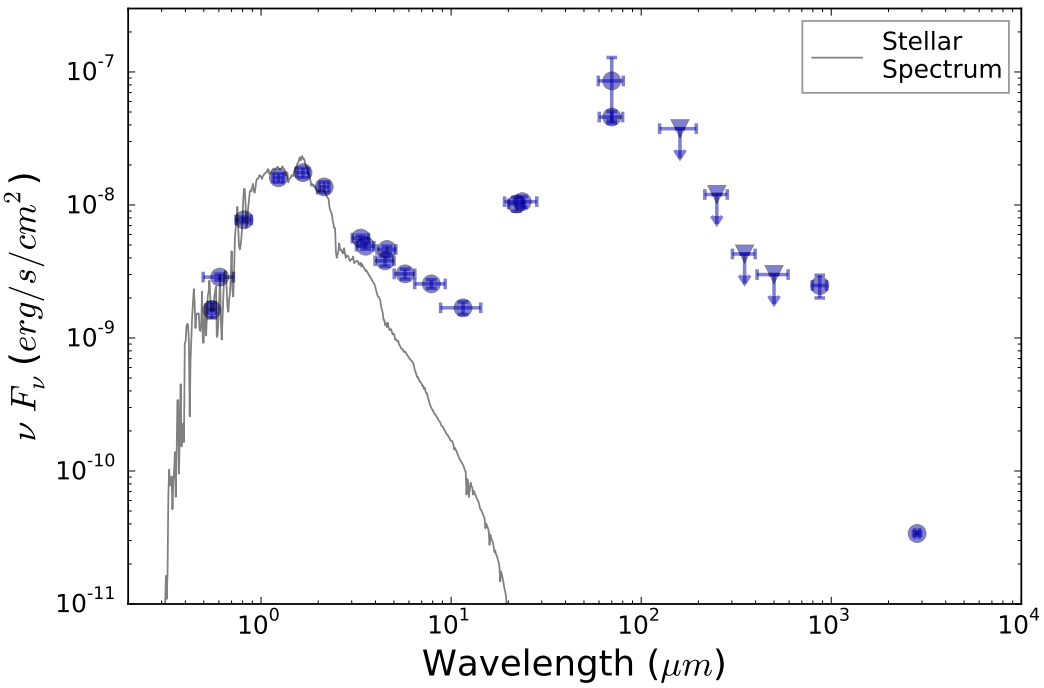

Figure 6.4 Spectral energy distribution for ESO-Hα 569 with upper limits indicated by triangles. The SED exhibits the double peaked structure typical of an optically thick, edge-on disk. The values were compiled from the literature with more information given in Table 1. The stellar spectrum for an M2.5 star with T_{eff} = 3500 K is overplotted.

Dunham et al. (2016) with ALMA in a compact configuration that achieved a $\sim$2" beam, and does not resolve the disk. Because the disk isn't resolved, the ALMA continuum flux could be contaminated with flux from a remnant envelope. However, there cannot be too much non-disk material present, or it would be too opaque to see the central disk in scattered light in the visible as we do. This measurement was published after our initial rounds of disk SED fitting as described below, but this datapoint has been included in our more recent SED model fitting.

In addition to the continuum measurement at 0.55 μm included in Table 1, Robberto et al. (2012) provide fluxes for ESO Hα 569 in HST WFPC2's F631N, F656N and F673N narrow band filters associated with [OI], Hα, and [SII] emission respectively. The disk is not resolved and the measured fluxes are near the detection limits: 0.21 $\pm$ 0.15 (F631N), 2.4 $\pm$ 0.7 (F656N), and 0.35 $\pm$ 0.12 (F673N) $\times 10^{-16}$ erg s^{-1} cm^{-2} Å^{-1}. These emission lines are all consistent with the spectrum of Luhman (2007), which shows strong Hα emission and [SII] emission. Given the large uncertainties, and that our model is not set up to simulate line emission, we chose to not include these in our SED fits.

6.3 Model Fitting

The scattered light images and full SEDs together provide a comprehensive dataset for ESO Hα 569 against which properties of the central star and surrounding disk

Table 6.2. ESO Hα 569 Modeled Disk Parameters

Parameter	Grid Values	MCMC Values
Distance (pc)	160 (Fixed)	160 (Fixed)
Outer Radius (au)	125 (Fixed)	125 (Fixed)
Min Particle Size (μm)	0.03 (Fixed)	0.03 (Fixed)
Inclination (degrees)	60 to 90	65 - 90
Scale Height (H in au at R=100 au)	10, 15, 20, 25	5 - 25
Dust Mass (M in $M_{\odot}$)	10^{-4}, 3×10^{-4}, 10^{-3}	10^{-5} - 10^{-3}
Surface Density (α)	-2.0, -1.5, -1.0, -0.5, 0.0	-2.0 - 0
Flaring Exponent (β)	1.1, 1.2, 1.3, 1.4, 1.5	1.0 - 1.5
Max Grain size[a](μm)	100, 1000, 3000	100 - 3000
Weight[b]	—	0.3 - 0.7
Grain Porosity	0.0, 0.25, 0.5	—
Structure	Disk, Tapered Edge Disk	—

[a]Grain size was kept at a constant value of 100 μm for the covariance based MCMC run.

[b]During the χ^2 based MCMC run a weighting term was used to describe the relative contribution of the image and SED fits to the log likelihood value of each model.

can be tested. The disk geometry can be directly measured from the images and the distribution of the dust grains within the disk is traced by the SED and disk morphology. To characterize this system, we construct disk models and explore parameter space with direct comparisons to the observations.

The parameter space described below was explored in two stages using two different techniques. First, we computed a coarse model grid with a wide range of allowed model parameter values to get a handle on reasonable regions of parameter space. Section 6.3.2 describes the initial exploration of parameter space via a grid search, with results in Section 6.3.3. This work was used to inform a more robust Markov Chain Monte Carlo exploration for finer sampling of allowed parameter values, with methods described in Section 6.3.4 and results given in Section 6.3.5.

6.3.1 Radiative Transfer Modeling with MCFOST

For this work, we use the MCFOST radiative transfer code (Pinte et al., 2006, 2009) to construct SEDs and 0.8 μm scattered light images for each of our models. We chose not to model the 0.6 μm scattered light images because the strong jet signature required masking $\geq 50\%$ of the integrated disk flux.

Our model assumes an axisymmetric disk with a surface density, Σ, described by a power law distribution in radius given by $\Sigma = \Sigma_0(R/R_0)^{\alpha}$ where α is termed the surface density exponent and R_0 is the reference radius of 100 au. In this "sharp-edged" model the disk is abruptly truncated at an outer radius R_{out}. In order to

achieve a good fit to the diffuse emission above the disk and the disk mass and inclination simultaneously, we also tested a "tapered-edged" disk model in which the density Σ falls off exponentially with some critical radius R_c of material outside of the disk:[1]

$$\Sigma = \Sigma_c \left(\frac{R}{R_c}\right)^{\alpha} \exp\left[\left(-\frac{R}{R_c}\right)^{2+\alpha}\right] \tag{6.1}$$

For this work we set $R_c = R_{out}$. This exponential taper is predicted by physical models of viscous accretion disks (Hartmann et al., 1998), but observations were not sensitive enough to detect this outer gradual fall-off until Hughes et al. (2008) used this form to model both gas and dust continuum observations in the millimeter. It is expected that the small dust grains seen in scattered light should be well coupled with the gas for young disks, suggesting the use of this surface density distribution is justified here. (See also recent work by Pohl et al., 2017). The scale height is also defined as a power law in radius by $H(R) = H_0(R/R_0)^{\beta}$ where β is the flaring exponent describing the curvature of the disk and again $R_0 = 100$ au.

Several model parameters were held fixed to minimize the degrees of freedom and to save computation time. Values for these parameters were either measured directly from the HST images or taken from the literature. The disk is within the SFR Chamaeleon I (Cha I), therefore we assume a distance to the disk of 160 pc (Whittet et al., 1997). From the angular size of the disk measured above and the distance, we calculate an outer radius of 125 au. The inner radius was defined by a

[1]Note that some authors give this equation using the notation $\gamma = -\alpha$.

conservative estimate of the sublimation radius $R_{\rm sub} = R_{\rm star}(T_{\rm star}/T_{\rm sub})^{2.1} \sim 0.1\,AU$ where $T_{\rm sub} = 1600\,K$ (Robitaille et al., 2006).

We left as free parameters the inclination (with 90° as edge-on), scale height, dust mass, maximum dust particle size, dust porosity, disk vertical flaring exponent (β) and surface density exponent (α), and disk edge type (sharp or tapered). For the maximum particle size, the grain population is described by a single species of amorphous olivine grains (Dorschner et al., 1995) with a particle size distribution following a -3.5 power law extending from 0.03 μm up to the free parameter a_{max}. This combination of dust properties (with $a_{max} = 100\,\mu m$) results in a mean scattering phase function asymmetry factor of $g = 0.54$. Dust porosity is modeled simply as a fraction between 0 and 1 of vacuum that is mixed with the silicates following the Bruggeman effective mixing rule.

For comparison with the observed 0.8 μm scattered light images, each model image was convolved with a Tiny Tim simulated PSF (Krist, 1995). The 0.8 μm observations were masked to select only the pixels with flux values $\geq 3\sigma$ above the background noise level. A 2D map of the noise was generated by converting the observed image to electrons, and assigning $\sigma = \sqrt{N_{e-}}$ for the χ^2 values. The model images were aligned with the observations via a cross correlation and normalized to the total observed flux. The models were then compared to the data via an error-weighted pixel-by-pixel χ^2 calculation. For similar work see Duchêne et al. (2010) and McCabe et al. (2011). For the SEDs, when fitting each model point we allow

the foreground extinction to vary from $A_V = 0 - 10$ with $R_V = 3.1$, and choose the extinction value that minimizes the observed - model residuals.

While the robust treatment of radiative transfer provided by MCFOST is essential for modeling optically thick disks, it is computationally intensive. Generating a single model SED requires $\sim$ three minutes of desktop CPU time, with an additional $\sim$ minute to generate synthetic images at each desired wavelength. MCFOST allows the user to parallelize the computation, however, systematic explorations of parameter space can quickly become very time consuming.

6.3.2 Initial Exploration of Parameter space via grid search

Our initial modeling used a uniform grid sampling, with the explored parameter space shown in Table 6.2. For each set of disk model parameters, 15 disk inclinations were sampled uniformly in $\cos i$ between 60 and 90 degrees. This resulted in a grid of over 200,000 models. Comparison with data were performed using custom IDL software. A benefit of the grid search approach is that multiple goodness-of-fit metrics may be evaluated across all sampled points. χ^2 values were computed separately for the 0.8 μm image and SED for each model along with the combined total $\chi^2_{tot} = \chi^2_{0.8\,\mu m} + \chi^2_{SED}$. Bayesian probabilities are derived from the likelihood function wherein the χ^2 value for a given model with unique parameter values is related to a probability

$\exp(-\chi^2/2)$ and the sum of all probabilities is normalized to unity (e.g. Pinte et al., 2008).

The grid sampling is a simple way to explore parameter space initially, but its sampling of parameters proved to be inadequate for several reasons. First it is too sparse to provide clear insight into degeneracies between the various parameters. Secondly, the discrete sampling limits the precision with which best-fit values can be determined, and does not allow rigorous computation of uncertainties. These factors motivated the later development of our MCMC model-fitting toolkit described below. Nonetheless the results of the grid search helped clarify relevant portions of parameter space and informed our understanding of the disk.

6.3.3 Results and Conclusions from Grid Search

For the grid search approach, the best fit model for the disk was found using a tapered-edged disk with non-porous grains, an inclination of 75.5 degrees, and a scale height of 20 au at a reference radius of 100 au. The preferred maximum particle size is 3000 μm, the dust mass is 3 $\times$ 10^{-4} $M_{\odot}$, the flaring exponent β is 1.3 and the surface density exponent α is -0.5. The separate SED and image fits for the α and β exponents favor opposing extremes of parameter space, but the combined χ^2_{tot} likelihood distribution peaks in the middle at physically reasonable values.

Figure 6.5 illustrates the likelihood distributions for the inclination and scale height. The sparse sampling and disagreement between the model parameters pre-

ferred by the image and SED (most pronounced in the scale height) demonstrate the limitations of the grid fitting approach.

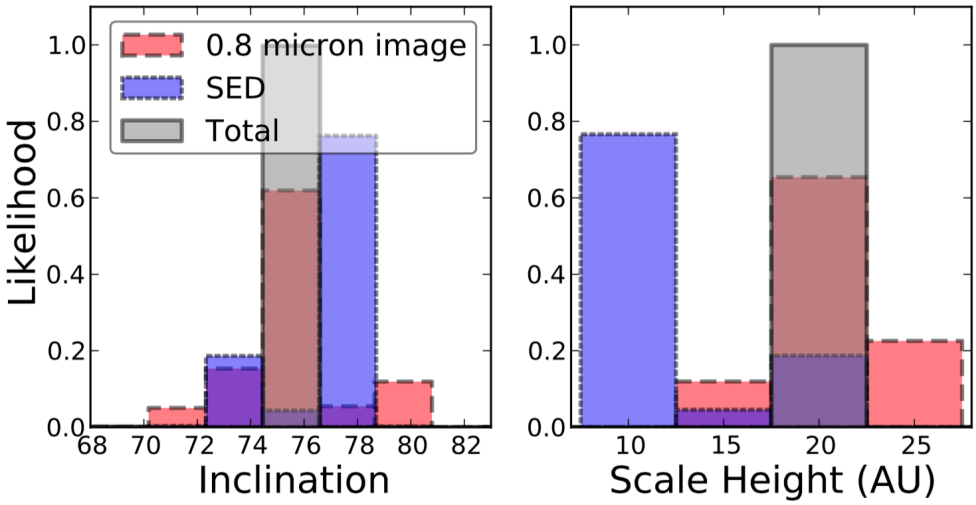

Figure 6.5 Likelihood distributions from the grid search for the disk inclination and scale height computed from the model χ^2 values for the 0.8 micron image (red), the SED (blue) and for the combined dataset (grey). The image and SED results favor different regions of parameter space. The sampling of the grid approach is sparse and does not provide an adequate estimate of the uncertainties.

6.3.3.1 Porosity

Porous grains were initially included in the modeling parameters to provide a better fit to the flux ratio between the top and bottom disk nebulae. Porous grains are generally more forward scattering, which would increase the flux ratio without needing to increase the line-of-sight inclination. However, the SED fitting strongly favored non-porous grains. A porosity of $\gtrsim 0.5$ produced a strong dip in the SED around the 10 - 20 μm silicate feature that was not observed for this target. The

overall SED+image fits also favor the non-porous grains, though not as strongly as the SEDs alone. The flux ratio issue was subsequently solved by invoking a tapered edge surface density model for the disk structure. For subsequent modeling, we chose to use only non-porous grains.

6.3.3.2 Disk Structure: Sharp vs. Tapered Outer Edge

When modeling the disk with a sharp outer edge, the SED and image fits preferred very different regions of parameter space. Specifically, it was difficult to simultaneously fit the flux ratio between the top and bottom nebulae of the disk, the diffuse emission above the plane of the disk, and the shape of the disk. Because the disk is not precisely edge-on, the scattering angles differ between the upper and lower disk nebulae. Therefore, changes in the scattering phase function of the grains will change the peak-to-peak flux ratio. Any parameter that would increase the flux ratio and emission above the disk (for example increasing the inclination or porosity of the grains) caused too much forward scattering and allowed too much of the light from the central star to appear in the peak. Similarly, we found that the diffuse emission above the disk could not be described well by a low mass spherical envelope.

The tapered-edged disk did much better in accounting for both the emission above the disk and matching the flux ratio between the top and bottom sides of the disk. This is clearly demonstrated in Figure 6.6 which compares the observations to the best fit tapered-edged disk model and corresponding sharp-edged model. The right

panel shows the surface brightness profiles through several vertical cuts across the disk for both the sharp- and tapered-edged models.

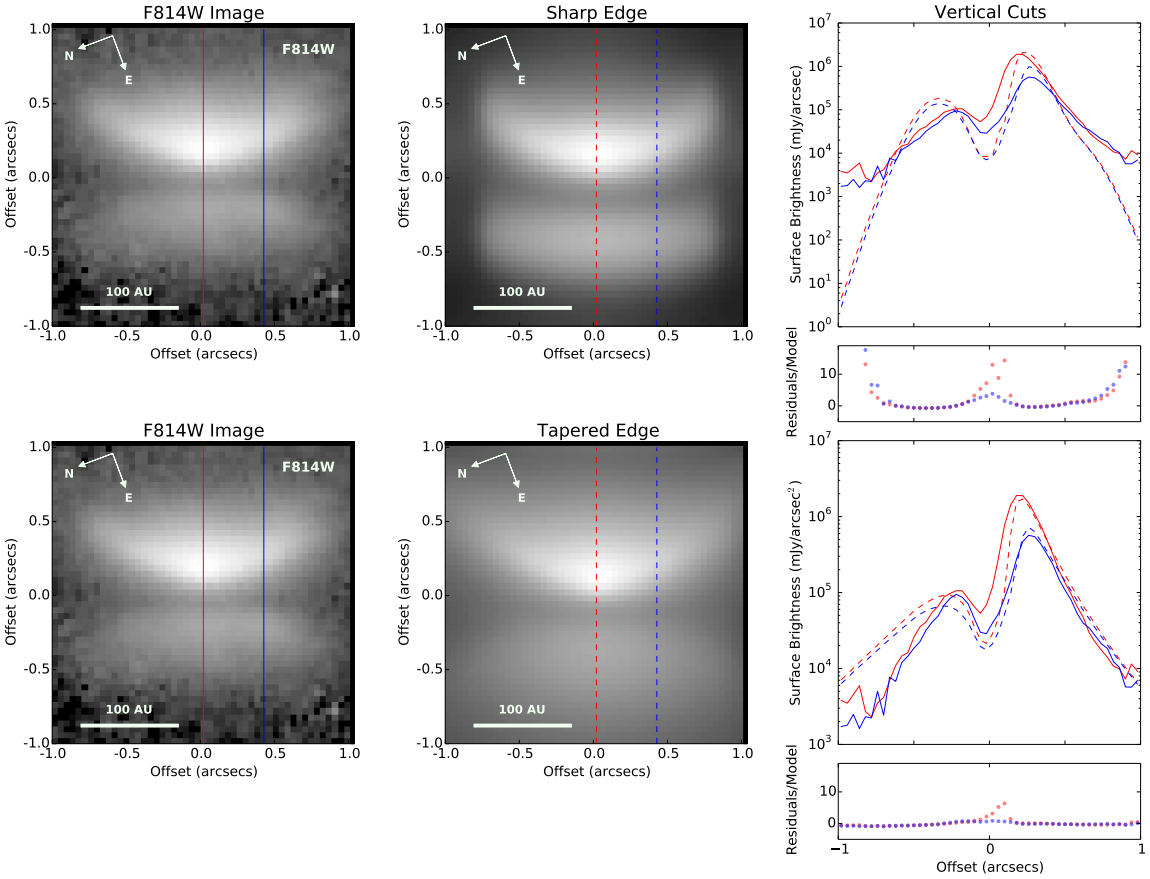

Figure 6.6 We show surface brightness profiles for two vertical image cuts through the data (left) and through the sharp-edged (Top middle) and tapered-edged (Bottom middle) disk models. The residuals for the two models are plotted on the same scale (smaller panels at right). The tapered edge model does a much better job of fitting the shape of the disk, especially the depth of the disk midplane, and the diffuse outer regions.

6.3.4 Model Optimization via MCMC

To more efficiently sample parameter space, and to gain a better understanding of our uncertainties, we turned to a Monte Carlo Markov Chain approach. We used the Python package `emcee` (Foreman-Mackey et al., 2013) which uses an Affine Invariant Markov Chain Monte Carlo (MCMC) Ensemble sampler algorithm by Goodman & Weare (2010). Specifically, we used the parallel-tempered MCMC sampler designed to improve convergence in degenerate parameter spaces. The MCMC samples the posterior distribution given by:

$$\mathrm{P}(\Theta|\mathrm{D}) \propto \mathrm{P}(\mathrm{D}|\Theta)\mathrm{P}(\Theta) \tag{6.2}$$

where D represents the observations, and Θ the free parameters in the model. Here $\mathrm{P}(\mathrm{D}|\Theta)$ is the likelihood of the data given the model and $\mathrm{P}(\Theta)$ is the prior distribution. We adopt uniform priors for each parameter over the allowable range.

In order to implement this code in conjunction with the MCFOST radiative transfer code, we developed a suite of software tools in Python to interact with the observations, generate models and calculate goodness-of-fit metrics to inform the MCMC iterations. The toolkit is general enough to be usable with any disk image, provided a PSF and uncertainty map are available. By combining the detailed modeling capabilities of MCFOST with the efficient parameter space sampling of the `emcee` package, we hope to self-consistently and simultaneously fit a wide variety of observables in

order to place constraints on the physical properties of a given disk, while also rigorously assessing the uncertainties in the derived properties. The code is publically available on github[2], and we encourage its use by the disk modeling community.

The `mcfost-python` package was designed to be modular, with different components to read in the observables, interact with the MCFOST parameter files, generate model SEDs and images, compare them to data, and setup and control the overall MCMC run. To validate the functions for comparing models to data, we performed benchmark cross-checks to compare the new Python fitting code to existing χ^2 routines in IDL and Yorick. While this code was originally designed to work with HST data and the MCFOST modeling package as described in this paper, it has also been expanded to work with data from different instruments, including polarimetry data, and can be used with other radiative transfer modeling codes.

6.3.4.1 χ^2 Based Log-Likelihood Estimation

The `mcfost-python` package allows the user to choose between two goodness-of-fit metrics. In this section, we discuss the χ^2 comparison. We provide a simple benchmark comparison of the χ^2 and covariance likelihood methods in the Appendix. At each step in the MCMC iteration, a model image and SED are created for the chosen parameter values and a χ^2 value is calculated using the same methodology as the grid sampling approach. The `emcee` code requires a log likelihood distribution

[2]https://github.com/swolff9/mcfost-python

which is computed from the χ^2 assuming a multi-dimensional Gaussian likelihood function:

$$\ln[P(D|\Theta)] = -0.5N \ln 2\pi + \sum_{i=1}^{N}(-\ln|\sigma_i|) - \frac{1}{2}\chi_i^2 \tag{6.3}$$

Here N is the number of data points, and σ is our uncertainty. The MCMC approach inherently requires a single goodness-of-fit metric and so we must combine the SED and image metrics into a single log likelihood function for use by `emcee`. The log likelihood distribution is computed separately for the images and SEDs, and a weighted average is used to determine the goodness of fit.

During initial tests using the χ^2-based log-likelihood goodness of fit metric, we chose to allow the relative weighting between the image and SED to vary. The best way to handle relative weighting between different types of observations for a single disk model was not well understood, and is a nuisance parameter that does not, itself, inform us about any inherent physical properties of the disk. By marginalizing over it in this way, we hoped to get a best fit model that was informed by both the SED and image data without a bias towards one or the other. We allowed the weighting to vary between 0.3 and 0.7 for a minimum of 30% weighting to either the image or SED fits. We found that the image likelihood values were down-weighted due to the systematically higher χ^2 values, and the MCMC chains worked to improve the images while largely ignoring the better SED fits. In our first round of MCMC calculations, we found that our image reduced χ^2 values tended to be more than an order of magnitude above the SED reduced χ^2 values (best $\chi^2_{SED} = 1.3$, $\chi^2_{0.8\mu m} = 66$), due to

the larger number of measurements in the images presumably with under-estimated uncertainties.

6.3.4.2 Covariance Based Log-Likelihood Estimation

The imbalance between the image and SED χ^2 values served as the impetus for the development of the covariance matrix likelihood estimation method, which ultimately provided much better relative weighting of the different observables. Given that each model image is convolved with an instrumental PSF, neighboring pixels must be covariant. Furthermore, we need to correct for the global limitations of the disk model to fit the dataset. Model systematics present as correlated uncertainties. For a more reasonable estimate of the errors in our HST images, we adapt the method for log likelihood estimation using a covariance matrix presented by Czekala et al. (2015) in the context of 1D spectral fitting. Here we must extend that approach to work in the context of 2D images. In this case, we convert Eq. 6.3, which describes the likelihood of our data given the model assuming a Gaussian likelihood distribution, into a matrix formalism in Equation 6.4.

$$\ln[\mathrm{P}(\mathrm{D}|\Theta)] = -\frac{1}{2}(R^T C^{-1} R + \ln[\det(C)] + N \ln[2\pi]) \tag{6.4}$$

where R represents the residuals of the observations subtracted by the model, C is the covariance matrix defined below, and N is the total number of pixels in the image

(*not* the number of pixels along a given dimension of the array).

Note that to apply this approach we must first "unwrap" each 2D image into a 1D array. In practice not all pixels in a square image may have sufficient SNR to justify fitting. Excluding such pixels from the unwrapping improves the overall computational efficiency, particularly for the matrix inversion calculation, at the cost of somewhat more complex bookkeeping between the 2D and 1D versions of the image.

The covariance matrix C (of size $N_{pix} \times N_{pix}$) incorporates both the noise in each individual pixel and global covariances between adjacent pixels (represented by K^G): $C_{i,j} = \delta_{i,j}\sigma^2_{i,j} + K^G_{i,j}$. An example source of global covariance is the FWHM of a telescope PSF. For a non-zero PSF FWHM, neighboring pixels cannot be treated as individual measurements of the disk surface brightness. Additionally, any global limitations of the model to fit the data can be implicitly included in the covariance structure. For example, when using a symmetric disk model any asymmetries in the observed image of the disk will necessarily lead to higher correllated residuals even for the best-fitting model parameters. These residuals will in general be spatially correlated on one or more scales from the angular resolution to the size of the observed asymmetry. Incorporating our knowledge of these residuals in the covariance matrix improves our ability to draw conclusions given such necessarily imperfect models. Likewise, the choice of incomplete or simplified parameterizations of the disk physics/structure in our model can be handled the same way. For instance, if there exists an additional un-modeled component such as a more vertically-extended disk

atmosphere or significant residual jet emission on the top/bottom on the disk, or if the functional form of the power law adopted for the disk surface density is an over-simplified description of the disk's true properties, such systematics would lead to correlated residuals in data-model comparisons. This covariance framework allows us to down-weight these contributions within the correlated residuals without masking them altogether.

The field of Gaussian processes has developed several useful analytic models for convolution kernels that can be used to parameterize covariant structure. For instance Czekala et al. (2015) adopt the Matérn kernel truncated by a Hann window function. This kernel has several free parameters, which can be solved for as nuisance parameters as part of the MCMC fit. Of course, this increases the dimensionality of the parameter space that must be explored, which can in practice increase computation time by an order of magnitude or more. Czekala et al. (2015) note that, because the best fit model parameters are relatively insensitive to the precise values of the covariance parameters (i.e. a reasonably good but perhaps not optimal covariance model often suffices), one can first roughly optimize the covariance model and then perform the MCMC fit with that model fixed. Given the computational demands of disk radiative transfer model fitting, we adopt a variant of that approach here.

We estimate the global covariance empirically by computing the average auto-correlation of the residuals from a subtraction of our 0.8 μm image and a subset of 1000 randomly chosen model disk images from a uniform sampling of the parameter

space within the limits of our priors (Figure 6.7). This provides, in a computationally tractable way, a reasonable model for the covariant structure found in residuals for the parameter space of interest, and allows us to hold the covariance model fixed in subsequent MCMC runs. We collapse the 2D autocorrelation along the horizontal axis to generate a 1D autocorrelation function (Figure 6.8). The horizontal axis was chosen because it provided the most conservative estimate, with a wider tail similar to the Matern kernel and did not exhibit the anti-correlation found in the vertical axis due to the dark lane of the disk. For comparison, we also show several $\nu = 3/2$ Matérn kernels following the chosen formalism for Czekala et al. (2015). To compute the covariance matrix K^G, for each pair of pixels i, j, we compute the distance between them given by $r_{i,j} = \sqrt{(x_i - x_j)^2 + (y_i - y_j)^2}$. For each entry of $K^G_{i,j}$, the analytic autocorrelation function is interpolated to the value for $r_{i,j}$, with a cutoff outside of 20 pixels to make computations of $C_{i,j}$ manageable. The resulting covariance matrix is shown in Figure 6.9.

For consistency, we also compute the likelihood of each model SED using the covariance matrix framework from Equation 6.4. In this case, the covariance matrix contains only the individual uncertainties for each point multiplied by an identity matrix. We neglect any global limitations of the model SEDs to fit the dataset. Given the low χ^2 values achieved for the SED fitting in the grid search described above (lowest SED $\chi^2 \sim 1.3$), we believe the uncertainties in the SED are well estimated. For our dataset, we do not anticipate covariances between neighboring photometric

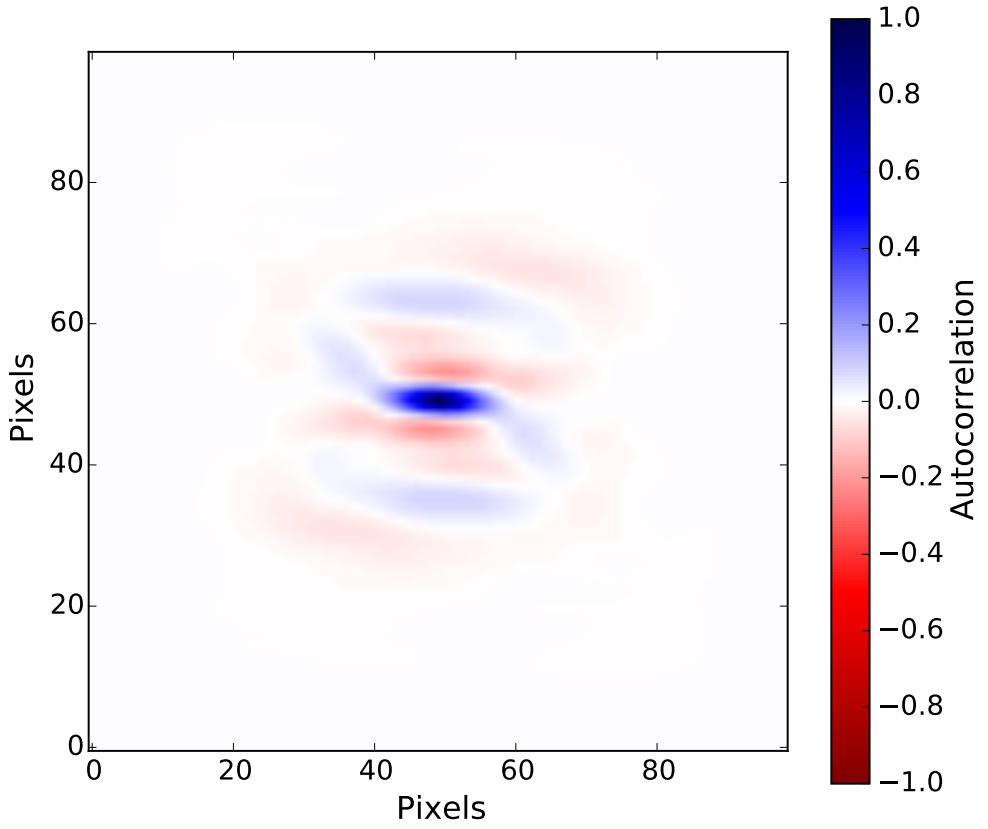

Figure 6.7 The mean of the autocorrelation of the residuals from subtractions between our 0.8 μm observed image and a randomly selected subset of 1000 model images spanning the range of our priors. Residuals are most strongly correlated between pixels that are horizontally adjacent, as expected for an edge-on disk with its major axis oriented horizontally. The slight anti-correlation in the vertical direction is likely due to dark lane structure between the two bright lobes

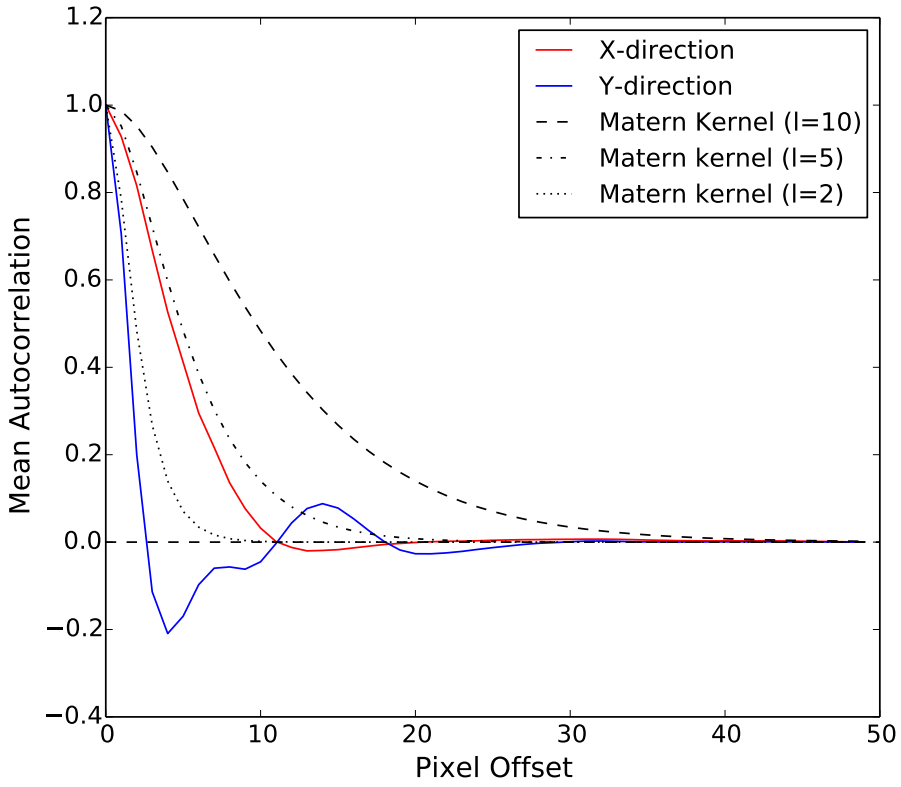

Figure 6.8 Slices through the mean autocorrelation shown in Figure 6.7. We show both the vertical (blue) and horizontal (red) slices along with several Matern kernels for comparison. We conservatively adopt the wider correlation scale from the horizontal axis to generate the global covariance matrix. It is not unsurprising that the autocorrelation image is more broadly extended in the horizontal direction where the disk is elongated than in the vertical where the gradients in the disk are much sharper.

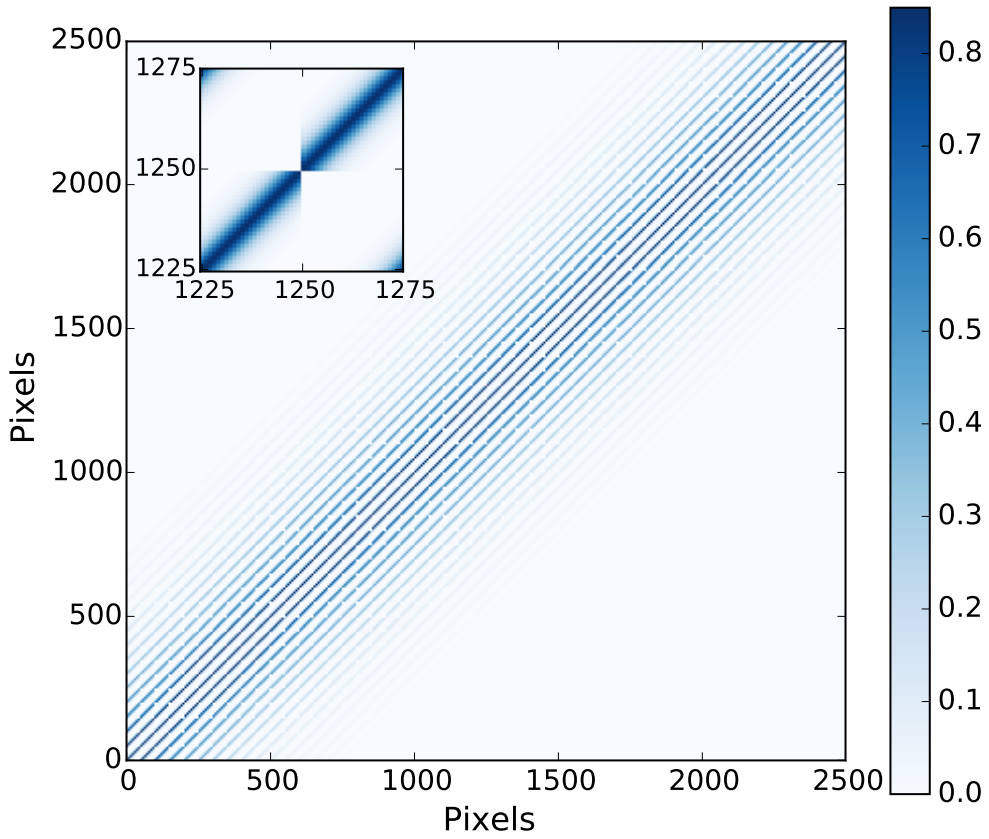

Figure 6.9 Covariance Matrix ($C_{i,j}$) used to compute the log likelihood of the model images given the observations. The matrix combines informaton about the noise in the observations, the covariances between adjacent pixels, and the pixel mask. The inset shows a zoomed in region illustrating the contribution of the autocorrelation function between adjacent pixels. To generate this we first unwrapped the 2D 50 $\times$ 50 pixel image into a 1D 2500 pixel array by stacking each row horizontally. The diagonal of the covariance matrix gives the uncertainties associated with each pixel (where $i = j$). The other elements of the covariance matrix dictate the covariances between the various pixel pairs (i, j) which is given by the autocorrelation shown in Figure 6.8 and depends on the distance between pixel i and j in the 2D detector frame (not in the 1D unwrapped image).

points, but this formalism would naturally handle any such correlations, and likewise makes it straightforward to include continuous spectra as part of a unified fit alongside broadband photometry.

The covariance framework is also capable of including model terms for additional regions of locally covariant structure (K^L), as discussed in Czekala et al. (2015). We leave the application of such local covariances to disk image fitting for a future work. Likewise, we leave for later exploring how best to explicitly model covariances between the SED and image portions of the overall fit.

6.3.4.3 Choice of parameter values for MCMC

The allowed parameter ranges were adjusted slightly for the MCMC modeling compared to the grid fit. The computation time for the grid modeling depended both on the number of free parameters, and on the size of the allowed parameter ranges, while the MCMC modeling time depended only on the number of free parameters. Therefore, we were able to widen the prior distributions for the MCMC modeling, being careful to widen allowable ranges for those parameters that were best fit at the edges of the grid distribution like the scale height and disk mass. Parameter ranges are shown in Table 2, Column 3. During the IDL grid search modeling phase, we found that the image and SED fits both prefer a large maximum grain size. In order to limit the computation time in the MCMC fits, we chose to fix the maximum grain size to be 3000 μm, and as noted above fixed the porosity at zero.

One downside to the MCMC over the grid search approach is that the chain does not work well with discrete parameter distributions. For example, the abrupt distinction between the tapered and sharp edged disk models could not have been tested using MCMC. Given the strong support for the tapered edge disk model as described in Section 6.3.3.2 we select an exponentially tapered outer edge for the MCMC run.

We conducted an MCMC run using the covariance-based log-likelihood goodness of fit metric with 2 temperatures with 50 walkers. We used uniform prior distributions for all of our parameters (with the dust mass uniformly distributed in log-space). We allowed the chain to run for $N_{\rm steps} = 10,000$, with an initial burn-in stage of $N_{\rm burn} = 0.2\,N_{\rm steps}$. This resulted in a total of 21,000 models requiring $\sim$ 2 weeks of computation time parallelized over only 10 cores. This was a significant improvement over the grid search approach which necessitated generating $\sim$ 200,000 models. As a test of convergence, we compute integrated autocorrelation times (τ_x) for each of our parameters and use this to estimate our effective sample size, ESS = $N_{\rm samples}/(2\tau_x)$ (a measure of the effective number of independent samples in the correlated chain). The ESS varied from 761 to 12075 with the surface density exponent being the least well constrained parameter. The Monte Carlo standard error for each parameter decreases with increasing effective sample size as $\sigma_i/\sqrt{ESS}$ where σ_i is the standard deviation for the posterior distribution (See discussion in Sharma, 2017). For example, to measure the 0.025 quantile to within $\pm$0.01 with a probability 0.95 requires 936

uncorrelated samples (this corresponds to roughly 10% errors in the best fit parameter values assuming the tail of the posterior is well described by a normal distribution), which is achieved for all parameters except the surface density distribution where we only confine the 0.025 quantile to within roughly ± 0.0125 (Raftery & Lewis, 1992).

6.3.5 Results and Conclusions from MCMC

The best fit parameter values are shown in Table 6.3. The data are best fit by a tapered-edged disk with an inclination of $83.0^{+2.6}_{-4.8}$ degrees, a scale height of $16.2^{+1.7}_{-2.0}$ au at a reference radius of 100 au, a total disk mass of $0.00057^{+0.00017}_{-0.00022}$ $M_{\odot}$ (assuming a gas to dust ratio of 100), a surface density exponent (α) of $-1.77^{+0.94}_{-0.14}$, and a flaring exponent (β) of $1.19^{+0.09}_{-0.08}$. The image and SED combined best fit model is illustrated in Figure 6.10 (single best fit in red, along with an ensemble of well-fitting models in gray) and together provide a close fit to the observations. Parameter distributions are shown in Figure 6.11. The results for individual parameters are discussed in more detail below.

The best fit parameters provide a compromise between the image and SED fit. Therefore, this combined fit to the SED and image is not as favorable as if the fits had been performed separately on each individual dataset. For example the best fit model under-predicts the flux in the 20 - 100 μm region of the SED (by a factor of 20 at 20 μm and 1.5 at 70 μm), while the image under-predicts the flux ratio between the top and bottom nebulae by a factor of ~ 4. The best image fits tend to over-predict the

Table 6.3. MCMC Best fit Paramters

Parameters	Best-fit Values
Inclination	$83.0^{+2.6}_{-4.8}$
Scale Height	$16.2^{+1.7}_{-2.0}$
Dust Mass	$0.00057^{+0.00017}_{-0.00022}$
Surface Density α	$-1.77^{+0.94}_{-0.14}$
Flaring β	$1.19^{+0.09}_{-0.08}$

Note. — Best fit values for the covariance likelihood estimation mode of the MCMC.

disk flux at all wavelengths, while the best SED fits produce images that have very steep surface density profiles, which removes the diffuse material on the outer edges of the disk provided by the tapered edge.

The apparent disagreement is likely a result of some limitations in the disk model. If the opacity of the dust grains in the disk was decreased, the optically thick/thin boundary would move to shorter wavelengths, recovering some of the flux in the several tens of μm range of the SED. However, to improve the flux ratio between the top/bottom nebulae in the modeled image we would need to move the inclination farther from edge-on and/or change the scattering properties of the grains (i.e. increase the forward scattering or decrease the dust albedo), which would most likely necessitate an increase in the dust opacity.

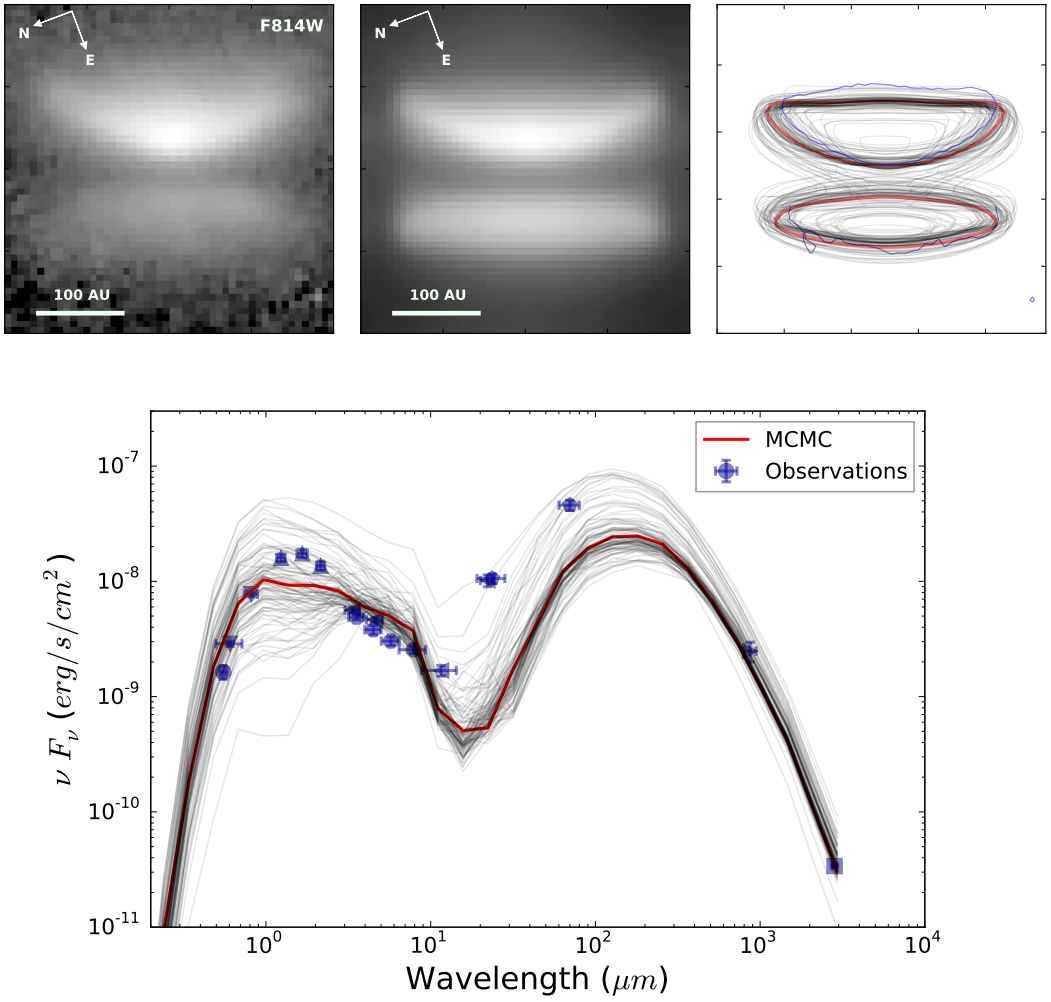

Figure 6.10 The results from the covariance-based MCMC. **Top:** The model image (Middle) corresponding to the best fit parameters given in Table 6.3 compared to the 0.8 μm observed image (Left). The right panel shows a contour highlighting the shape of the best fit model disk in red, with contours scaled to the observed 0.8 μm image shown in blue. In grey we provide 100 randomly chosen models drawn from the MCMC chain. **Bottom:** The SED for the same model as above is shown in red and compared to the literature values in blue. The grey curves present the same 100 randomly selected models drawn from the chain. While the MCMC results provide a reasonably good fit to both the image and SED, the compromise between the two datasets, inherent in the covariance framework, lead to imperfect solutions. For example the best fit model under-predicts the flux in the 20 - 100 μm region.

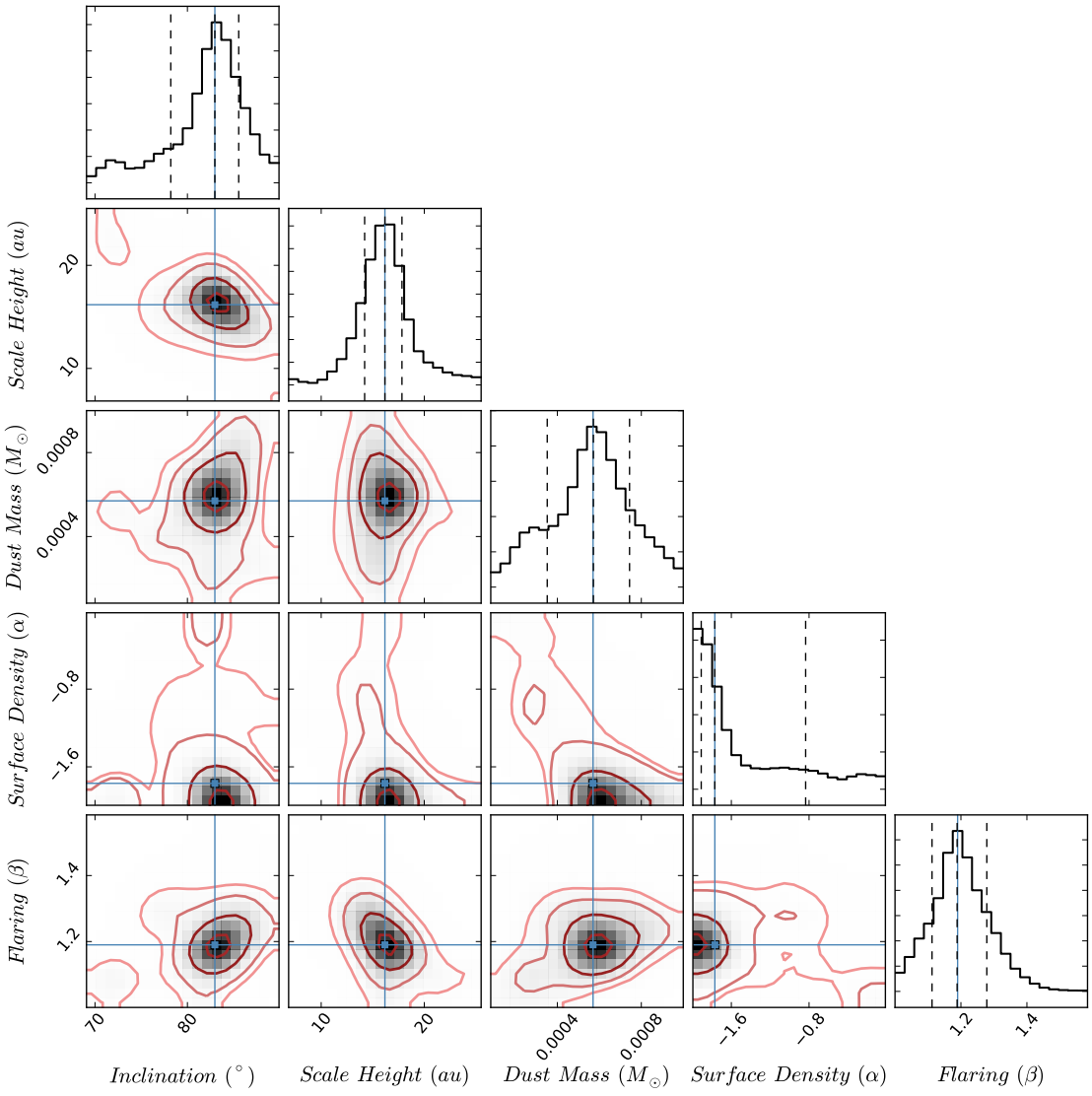

Figure 6.11 The MCMC results using the covariance log likelihood estimation. The blue crosshairs indicate the best fit value for each parameter. Shading indicates the density of the parameter space sampling, while the red contours are drawn at the 1-4σ levels. All parameters are well constrained except for the surface density exponent (α). Dashed vertical lines represent the 16th, 50th, and 84th percentiles of the samples in the marginalized distributions.

6.3.6 Dust Mass

Our best fit disk dust mass was $0.00057^{+0.00017}_{-0.00022}\,M_{\odot}$, which corresponds to a disk mass of 0.057 $M_{\odot}$ (assuming the standard ISM gas to dust ratio of 100). This is 16% of the stellar mass for a 0.35 $M_{\odot}$ star like ESO Hα 569, a surprisingly high disk to star mass ratio.

In the grid fit and preliminary MCMC runs, the fit to the disk mass relied heavily on the 870 μm measurement. Assuming the disk is optically thin at 870 μm, the measured flux corresponds to an estimated disk mass of $M(\mathrm{gas+dust}) = \frac{F_{\nu}D^2}{\kappa_{\nu}B_{\nu}(T)} = 0.0055 M_{\odot}$, where $\kappa_{\nu} = 0.03\,cm^2/g$ (Beckwith et al., 1990), we assume a gas to dust ratio of 100, and we use a characteristic temperature of $T = 20$ K. Given the surprisingly high mass estimate, we wondered if the 870 μm photometry might be in some way compromised, for instance if contaminated by excess flux from a background source. To test the dependence of the derived mass on this measurement, we tested running the MCMC code excluding this datapoint, but the overall fit still preferred high disk masses. We ultimately opted to include the 870 μm measurement in our fits.

Subsequent to the initial MCMC runs, Dunham et al. (2016) published 106 Ghz continuum observations with ALMA. Using the same millimeter flux to mass relation described above, though with a different assumption for the disk temperature (T=10 K) and a dust opacity characteristic of coagulated dust grains with thin icy mantles ($\kappa = 0.23\,cm^2/g$ Ossenkopf & Henning, 1994), they find a total disk mass

(gas+dust assuming a gas to dust ratio of 100) of $0.057 \pm 0.002 M_{\odot}$. This agrees very well with our best fit disk mass. For the final MCMC run, both this ALMA point and the 870 μm data were included. *The disagreement between the predictions from the 1.3 mm and 870 μm continuum measurements is unsurprising since derived dust masses from (sub)mm data alone are likely to be biased downwards in the case of EODs due to the large optical depth.* We note that this dust mass agreement between the millimeter continuum and scattered light imaging seems to indicate that the relative importance of absorption/emission and scattering of the dust model (which includes, but is not limited to, the dust albedo) used here is a reasonable approximation.

6.3.7 Scale Height

The best fit scale height of $16.2^{+1.7}_{-2.0}$ au (at 100 au) is consistent with the low mass of the central star. For a disk that is pressure supported and vertically isothermal with temperature, the Gaussian vertical density distribution is described by Equation 6.5 (Burrows et al. 1996):

$$H(r) = \sqrt{\frac{k_B T(r) r^3}{G M_{\rm star} \mu}} \tag{6.5}$$

where we assume a reduced mass (μ) of 2.3 If we adopt the best fit scale height value of 16.18 au at a reference radius of 100 au and calculate the temperature of the disk at this radius, we obtain T $\sim$ 23 K. This disk temperature agrees well with observations

of other edge-on disks (e.g. HH 30; Burrows et al., 1996).

Additionally, MCFOST is capable of producing the temperature structure within the disk along with the images and SEDs. This can be used as a cross check on the physical self-consistency of our best fit model parameters. The mass averaged temperature (across the vertical direction) for out best fit model at the reference radius (100 au) is $T = 29$ K. Surface effects that are exacerbated in scattered light could account for the slight discrepancy between the analytically and numerically estimated disk temperatures, as the surface gas is super heated by stellar radiation. The agreement between the dust scale height inferred from the image and the gas scale height computed from the model suggests that the dust grains are well-mixed vertically with very little dust settling, at least for the small dust particles that dominate the opacity at visible wavelengths.

6.3.8 Flaring Exponent

We obtain a best fit flaring exponent $\beta = 1.19^{+0.09}_{-0.08}$. Kenyon & Hartmann (1987) provide an analytical model for the temperature profile of a flared disk wherein the surface layers are heated by the direct stellar radiation and the energy is re-radiated thermally. Assuming the gas and dust are well mixed vertically, and that the incident angle of the stellar radiation on the flared surface is small, $T(R) = T(R_0)\left(\frac{R}{R_0}\right)^{2\beta-3}$. We fit the modeled mass-averaged disk temperature profile to this analytic solution and find that a flaring exponent of $\beta = 1.29$ is preferred. This value consistent within $\sim$

1σ of the model preferred value. Our best fit value is slightly shallower than has been predicted for other young, flared disks with $\beta = 1.3 - 1.5$ (e.g. Chiang & Goldreich, 1997). This could be an indication of early dust settling in the disk, decoupling the dust and gas and changing the disk thermal pressure profile. In this model we assume dust particles of all sizes are evenly distributed vertically throughout the disk. An investigation into the effect of settling of larger grains to the disk midplane is left for future work.

6.3.9 Surface Density Exponent

The surface density exponent is best fit by $\alpha = -1.77^{+0.94}_{-0.14}$, which is near the lower edge of the allowed parameter space. However, allowing for steeper surface density profiles would push the models into a highly unphysical range. The SED favors a very steep surface density profile (also seen for HV Tau C: Duchêne et al., 2010), while the images favor a shallow profile with a more gradual taper at the disk edge. It is possible that the steep best fit surface density profile is a reaction to the large disk masses required to fit the mm data in the SED, whereby mass is being concentrated in the center of the disk, where our dataset is poorly equipped to constrain the disk properties. We did not expect the SED to have a strong dependence on the surface density slope. The disk is expected to be very optically thick across most of the IR portion of the SED. Consequently, the surface density profile would not impact the location of the disk scattering surface which is intercepting and re-radiating light from

the central star. It is possible that a degeneracy between surface density exponent and some other star/disk property is influencing this fit (e.g. stellar luminosity, dust albedo, etc.).

It is unexpected that a disk surface density power law would be steeper than the $\alpha = -1.5$ value for the minimum mass solar nebula (Weidenschilling, 1977). Indeed, Andrews & Williams (2007) conducted a resolved submillimeter continuum survey of circumstellar disks and find a mean value of $\alpha = -0.5$. Instead this steep profile is probably indicative of some shortcoming in our model parameterization. Invoking separate power laws for the inner and outer regions of the disk may provide a solution, but is beyond the scope of this paper. While we have spatially resolved images at optical wavelengths, the disk is highly optically thick and we are unable to see any effects of radial density gradients. This would require resolved images at wavelengths where the disk is optically thin (e.g. resolved millimeter continuum images, though it is uncertain if the disk is truly optically thin at these wavelengths). Scattered light imaging alone simply does not constrain the surface density exponent in the innermost regions of the disk. Previous studies of the radial structure of protoplanetary disks observed in millimeter continuum find surface density profiles that are generally shallower than presented here, though there are a few exceptions (e.g. DG Tau, GM Aur; Guilloteau et al., 2011). Estimates of the surface density distributions inferred from resolved mm data at different wavelengths vary widely (Isella et al., 2010), suggesting that these disks are not optically thin even in the 1-3

mm range.

6.4 Discussion

6.4.1 Mass and Stability of the Disk

The best fit dust mass ($0.00057\,M_{\odot}$ or $190\,M_{\oplus}$) and the associated total (gas + dust) disk mass ($60\,M_{Jup}$, assuming a gas-to-dust ratio of 100) imply a disk mass to star mass ratio ($M_D/M_{\rm star}$) significantly higher than expected for its age and spectral type. Williams & Cieza (2011) provide a review of protoplanetary disks and report a relatively flat distribution of disk masses when spaced logarithmically, with a sharp drop outside of $\sim 50\ M_{Jup}$, and an average disk mass to host stellar mass ratio of 0.01 albeit with large scatter. The median mass (assuming a gas-to-dust ratio of 100) of disks around GKM spectral type hosts is 5 M_{Jup} (impying a dust mass of $\sim$16 $M_{\oplus}$).

This trend of low $M_D/M_{\rm star}$ mass ratios seems to continue for low mass stars. van der Plas et al. (2016) conducted a survey of disk masses for low mass stars with ALMA, finding a range of masses between 0.1 and 1 $M_{\oplus}$ for their eight targets. One target in their sample, Allers 8 (an M3 star with a mass of 0.34 $M_{\odot}$), has similar stellar parameters to ESO Hα 569, but a significantly lower dust mass of 1.05 $M_{\oplus}$. However, the bulk of the disks in their sample are located in the Upper Scorpius SFR ($\sim$ 10 Myr; David et al., 2016) and are older than our target. The authors have an additional dataset for the younger Taurus SFR, with preliminary estimates for

the dust mass upper limit of 25 $M_{\oplus}$ for a sample of stars with an earliest spectral type of M4 (Ward-Duong, private communication). Additionally, Andrews et al. (2013) conduct a survey of the protoplanetary disks with low mass hosts (spectral types earlier than M8.5) in the Taurus SFR and find slightly higher disk masses. The authors estimate the disk masses from their mm-wave continuum luminosity, and find that the median disk mass to stellar mass ratio is 0.3%, with very few disks having a ratio of $\geq$ 10%. Targets in their sample in the M3-M4 spectral type range have disk dust masses of 2-17 $M_{\oplus}$, with an average of 9 $M_{\oplus}$.

While uncommon, protoplanetary disks with large disk masses aren't unprecedented. Duchêne et al. (2010) model scattered light images and SEDs for the HV Tau C system and find a best fit dust mass of $M_{dust} \geq 10^{-3}\,M_{\odot}$ which gives $M_D/M_{\rm star} \sim$ 0.2 (meaning the disk is 20% the mass of the central star) assuming a gas-to-dust ratio of 100. Likewise, Duchêne et al. (2003) model a mm image of the HK Tau B protoplanetary disk and get a best fit total disk mass of $M_{disk} \simeq 2 \times 10^{-2}\,M_{\odot}$, which gives $M_D/M_{\rm star} \sim 0.04$ (4% of the stellar mass). Glauser et al. (2008) present an in-depth study of the IRAS 04158+2805 disk using images in the optical, NIR, polarization maps in the optical and mid-IR and X-ray spectra. The dust mass is constrained to be $M_{dust} = 1.0 - 1.75 \times 10^{-4}\,M_{\odot}$, which also gives $M_D/M_{\rm star} =\sim 0.04$ (4%). All three disks are in the Taurus SFR, and the first two disks above are in multiple systems. Likewise, all of these sources are viewed edge-on. It is possible that the large inferred disk masses could be the result of a selection effect (observations

of edge-on disks are only sensitive to the most massive disks), or some artifact of our fitting method which compensates for missing physics by placing more mass in the disk. The fit for the dust mass is driven by the SED, but the spectral coverage is poor in the millimeter. The mass estimates could be reduced by including larger opacities in the mm, for instance by adding amorphous carbon into the mixture, or by using a more complex, nonuniform particle distribution.

Throughout this paper we have assumed a gas to dust mass ratio of 100 as is typical of other young disks and the ISM. However, very recent work by Long et al. (2017) estimate the gas mass around ESO Hα 569 from ALMA ^{13}CO line emission and find only $\sim 1.3\,M_{Jup}$ of gas mass in the disk, though optical depth effects and details of the CO freeze-out are likely to introduce major sources of uncertainty. Combined with our own dust mass estimate, this gives an uncharacteristically low gas to dust ratio of only ~ 2. While gas depletion in the disk would lower the unusually high best fit total disk mass, the flared appearance strongly confirms this is a young pressure-supported gas+dust disk. A gas to dust ratio of 2:1 is suggestive of a later evolutionary stage. This disagreement highlights the challenges of measuring disk masses for EODs, which are generally optically thick even at millimeter wavelengths.

The MCMC radiative transfer fit prefers a disk with an abnormally large disk mass that is $\sim 16\%$ the mass of the central star. For a disk this massive, it is unlikely that the disk would remain gravitationally stable. We investigate the stability of the disk via the Toomre Q parameter.

$$Q = \frac{c_s \kappa}{\pi G \Sigma} \tag{6.6}$$

where c_s is the sound speed in the disk, κ is the epicyclic frequency, and Σ is the surface density profile of the disk. For a vertically isothermal disk with a Keplerian velocity, $\kappa = \Omega = \sqrt{\frac{GM_{D?}}{R^3}}$ and a sound speed $c_s = \sqrt{\frac{k_B T}{\mu m_p}}$ where we assume a reduced mass (μ) of 2.3. Figure 6.12 shows the radial profile of the Toomre Q parameter. It shows that the disk appears to be unstable inside of $\sim$ 2.6 au.

It is worth noting here that we do not expect to have a good constraint on the properties of the inner regions of the disk from scattered light imaging and the SED alone. Any change in the interior structure (e.g. an inner wall, spiral structure, or a broken surface density power law) of the disk would affect stability. A steeper inner surface density profile would prevent instability, though such a sharp profile is unlikely. Each of these mechanisms would increase the variability of the system, possibly accounting for the observed variability in several of the photometric points included in the SED.

6.4.2 ESO Hα 569 Compared to Other Cha I Disks

Rodgers-Lee et al. (2014) conducted a survey of disks in Cha I as identified from IR excesses in the SEDs. For 34 objects, disk masses were estimated. The median of the distribution of disk masses is 0.005 $M_\odot$, which corresponds to 0.5% of the stellar

mass, while the tail of the distribution stretches to 0.1 $M_{\odot}$ for more massive central stars. ESO Hα 569 is a clear outlier with 10 times more mass than the median value.

The Luhman (2007) survey of Cha I names six members as likely edge-on disk candidates because they are underluminous for their spectral type and are seen in scattered light (CHSM 15991, T14A, ISO 225, ESO Hα 569 and 574, and Cha J11081938-7731522). The sixth object, Cha J11081938-7731522, appears extended in their survey with a butterfly morphology, providing further support that these targets are all likely edge-on disks. We observe two members of this list, ESO Hα 569 and 574 in our HST campaign and confirm that both are edge-on protoplanetary disks.

6.4.3 A Deficit of Edge-on Disks?

Luhman et al. (2008) use Spitzer colors to estimate the disk fraction as a function of stellar mass. For stars of spectral type between K6 and M3.5 the disk fraction in Cha I is 0.64 $\pm$ 0.06 disks per star. If we multiply this fraction by the fraction of disks expected to have inclinations between 75 and 90 degrees, we would expect to find roughly 17% of stars hosting edge-on disks. However, a recent survey of 44 YSOs hosting circumstellar disks detectable with Herschel found only 2 edge-on disks (Rodgers-Lee et al., 2014) as classified from the SEDs. While the sample size of this survey is small, this surprising lack of known EODs is a common phenomena seen for many SFRs (Stapelfeldt et al., 2014), and was one of the key motivating factors

for our HST survey. While that program doubled the number of known EODs, the increased sample remains smaller than would be predicted from purely geometrical grounds. This suggests that many disks must be near-edge-on but with insufficient material and/or vertical extent to block the direct light of the star. Flatter disks, with lower H/R values than ESO Hα 569, would only appear edge-on for a narrower inclination range. For instance if the "typical" young disk is flared enough to only occult its star within 5 degrees, Considering a range from 85 to 90 degrees would give an edge-on disk fraction per star of 4%, more in line with what is observed.

Alternatively, this could suggest that the 'typical' double peaked SED assumed for edge-on disks may only present for the disks with an unusually high disk mass. The targets for this edge-on disk survey were selected based on the shape of the SEDs. Specifically, targets with a doubled peaked SED, where the stellar peak flux was of order the same as the dust peak flux in the IR. Figure 6.13 shows the effect of changing dust mass on the structure of the SED, and the scattered light image for a fixed inclination. Disk masses shown are for our best fit disk mass divided by factors of 3, 10, 30 and 100. After dividing by a factor of 10 (for a more reasonable $M_D/M_\odot \sim 0.016$) the double peaked structure has disappeared, and we would not have included this target in our sample. It is possible that this could account for the relative lack of known edge-on disks; the selection metrics used are biased towards detecting only the most massive disks, as they require fairly large line-of-sight opacities. Likewise, we are more likely to find EODs in the earliest stages before dust settling causes

additional decreases in the line-of-sight opacity, also contributing to the low observed EOD frequency.

It is therefore possible that the edge-on disk detections thus far are outliers in the population of young disks. Double-peaked SEDs alone are an insufficient indicator of the edge-on disk fraction, and images in scattered light or thermal emission with high spatial resolution are required to determine the true nature of these objects. Existing surveys of young, nearby SFRs tend to have selection biases towards more face-on systems and are dependent on the cloud properties and the science drivers of the survey. In order to determine the true edge-on disk fraction and to confirm or deny that the high disk mass of ESO Hα 569 is indeed representative of the population of protoplanetary disks, we would require a uniform sample of disk observations at sufficiently high angular resolution.

6.5 Summary and Conclusions

We have resolved the disk around ESO Hα 569 in scattered light with HST/ACS and unambiguiously confirm that it is an optically thick protoplanetary disk viewed nearly edge-on. We performed radiative transfer modeling using a variety of fitting techniques to constrain the geometry and grain properties of the disk. We successfully combine a covariance-based log likelihood estimation with an MCMC framework to simultaneously fit the scattered light image and literature compiled SED for

ESO Hα 569. Our main results are as follows:

- We find that a tapered-edge disk structure, with an exponential falloff of material outside of the apparent outer radius, is necessary to generate the diffuse scattered light emission above the disk midplane, the flux ratio between the top/bottom nebulae of the disk, and the width of the dark-lane simultaneously.

- Our best fit disk mass of 0.057 $M_{\odot}$ is abnormally large, especially considering the small central object, though multiple mm continuum observations support this estimate. The disk to stellar mass ratio of ~ 0.16 generates stability issues in the inner few au, though none of our modeled observations are capable of tightly constraining properties of the inner regions of the optically thick disk.

- The vertical structure of the disk as defined by the scale height and the power law flaring exponent is well constrained. The best fit model has a mass-averaged disk temperature of ~ 23 K, similar to other disk observations. The scale height is self-consistent with the modeled temperature profile, supporting a flared disk model in which the gas and dust are well-coupled.

A large effort was put into simultaneous and consistent fitting of the images and the SEDs, resulting in a disk model that is is a good compromise between the two. But naturally a separate fit to each individual observable is capable of yielding a better fit to that one, at the cost of an inferior fit to the other. This is likely due to (1) limitations in how we have parameterized the complex physical processes ongoing in

protoplanetary disks (in this work we have used a fairly simple analytic disk structure formalism with a single grain population), and (2) the inability of our dataset to investigate some of the relevant physics and processes (e.g. neither the SED nor the scattered light image provide much information on the innermost regions of the disk).

Using a combination of different observables (spectral data, images in scattered light, and thermal emission, and polarimetry data to constrain grain properties) helps to break degeneracies between various model parameters. However, care must be taken to determine the correct approach for the relative weighting of observables with different noise properties and model sensitivities. Now that high contrast imaging systems designed to study these circumstellar environments in greater detail are coming on line, there is a plethora of great observations for disks in a wide range of evolutionary stages which formed under a range of initial conditions. We may be entering an era where we have statistically significant numbers of circumstellar disk observations to employ population synthesis techniques. This is an important step if we hope to understand the inherent physics in the disk and planet formation processes. The tools we have been developing take us a step closer to being able to consistently make fits and measurements to e.g. the entire known sample of edge-on disks.

To better constrain the ESO Hα 569 disk and stellar parameters, we would need to incorporate resolved images at multiple wavelengths. We chose not to model the 0.6 μm image because of the contamination from the jet. However, we have recently

obtained resolved images in the F475W filter and will use this to probe the diffuse scattering material high up above the disk in a forthcoming paper. Additionally, we have recently been awarded an ALMA Cycle 4 program (PI: F. Ménard) to map the thermal emission from 15 confirmed edge-on disks from our HST sample at 870 μm and 2 mm to probe dust settling, migration and grain growth. Spatially resolved millimeter observations should go a long way toward disentangling many of the outstanding uncertainties regarding this disk's structure. Looking forward, with the launch of JWST, the MIRI MRS integral field spectrograph will provide spatially- and spectrally-resolved data across the entire 5 - 30 μm range for many disks. This would not only help us to constrain the structure of the disk in a regime where the current SED fit particularly struggles, but also provide valuable and detailed information about the dust species within the disk.

6.6 Appendix

Here we provide a simplified disk model fitting effort designed to illustrate the effect of the two 'goodness of fit' metrics used in the MCMC explorations of parameter space: χ^2 and covariance log-likelihood based estimation described in Sections 3.4.1 and 3.4.2 respectively. While this demonstrates the power of the two tools, we recognize that it is not a comprehensive test of performance. A full benchmarking effort of the `mcfost-python` package is beyond the scope of this paper.

To test the ability of both fitting metrics, we generate an MCFOST model with known parameter values, add randomly generated 1σ noise to both the MCFOST produced image and SED, and attempt to retrieve the parameters. The model was randomly drawn from the ESO Hα 569 MCMC chain described above. We perform a fit to this synthetic dataset using both the χ^2 and covariance log-likelihood based estimation. For simplicity, we choose only to fit the scale height and inclination of our modeled disk. We expect both methods to recover the known parameter values within the uncertainties. Parameter values used for the synthetic dataset are shown in Table 6.4.

To illustrate the power of the covariance framework over the χ^2 fitting technique, we perform the same test, but purposefully input a disk dust mass too low by a factor of 10 into the MCFOST parameter file. This will test how robust the covariance framework in the presence of clear limitations in the model's ability to fit the data.

In an effort to conduct these tests as close to the MCMC results reported above, we use the same Parallel Tempered ensemble sampler with two temperatures and 50 walkers. With only two free parameters, the chains converged more quickly, requiring only $N_{\rm steps} = 10000$ with $N_{\rm burn} = 0.2\,N_{\rm steps}$. The allowable parameter ranges for the inclination and scale height were the same as reported in Table 2.

Figures 6.14 and 6.15 present the results for the Covariance and χ^2 fitting techniques, respectively. Both methods retrieve the input inclination and scale height within the uncertainties when using the correct dust mass. However, when the dust

Table 6.4. Parameter values for the Synthetic Dataset

Parameters	Values	Notes
Inclination	71.6°	Allowed to vary.
Scale Height (R=100 au)	25.6 au	Allowed to vary.
Dust Mass	$4.94 \times 10^{-4}\, M_{\odot}$	Held constant[a]
Surface Density α	-1.76	Held constant.
Flaring β	1.54	Held constant.

[a]This value was held constant for all runs, however, a value of $4.94 \times 10^{-5}\, M_{\odot}$ (0.1 times the actual value) was used to test the robustness of the fitting techniques to systematic model errors.

mass is set to one tenth the actual value, both fitting methods struggle to retrieve the correct parameter values. The covariance run successfully recovered the disk scale height, thought the uncertainties are larger than the correct dust mass case. The inclination was found to be $77.7^{+5.1}_{-2.6}$ degrees, which is only $\sim 2\sigma$ discrepant from the true value. With the incorrect disk mass, the χ^2 run was unable to recover either parameter. The scale height of the disk is not well constrained at all, while the likelihood distribution for the inclination is sharply peaked at $79.8^{+1.1}_{-0.6}$ degrees, which is $\sim 14\sigma$ discrepant from the true value. It is unsurprising that the covariance framework is much more robust to global limitations of the models to fit the dataset.

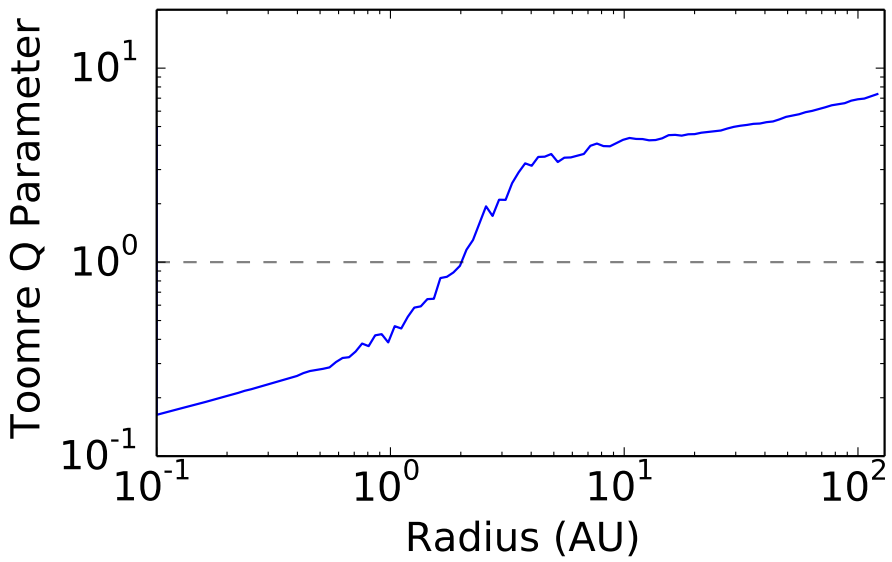

Figure 6.12 Radial profile of the Toomre Q parameter for our best fit disk. The disk appears to be likely unstable inside of 2.6 au.

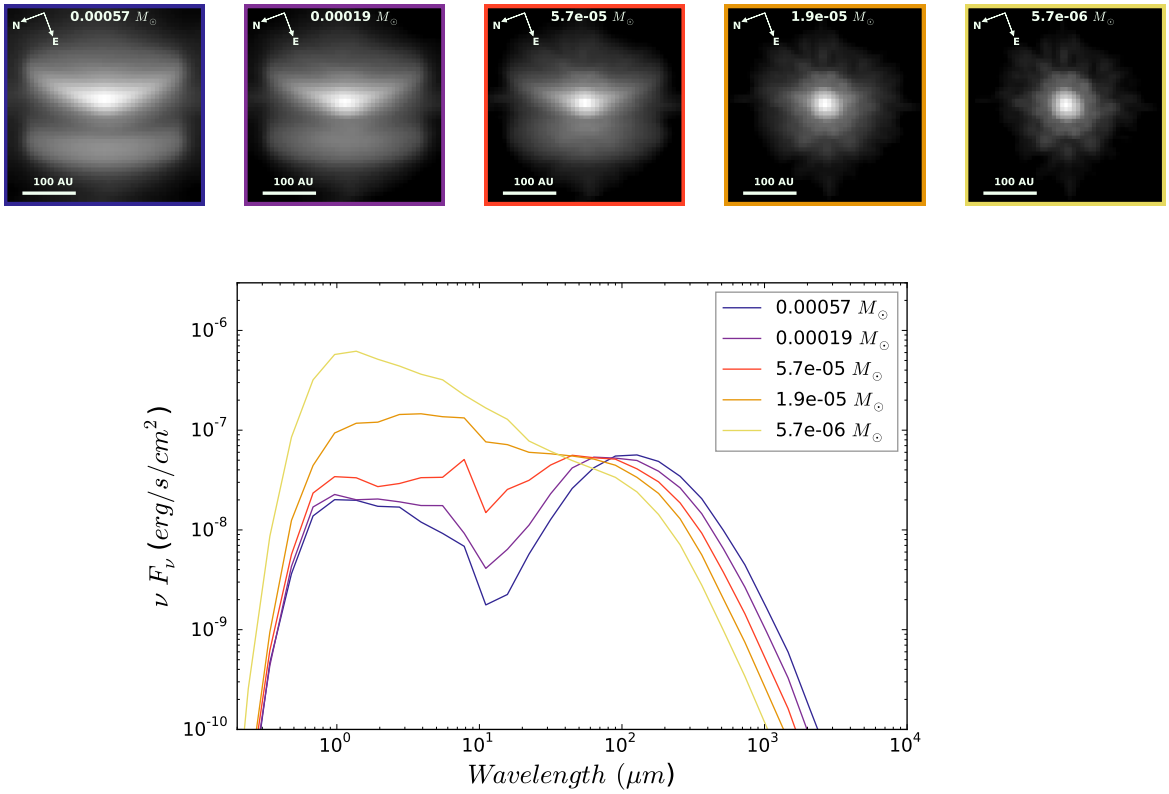

Figure 6.13 We show the evolution of the shape of the image and SED for different dust masses. Our best fit model is shown in blue. The other models use the same parameter values except for the mass, which is some fraction of the best fit dust mass as indicated in the legend. For a fixed inclination, decreasing the dust mass moves photons from the thermal peak in the SED to the scattered light peak. Decreasing the mass by a factor of 10 generates a flat SED without the double peaked structure. Likewise, if the dust mass is one tenth the best fit value, the double nebula shape begins to disappear in the scattered light image, and is not seen at all in the $1.9 \times 10^{-5}\,M_\odot$ model.

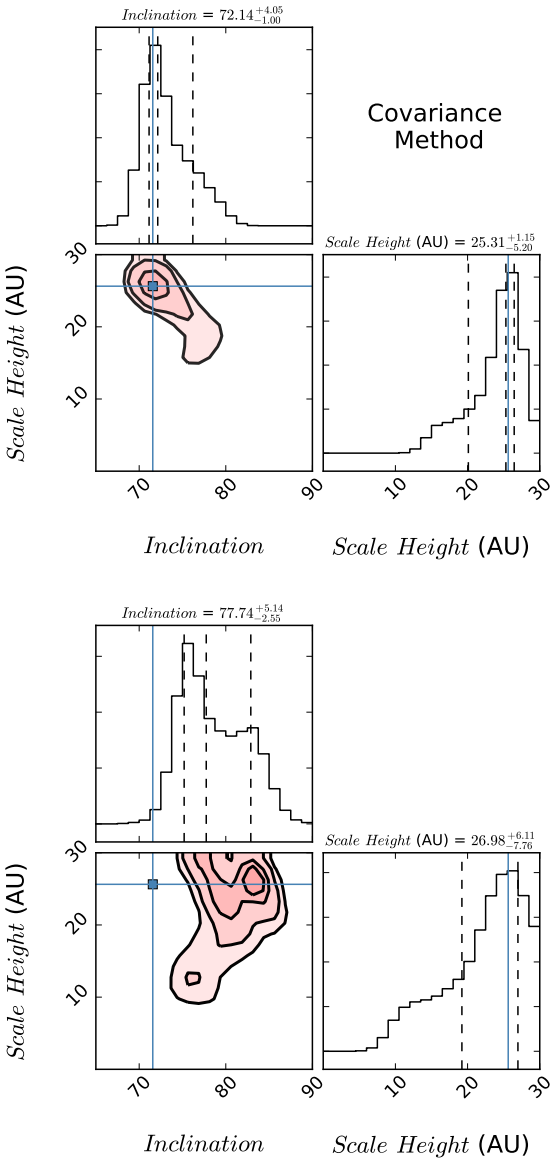

Figure 6.14 **Left:** MCMC results of the covariance log-likelihood estimation fit using a synthetic dataset. We fit only the scale height and inclination of the modeled disk. The blue lines correspond to the known values for each parameter. The correct parameter values were retrieved, and the distributions are sharply peaked. **Right:** Same as the left panel, but the MCMC run was conducted using an incorrect disk dust mass in the MCFOST parameter files. Even assuming a depleted dust mass, the scale height of the disk is still recovered, while the best fit inclination is $\sim 2\sigma$ discrepant. The covariance framework is less sensitive to any global limitations of the disk model to fit the given dataset.

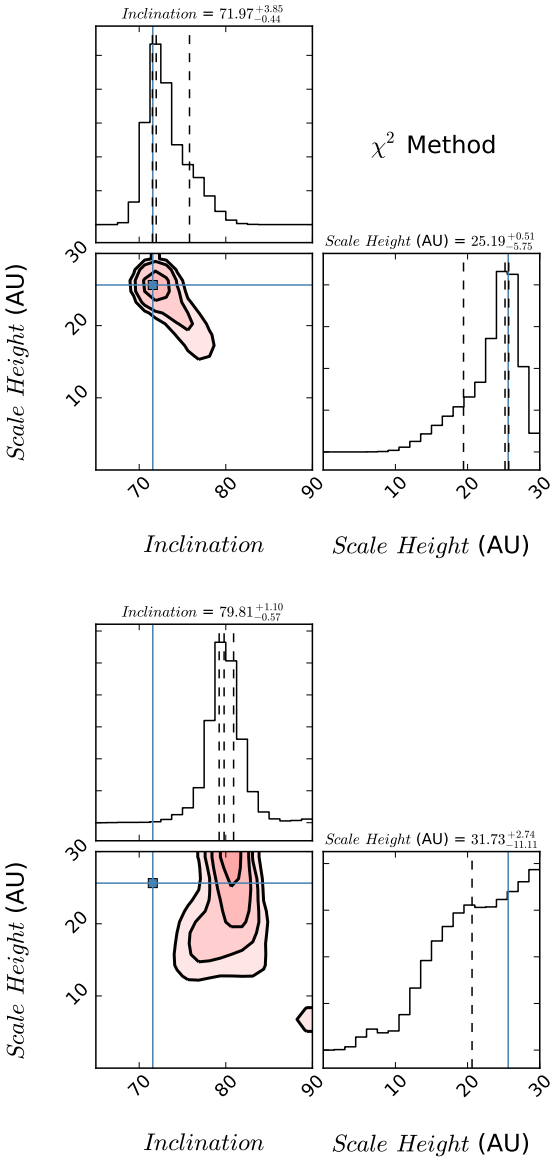

Figure 6.15 Same as figure 6.14 but the MCMC was run using the χ^2 log-likelihood based estimation rather than the covariance framework. Unlike the covariance case, the χ^2 fitting metric has a difficult time retrieving any of the correct parameter values when the incorrect disk dust mass was used to generate each MCFOST model. The disk scale height is not well constrained at all, and the best fit inclination is $\sim 14\sigma$ discrepant.

Chapter 7

Conclusion

7.1 Predominant Results

Here I have presented a series of works in the detection and characterization of circumstellar systems. In Chapters 2 and 3, I present the wavelength calibration for the Integral Field Spectrograph of the Gemini Planet Imager high contrast instrument. This work provides a wavelength uncertainty of only ~ 0.2 nm across all filters, and has enabled some incredible science, namely the spectral characterization of one of the lowest mass extrasolar planets ever discovered via direct imaging, 51 Eridani b, the most comprehensive spectrum for any exoplanet yet for Beta Pic b, characterization of several brown dwarfs, studies of potential planetary candidates within the HD 100546 disk, and many more. This software has benefited not only the GPI Exoplanet Survey, but also the many other community GPI projects.

I have also presented my work on the observation and characterization of three circumstellar systems. Polarization observations of the PDS 66 disk show a radial surface brightness distribution described by a broken power law indicative of an evolving disk. The apparent disk gap from 45 to 80 au could be a physical clearing of dust due to e.g. a perturbing planet embedded in the disk below our detection threshold. As this disk is optically thick, and the polarized intensity images are only sensitive to the disk surface, the gap could also arise from shadowing from some interior feature (e.g. an enhanced inner wall) or some localized change in the dust particle properties changing the degree of scattering. Additionally, we detect an azimuthal asymmetry rotating at some undetermined timescale.

Moving to longer wavelengths, millimeter continuum observations of the DH Tau system allows us to place limits on the disk mass of the wide separation planetary mass companion, DH Tau b. The disk dust mass upper limit of $0.09\,M_{\oplus}$ is at least three times lower than we would expect for such a young object, giving support for a formation scenario involving core accretion closer into the central star coupled with a dynamical scattering event forcing the planet out to a much larger semi-major axis and disrupting the disk. While other formation scenarios aren't ruled out by this dataset, DH Tau seems to follow a trend among wide separation PMCs with lower than expect dust disk masses.

Lastly, I presented HST observations of the edge-on protoplanetary disk ESO Hα 569. In order to characterize this disk, I developed a complex set of modeling tools

designed to explore disk properties quickly and efficiently while providing an estimate of the uncertainties and properly weighting the information provided by different observables. The covariance log-likelihood estimation technique was successful in combining both scattered light imaging and a spectral energy distribution. The flared disk has a best fit scale height of 16 au, which is self-consistent with the modeled disk temperature profile, indicating that the gas and dust are well mixed. All evidence supports an uncharacteristically high disk mass for this target with an unusually steep surface density power law distribution forcing the disk to become unstable in the inner few au. We investigate the possibility that the unexpectedly low observed edge-on disk fraction coupled with the high disk masses of those few resolved edge-on disks is an observational bias rather than an indication of the true underlying distribution. Together, individual disk characterization efforts provide a global view of the processes ongoing in evolving disks.

7.2 Further Discussion

In order to gain a full picture of the planetary system formation process, in depth studies of individual objects viewed at different stages in the life cycle of a circumstellar system are necessary to examine the processes of grain growth and interactions between planets and disks. Workhorse high contrast direct imaging instruments like the Gemini Planet Imager will provide a large population of resolved disks and ex-

oplanets at large separations to elucidate the underlying physics of these structures. I intend to use the software toolkit I created that allows for fast and efficient model fitting of a wide variety of circumstellar environments using different instruments. Using these tools, I hope to continue radiative transfer modeling of GPI and HST disk targets with a focus on systems with both planets and disks when available.

Furthermore, combining different observables (spectral data, images in scattered light and thermal emission, and polarimetry data to constrain grain properties) helps to break degeneracies between various model parameters. We are entering an era where we have statistically significant numbers of circumstellar disk observations to employ population synthesis techniques. This is an important step if we hope to understand the inherent physics in the disk and planet formation processes. The software tools I have been developing take us a step closer to being able to consistently make fits and measurements to e.g. the entire known sample of debris or protoplanetary disks.

The Gemini Planet Imager serves as a stepping stone for future endeavors. Using similar techniques employed in GPI, extreme adaptive optics (AO) systems on 30-meter class telescopes (Ex. TMT) and longer timescale AO systems on future space telescopes (Ex. AFTA/WFIRST and proposed future flagships such as HabEx or LUVOIR) will not only enable the direct imaging of earth like planets, but widen the possibilities for ground and space based observing of all astronomical sources. More immediately, the James Webb Space Telescope will soon provide advances in

contrast performance (the superb PSF stability in space allows for higher contrast via PSF subtraction techniques), and resolved images at infrared wavelengths that are very difficult to achieve from the ground. The Hubble Space Telescope recently had its 27th anniversary, and the technology that flew with Hubble (including coronagraphs, though there have been some updates with servicing missions) is no longer the state-of-the-art. With the launch of JWST in 2018, the community profits from the increased collecting area, a wavelength coverage extending farther into the Infrared and the improved technology of the instruments on board. While HST flew with only standard Lyot coronagraphs, JWST will fly with three different types of coronographs including a Lyot coronagraph on the Mid-IR Instrument, a set of Band Limited Lyot Coronagraphs on NIRCam and a set of Four Quadrant Phase masks on MIRI. The most notable difference between HST and JWST is the wavelength coverage. This will allow us to prove the thermal structure of the several micron sized grains in the disk and provide information on the disk chemistry. JWST can achieve higher contrast and comparable inner working angles at longer wavelenths as compared to HST due to the larger aperture and consequently longer baselines.

The era of HST and ground based 8-meter class Extreme AO systems saw some incredible developments in our ability not only to image disks and planets around nearby stars, but also in our understanding of the physical processes inherent in the planet formation process. As instrumental capabilities improve, and sample sizes become larger, we are able to identify finer detailed features within disks, and compare

these to ever more complex simulations of the dynamics of gas and dust and of exoplanet atmospheres. Looking ahead, the highly anticipated era of JWST and 30-m class ground based Extreme AO systems will allow us to probe closer into the planet forming regions of nearby disks in scattered light, and open up a new frontier of well-resolved infrared images of disks viewed in thermal emission.

Bibliography

Akeson, R. L., & Jensen, E. L. N. 2014, ApJ, 784, 62

Alcalá, J. M., Natta, A., Manara, C. F., et al. 2014, A&A, 561, A2

Andrews, S. M., Rosenfeld, K. A., Kraus, A. L., & Wilner, D. J. 2013, ApJ, 771, 129

Andrews, S. M., & Williams, J. P. 2007, ApJ, 659, 705

Ansdell, M., Williams, J. P., van der Marel, N., et al. 2016, ApJ, 828, 46

Armitage, P. J., Clarke, C. J., & Tout, C. A. 1999, MNRAS, 304, 425

Bailey, V., Meshkat, T., Reiter, M., et al. 2014, ApJL, 780, L4

Bally, J., Walawender, J., Luhman, K. L., & Fazio, G. 2006, AJ, 132, 1923

Baraffe, I., Chabrier, G., Allard, F., & Hauschildt, P. H. 1998, A&A, 337, 403

Baraffe, I., Chabrier, G., Barman, T. S., Allard, F., & Hauschildt, P. H. 2003, A&A, 402, 701

Bate, M. R. 2009, MNRAS, 392, 590

—. 2011, MNRAS, 418, 703

Beckwith, S. V. W., Sargent, A. I., Chini, R. S., & Guesten, R. 1990, AJ, 99, 924

Belloche, A., Schuller, F., Parise, B., et al. 2011, A&A, 527, A145

Bertout, C., Basri, G., & Bouvier, J. 1988, ApJ, 330, 350

Bertout, C., Robichon, N., & Arenou, F. 1999, A&A, 352, 574

Bertout, C., Siess, L., & Cabrit, S. 2007, A&A, 473, L21

Biller, B. A., Males, J., Rodigas, T., et al. 2014, ApJL, 792, L22

Bonnefoy, M., Chauvin, G., Lagrange, A.-M., et al. 2014, A&A, 562, A127

Bonnet, H., Conzelmann, R., Delabre, B., et al. 2004, in Proc. SPIE, Vol. 5490, Advancements in Adaptive Optics, ed. D. Bonaccini Calia, B. L. Ellerbroek, & R. Ragazzoni, 130–138

Boss, A. P. 1997, Science, 276, 1836

—. 2011, ApJ, 731, 74

Boulanger, F., Bronfman, L., Dame, T. M., & Thaddeus, P. 1998, A&A, 332, 273

Bouwman, J., Henning, T., Hillenbrand, L. A., et al. 2008, ApJ, 683, 479

Bowler, B. P., Andrews, S. M., Kraus, A. L., et al. 2015, ApJL, 805, L17

BIBLIOGRAPHY

Bowler, B. P., Liu, M. C., Kraus, A. L., Mann, A. W., & Ireland, M. J. 2011, ApJ, 743, 148

Bryan, M. L., Bowler, B. P., Knutson, H. A., et al. 2016, ApJ, 827, 100

Burrows, C. J., Stapelfeldt, K. R., Watson, A. M., et al. 1996, ApJ, 473, 437

Caceres, C., Hardy, A., Schreiber, M. R., et al. 2015, ApJL, 806, L22

Cambresy, L., Epchtein, N., Copet, E., et al. 1997, A&A, 324, L5

Canovas, H., Ménard, F., de Boer, J., et al. 2015, A&A, 582, L7

Carmona, A., Pinte, C., Thi, W. F., et al. 2014, A&A, 567, A51

Carpenter, J. M., Wolf, S., Schreyer, K., Launhardt, R., & Henning, T. 2005, AJ, 129, 1049

Chabrier, G., Baraffe, I., Allard, F., & Hauschildt, P. 2000, ApJ, 542, 464

Chiang, E., & Choi, H. 2008, AJ, 136, 350

Chiang, E. I., & Goldreich, P. 1997, ApJ, 490, 368

Chiang, E. I., Joung, M. K., Creech-Eakman, M. J., et al. 2001, ApJ, 547, 1077

Chiang, H.-F., Looney, L. W., & Tobin, J. J. 2012, ApJ, 756, 168

Chilcote, J., Barman, T., Fitzgerald, M. P., et al. 2015, ApJL, 798, L3

Chilcote, J., Pueyo, L., De Rosa, R. J., et al. 2017, AJ, 153, 182

BIBLIOGRAPHY

Chilcote, J. K., Larkin, J. E., Planet Imager instrument, G., & science Teams. 2014, in American Astronomical Society Meeting Abstracts, Vol. 223, American Astronomical Society Meeting Abstracts, 202.04

Cleeves, L. I., Öberg, K. I., Wilner, D. J., et al. 2016, ApJ, 832, 110

Comerón, F., Reipurth, B., Henry, A., & Fernández, M. 2004, A&A, 417, 583

Cortes, S. R., Meyer, M. R., Carpenter, J. M., et al. 2009, ApJ, 697, 1305

Cotera, A. S., Whitney, B. A., Young, E., et al. 2001, ApJ, 556, 958

Crossfield, I. J. M. 2015, PASP, 127, 941

Czekala, I., Andrews, S. M., Mandel, K. S., Hogg, D. W., & Green, G. M. 2015, ApJ, 812, 128

Dai, Y., Wilner, D. J., Andrews, S. M., & Ohashi, N. 2010, AJ, 139, 626

D'Alessio, P., Calvet, N., Hartmann, L., Franco-Hernández, R., & Servín, H. 2006, ApJ, 638, 314

D'Alessio, P., Calvet, N., Hartmann, L., Lizano, S., & Cantó, J. 1999, ApJ, 527, 893

David, T. J., Hillenbrand, L. A., Cody, A. M., Carpenter, J. M., & Howard, A. W. 2016, ApJ, 816, 21

De Rosa, R. J., Rameau, J., Patience, J., et al. 2016, ApJ, 824, 121

BIBLIOGRAPHY

Debes, J. H., Jang-Condell, H., Weinberger, A. J., Roberge, A., & Schneider, G. 2013, ApJ, 771, 45

Dong, R. 2015, ApJ, 810, 6

Dong, R., Zhu, Z., & Whitney, B. 2015, ApJ, 809, 93

Dorschner, J., Begemann, B., Henning, T., Jaeger, C., & Mutschke, H. 1995, A&A, 300, 503

Draper, Zachary H., & the GPI Team. 2014, in SPIE **these proceedings**

Duchêne, G., Ménard, F., Stapelfeldt, K., & Duvert, G. 2003, A&A, 400, 559

Duchêne, G., McCabe, C., Pinte, C., et al. 2010, ApJ, 712, 112

Dullemond, C. P., & Dominik, C. 2004, A&A, 421, 1075

—. 2005, A&A, 434, 971

Dunham, M. M., Offner, S. S. R., Pineda, J. E., et al. 2016, ApJ, 823, 160

Eisenhauer, F., Abuter, R., Bickert, K., et al. 2003, in Proc. SPIE, Vol. 4841, Instrument Design and Performance for Optical/Infrared Ground-based Telescopes, ed. M. Iye & A. F. M. Moorwood, 1548–1561

Espaillat, C., Furlan, E., D'Alessio, P., et al. 2011, ApJ, 728, 49

Espaillat, C., D'Alessio, P., Hernández, J., et al. 2010, ApJ, 717, 441

BIBLIOGRAPHY

Esposito, T. M., Fitzgerald, M. P., Graham, J. R., et al. 2016, AJ, 152, 85

Fitzgibbon, A. W., P. M., & B., F. R. 1996, in

Flaherty, K. M., Muzerolle, J., Rieke, G., et al. 2012, ApJ, 748, 71

Foreman-Mackey, D., Hogg, D. W., Lang, D., & Goodman, J. 2013, PASP, 125, 306

Garaud, P., Barrière-Fouchet, L., & Lin, D. N. C. 2004, ApJ, 603, 292

Glauser, A. M., Ménard, F., Pinte, C., et al. 2008, A&A, 485, 531

Goldsmith, P. F. 1987, in Astrophysics and Space Science Library, Vol. 134, Interstellar Processes, ed. D. J. Hollenbach & H. A. Thronson, Jr., 51–70

Goodman, J., & Weare, J. 2010, Comm. App. Math. Comp. Sci., 5, 65

Graham, J. R., Kalas, P. G., & Matthews, B. C. 2007, ApJ, 654, 595

Greenbaum, A. Z., Cheetham, A., Sivaramakrishnan, A., et al. 2014, in Proc. SPIE, Vol. 9147, Ground-based and Airborne Instrumentation for Astronomy V, 91477B

Gregorio-Hetem, J., Lepine, J. R. D., Quast, G. R., Torres, C. A. O., & de La Reza, R. 1992, AJ, 103, 549

Guilloteau, S., Dutrey, A., Piétu, V., & Boehler, Y. 2011, A&A, 529, A105

Haisch, Jr., K. E., Lada, E. A., & Lada, C. J. 2001, ApJL, 553, L153

Harris, R. J., Andrews, S. M., Wilner, D. J., & Kraus, A. L. 2012, ApJ, 751, 115

BIBLIOGRAPHY

Hartmann, L., Calvet, N., Gullbring, E., & D'Alessio, P. 1998, ApJ, 495, 385

Heng, K., & Kenyon, S. J. 2010, MNRAS, 408, 1476

Herbig, G. H. 1977, ApJ, 214, 747

Herczeg, G. J., Cruz, K. L., & Hillenbrand, L. A. 2009, ApJ, 696, 1589

Huélamo, N., Bouy, H., Pinte, C., et al. 2010, A&A, 523, A42

Hughes, A. M., Wilner, D. J., Qi, C., & Hogerheijde, M. R. 2008, ApJ, 678, 1119

Hung, L.-W., Duchêne, G., Arriaga, P., et al. 2015, ApJL, 815, L14

Ingleby, L., Calvet, N., Herczeg, G., et al. 2013, ApJ, 767, 112

Ingraham, P., Ruffio, J.-B., Perrin, M. D., et al. 2014a, in Proc. SPIE, Vol. 9147, Ground-based and Airborne Instrumentation for Astronomy V, 91477K

Ingraham, P., Marley, M. S., Saumon, D., et al. 2014b, ApJL, 794, L15

Ireland, M. J., Kraus, A., Martinache, F., Law, N., & Hillenbrand, L. A. 2011, ApJ, 726, 113

Isella, A., Carpenter, J. M., & Sargent, A. I. 2010, ApJ, 714, 1746

Itoh, Y., Hayashi, M., Tamura, M., et al. 2005, ApJ, 620, 984

James E. Larkin, Jeffrey K. Chilcote, Theodore Aliado, et al. 2014, in

Jang-Condell, H. 2009, ApJ, 700, 820

Joergens, V., Bonnefoy, M., Liu, Y., et al. 2013, A&A, 558, L7

Kalas, P. G., Rajan, A., Wang, J. J., et al. 2015, ApJ, 814, 32

Kant, I. 1755, Allgemeine Naturgeschichte und Theorie des Himmels

Kastner, J. H., Hily-Blant, P., Sacco, G. G., Forveille, T., & Zuckerman, B. 2010, ApJL, 723, L248

Kenyon, S. J., & Hartmann, L. 1987, ApJ, 323, 714

Kenyon, S. J., Yi, I., & Hartmann, L. 1996, ApJ, 462, 439

Kratter, K. M., Murray-Clay, R. A., & Youdin, A. N. 2010, ApJ, 710, 1375

Kraus, A. L., Andrews, S. M., Bowler, B. P., et al. 2015, ApJL, 798, L23

Kraus, A. L., & Ireland, M. J. 2012, ApJ, 745, 5

Krist, J. 1995, in Astronomical Society of the Pacific Conference Series, Vol. 77, Astronomical Data Analysis Software and Systems IV, ed. R. A. Shaw, H. E. Payne, & J. J. E. Hayes, 349

Lafrenière, D., Jayawardhana, R., & van Kerkwijk, M. H. 2008, ApJL, 689, L153

Lagage, P.-O., Doucet, C., Pantin, E., et al. 2006, Science, 314, 621

Larkin, J. E., Chilcote, J. K., Aliado, T., et al. 2014, in Proc. SPIE, Vol. 9147, Ground-based and Airborne Instrumentation for Astronomy V, 91471K

BIBLIOGRAPHY

Lebreton, J., Augereau, J.-C., Thi, W.-F., et al. 2012, A&A, 539, A17

Levenberg, K. 1963, The Quarterly of Applied Mathematics, 2, 164

Lissauer, J. J., & Stevenson, D. J. 2007, Protostars and Planets V, 591

Lombardi, M., Lada, C. J., & Alves, J. 2008, A&A, 489, 143

Long, F., Herczeg, G. J., Pascucci, I., et al. 2017, ArXiv e-prints, arXiv:1706.03320

Low, C., & Lynden-Bell, D. 1976, MNRAS, 176, 367

Luhman, K. L. 2007, ApJS, 173, 104

Luhman, K. L., Wilson, J. C., Brandner, W., et al. 2006, ApJ, 649, 894

Luhman, K. L., Allen, L. E., Allen, P. R., et al. 2008, ApJ, 675, 1375

MacGregor, M. A., Wilner, D. J., Czekala, I., et al. 2017, ApJ, 835, 17

Macintosh, B., Gemini Planet Imager instrument Team, Planet Imager Exoplanet Survey, G., & Observatory, G. 2014a, in American Astronomical Society Meeting Abstracts, Vol. 223, American Astronomical Society Meeting Abstracts, 229.02

Macintosh, B., Graham, J., Palmer, D., et al. 2006, in Proc. SPIE, Vol. 6272, Society of Photo-Optical Instrumentation Engineers (SPIE) Conference Series, 62720L

Macintosh, B., Graham, J. R., Ingraham, P., et al. 2014b, ArXiv e-prints, arXiv:1403.7520

—. 2014c, Proceedings of the National Academy of Science, 111, 12661

Macintosh, B., Graham, J. R., Barman, T., et al. 2015, Science, 350, 64

Madlener, D., Wolf, S., Dutrey, A., & Guilloteau, S. 2012, A&A, 543, A81

Maire, J., Perrin, M. D., Doyon, R., et al. 2012, in Society of Photo-Optical Instrumentation Engineers (SPIE) Conference Series, Vol. 8451, Society of Photo-Optical Instrumentation Engineers (SPIE) Conference Series

Maire, Jérôme, & the GPI Team. 2014, in SPIE **these proceedings**

Mamajek, E. E., Meyer, M. R., & Liebert, J. 2002, AJ, 124, 1670

Manara, C. F., Testi, L., Natta, A., & Alcalá, J. M. 2015, A&A, 579, A66

Manara, C. F., Testi, L., Herczeg, G. J., et al. 2017, ArXiv e-prints, arXiv:1704.02842

Marquardt, D. 1944, Journal of the Society for Industrial and Applied Mathematics, 11, 431

McBride, J., Graham, J. R., Macintosh, B., et al. 2011, PASP, 123, 692

McCabe, C., Duchêne, G., Pinte, C., et al. 2011, ApJ, 727, 90

Millar-Blanchaer, M. A., Graham, J. R., Pueyo, L., et al. 2015, ApJ, 811, 18

Milli, J., Mawet, D., Pinte, C., et al. 2015, A&A, 577, A57

Murakawa, K. 2010, A&A, 518, A63

Murphy, S. J., Lawson, W. A., & Bessell, M. S. 2013, MNRAS, 435, 1325

Muzerolle, J., Flaherty, K., Balog, Z., et al. 2009, ApJL, 704, L15

Neuhäuser, R., Guenther, E. W., Wuchterl, G., et al. 2005, A&A, 435, L13

Nielsen, E. L., & Close, L. M. 2010, ApJ, 717, 878

Nielsen, E. L., Close, L. M., Biller, B. A., Masciadri, E., & Lenzen, R. 2008, ApJ, 674, 466

Nielsen, E. L., Liu, M. C., Wahhaj, Z., et al. 2016, in IAU Symposium, Vol. 314, Young Stars Planets Near the Sun, ed. J. H. Kastner, B. Stelzer, & S. A. Metchev, 220–225

Olofsson, J., Samland, M., Avenhaus, H., et al. 2016, A&A, 591, A108

Ossenkopf, V., & Henning, T. 1994, A&A, 291, 943

Papaloizou, J., & Pringle, J. E. 1977, MNRAS, 181, 441

Pascucci, I., Hollenbach, D., Najita, J., et al. 2007, ApJ, 663, 383

Pascucci, I., Testi, L., Herczeg, G. J., et al. 2016, ApJ, 831, 125

Patience, J., King, R. R., De Rosa, R. J., et al. 2012, A&A, 540, A85

Perrin, M. D., Gemini Planet Imager instrument, T., & science Teams. 2014a, in American Astronomical Society Meeting Abstracts, Vol. 223, American Astronomical Society Meeting Abstracts, 348.14

Perrin, M. D., Maire, J., Ingraham, P., et al. 2014b, in Proc. SPIE, Vol. 9147, Ground-based and Airborne Instrumentation for Astronomy V, 91473J

Perrin, M. D., Maire, J., Ingraham, P., et al. 2014c, in Proc. SPIE, Vol. 9147, Ground-based and Airborne Instrumentation for Astronomy V, 91473J

Perrin, M. D., Duchene, G., Millar-Blanchaer, M., et al. 2015, ApJ, 799, 182

Pinte, C., Dent, W. R. F., Ménard, F., et al. 2016, ApJ, 816, 25

Pinte, C., Harries, T. J., Min, M., et al. 2009, A&A, 498, 967

Pinte, C., Ménard, F., Duchêne, G., & Bastien, P. 2006, A&A, 459, 797

Pinte, C., Padgett, D. L., Ménard, F., et al. 2008, A&A, 489, 633

Pohl, A., Sissa, E., Langlois, M., et al. 2017, ArXiv e-prints, arXiv:1705.03477

Poyneer, L. A., De Rosa, R. J., Macintosh, B., et al. 2014, in Proc. SPIE, Vol. 9148, Adaptive Optics Systems IV, 91480K

Quanz, S. P., Amara, A., Meyer, M. R., et al. 2015, ApJ, 807, 64

Raftery, A., & Lewis, S. 1992, Bayesian Statistics, 4, 763

Rajan, A., Rameau, J., De Rosa, R. J., et al. 2017, AJ, 154, 10

Ramsay Howat, S. K., Harris, J. W., & Bennett, R. J. 1997, in Society of Photo-Optical Instrumentation Engineers (SPIE) Conference Series, Vol. 2871, Optical Telescopes of Today and Tomorrow, ed. A. L. Ardeberg, 1171–1178

Rapson, V. A., Kastner, J. H., Andrews, S. M., et al. 2015a, ApJL, 803, L10

Rapson, V. A., Kastner, J. H., Millar-Blanchaer, M. A., & Dong, R. 2015b, ApJL, 815, L26

Reggiani, M., Quanz, S. P., Meyer, M. R., et al. 2014, ApJL, 792, L23

Ribas, Á., Bouy, H., Merín, B., et al. 2016, MNRAS, 458, 1029

Ricci, L., Carpenter, J. M., Fu, B., et al. 2015, ApJ, 798, 124

Robberto, M., Spina, L., Da Rio, N., et al. 2012, AJ, 144, 83

Robitaille, T. P., Whitney, B. A., Indebetouw, R., Wood, K., & Denzmore, P. 2006, ApJS, 167, 256

Rodgers-Lee, D., Scholz, A., Natta, A., & Ray, T. 2014, MNRAS, 443, 1587

Sallum, S., Follette, K. B., Eisner, J. A., et al. 2015, Nature, 527, 342

Sauter, J., Wolf, S., Launhardt, R., et al. 2009, A&A, 505, 1167

Schaefer, G. H., Dutrey, A., Guilloteau, S., Simon, M., & White, R. J. 2009, ApJ, 701, 698

Schmid, H. M., Joos, F., & Tschan, D. 2006, A&A, 452, 657

Schmidt, T. O. B., Neuhäuser, R., Seifahrt, A., et al. 2008, A&A, 491, 311

Schneider, G., Grady, C. A., Hines, D. C., et al. 2014, AJ, 148, 59

Schütz, O., Meeus, G., & Sterzik, M. F. 2005, A&A, 431, 165

Sembach, K. R., & Savage, B. D. 1992, ApJS, 83, 147

Sharma, S. 2017, ArXiv e-prints, arXiv:1706.01629

Sivaramakrishnan, A., Koresko, C. D., Makidon, R. B., Berkefeld, T., & Kuchner, M. J. 2001, ApJ, 552, 397

Sivaramakrishnan, A., & Oppenheimer, B. R. 2006, ApJ, 647, 620

Smith, B. A., & Terrile, R. J. 1984, Science, 226, 1421

Soummer, R., Pueyo, L., & Larkin, J. 2012, ApJL, 755, L28

Soummer, R., Sivaramakrishnan, A., Oppenheimer, B. R., et al. 2009, in Proc. SPIE, Vol. 7440, Techniques and Instrumentation for Detection of Exoplanets IV, 74400R

Sousa, A. P., Alencar, S. H. P., Bouvier, J., et al. 2016, A&A, 586, A47

Stapelfeldt, K. 2004, in IAU Symposium, Vol. 202, Planetary Systems in the Universe, ed. A. Penny, 291

Stapelfeldt, K. R., Duchêne, G., Perrin, M., et al. 2014, in IAU Symposium, Vol. 299, Exploring the Formation and Evolution of Planetary Systems, ed. M. Booth, B. C. Matthews, & J. R. Graham, 99–103

Steinacker, J., Baes, M., & Gordon, K. D. 2013, ARA&A, 51, 63

Torres, C. A. O., Quast, G. R., Melo, C. H. F., & Sterzik, M. F. 2008, Young Nearby Loose Associations, 757

van der Plas, G., Ménard, F., Ward-Duong, K., et al. 2016, ApJ, 819, 102

Venuti, L., Bouvier, J., Irwin, J., et al. 2015, A&A, 581, A66

Vorobyov, E. I. 2013, A&A, 552, A129

Wang, J. J., Ruffio, J.-B., De Rosa, R. J., et al. 2015a, pyKLIP: PSF Subtraction for Exoplanets and Disks, Astrophysics Source Code Library, ascl:1506.001

Wang, J. J., Rajan, A., Graham, J. R., et al. 2014, in Proc. SPIE, Vol. 9147, Ground-based and Airborne Instrumentation for Astronomy V, 914755

Wang, J. J., Graham, J. R., Pueyo, L., et al. 2015b, ApJL, 811, L19

Ward, W. R., & Canup, R. M. 2010, AJ, 140, 1168

Watson, A. M., Stapelfeldt, K. R., Wood, K., & Ménard, F. 2007, Protostars and Planets V, 523

Weidenschilling, S. J. 1977, Ap&SS, 51, 153

Whitney, B. A., Indebetouw, R., Bjorkman, J. E., & Wood, K. 2004, ApJ, 617, 1177

Whitney, B. A., Wood, K., Bjorkman, J. E., & Cohen, M. 2003a, ApJ, 598, 1079

Whitney, B. A., Wood, K., Bjorkman, J. E., & Wolff, M. J. 2003b, ApJ, 591, 1049

Whittet, D. C. B., Prusti, T., Franco, G. A. P., et al. 1997, A&A, 327, 1194

Williams, J. P., & Cieza, L. A. 2011, ARA&A, 49, 67

Winston, E., Cox, N. L. J., Prusti, T., et al. 2012, A&A, 545, A145

Woitke, P. 2015, in European Physical Journal Web of Conferences, Vol. 102, European Physical Journal Web of Conferences, 00007

Woitke, P., Pinte, C., Tilling, I., et al. 2010, MNRAS, 405, L26

Wolf, S., Padgett, D. L., & Stapelfeldt, K. R. 2003, ApJ, 588, 373

Wolff, S. G., Perrin, M. D., Maire, J., et al. 2014, in Proc. SPIE, Vol. 9147, Ground-based and Airborne Instrumentation for Astronomy V, 91477H

Wolff, S. G., Ward-Duong, K., Zalesky, J., et al. 2016a, in Proc. SPIE, Vol. 9908, Ground-based and Airborne Instrumentation for Astronomy VI, 990838

Wolff, S. G., Perrin, M., Millar-Blanchaer, M. A., et al. 2016b, ApJL, 818, L15

Wolff, S. G., Ménard, F., Caceres, C., et al. 2017, AJ, 154, 26

Wood, K., Whitney, B. A., Robitaille, T., & Draine, B. T. 2008, ApJ, 688, 1118

Wu, Y.-L., Sheehan, P. D., Males, J. R., et al. 2017, ApJ, 836, 223

Zhang, K., Blake, G. A., & Bergin, E. A. 2015, ApJL, 806, L7

BIBLIOGRAPHY

Zhou, Y., Herczeg, G. J., Kraus, A. L., Metchev, S., & Cruz, K. L. 2014, ApJL, 783, L17

Vita

Starting in October 2017, Schuyler will begin her tenure as the Oort Postdoctoral Fellow at the Leiden Observatory. There she plans to continue her work on the radiative transfer modeling of multi-wavelength observations of circumstellar disks at all evolutionary stages.

Education

The Johns Hopkins University

M.A., Physics and Astronomy, 2013.

Ph.D., Physics and Astronomy, expected 2017.

Thesis: *Characterizing the Evolution of Circumstellar Systems with the Hubble Space Telescope and the Gemini Planet Imager*

Graduate Research Advisor: Marshall Perrin, Space Telescope Science Institute

Graduate Thesis Advisor: Holland Ford, The Johns Hopkins University

Western Kentucky University

B.S., Physics and Astronomy, 2011.

Honors Thesis: *Examining Type Ia Supernova Progenitors from Local Event Rates*

Thesis Advisor: Louis-Gregory Strolger

Teaching

The Johns Hopkins University

Teaching Assistant, General Physics I, 2011

Teaching Assistant, General Physics II, 2012

Western Kentucky University

Teaching Assistant, Astronomy 275: Astronomy Research Methods, 2010

Teaching Assistant, Astronomy 298: Research Experiences, 2011

Awards and Fellowships

National Science Foundation Graduate Research Fellowship

The Johns Hopkins University, 2013-2016

Chambliss Astronomy Achievement Award

229th AAS Meeting, 2017

NSF Graduate Research Opportunities Worldwide Fellowship

Grenoble, France, 2016

Honors Capstone Experience/Thesis of the Year

Western Kentucky University, 2011

Dr. Douglas Humphrey Award for Outstanding Service

Department of Physics and Astronomy, Western Kentucky University, 2011

Randall Harper Award for Outstanding Research

Department of Physics and Astronomy, Western Kentucky University, 2010

Kentucky Space Grant Consortium Scholarship

Western Kentucky University, 2010

Smithsonian Astrophysical Observatory REU Internship

Cambridge, MA, 2010

DAAD Rise Internship

Göttingen, Germany, 2009

Technical Skills: Python, IDL, LaTeX, SQL, Machining Training

Professional Development

- Attended the Center for Adaptive Optics AO Summer School. 2012
- Attended the SciCoder Summer School. 2013
- Attended the Sagan Exoplanet Workshop on *Imaging Planets and Disks*. 2014
- Attended the Sagan Exoplanet Workshop on *Exoplanetary System Demographics: Theory and Observations*. 2015

Professional Memberships

- Junior Member of the American Astronomical Society 2010 - Present
- Member of SPIE, the International Society for Optics and Photonics, 2014 - Present

Open Source Software Projects

- The Gemini Planet Imager Data Reduction Pipeline:
  <http://docs.planetimager.org/pipeline/>
- Python MCFOST MCMC disk fitting toolkit:
  <https://github.com/swolff9/mcfost-python>

Outreach Activities

Member of the Steering Committee for the JHU Physics and Astronomy Diversity Group:

We have developed a mentorship system to encourage women and minorities to remain in physics and astronomy beginning in the Undergraduate level. We hold bi-semester, department wide meetings to raise awareness about issues facing under-represented groups.

Member of the JHU Physics and Astronomy Graduate Student Outreach Group:

We conduct visits once a month to a local Baltimore Charter School, providing demonstrations and instruction in physics. We have also partnered with World Wide Telescope to built a portable planetarium and provide educational shows for the community.

Member of the Gemini Planet Imager Exoplanet Survey Committee on Harassment Prevention:

The duties of the committee include defining and maintaining the GPIES anti-harassment policy, providing a comprehensive list of resources regarding harassment and anti-discrimination, and defining protocol for reporting harassment to the proper institution.

Publications (5 first author publications, 45 total publications.)

Wolff, S., Perrin, M., Stapelfeldt, G. Duchêne, J. Krist, F. Ménard, D. Padgett C. Pinte, & L. Pueyo. "HST Scattered Light Imaging and Modeling of the Edge-on Protoplanetary Disk ESO-Hα 569."

Wolff, S., Perrin, M., Stapelfeldt, G. Duchêne, J. Krist, F. Ménard, D. Padgett C. Pinte, & L. Pueyo. "Improved Methods for Parameter Inference for Circumstellar Disk Modeling." Submitted for publication in ApJ.

Wolff, S., Ménard, F., Caceres, C., & Lefèvre, C. "An Upper Limit on the Mass of the Circumplanetary Disk for DH Tau b." Accepted for publication in AJ.

Wolff, S. G., K. Ward-Duong, J. Zalesky, A. Z. Greenbaum, M. D. Perrin, and J. Graham 2016. "Gemini Planet Imager Observational Calibration XIII: Wavelength Calibration Improvements, Stability, and Nonlinearity." Proc. SPIE 9908, 990838.

Wolff, S. G., M. Perrin, M. A. Millar-Blanchaer, E. L. Nielsen, J. Wang, A. Cardwell, J. Chilcote, R. Dong, Z. H. Draper, G. Duchêne, M. P. Fitzgerald, S. J. Goodsell, C. A. Grady, J. R. Graham, A. Z. Greenbaum, M. Hartung, P. Hibon, D. C. Hines, L.-W. Hung, P. Kalas, B. Macintosh, F. Marchis, C. Marois, L. Pueyo, F. T. Rantakyrö, G. Schneider, A. Sivaramakrishnan, and S. J. Wiktorowicz 2016. "The PDS 66 Circumstellar Disk as Seen in Polarized Light with the Gemini Planet Imager." ApJL 818, L15.

Wolff, S. G., M. D. Perrin, J. Maire, P. J. Ingraham, F. T. Rantakyrö, and P. Hibon 2014. "Gemini planet imager observational calibrations IV: wavelength calibration and flexure correction for the integral field spectograph." Proc. SPIE 9147, 91477H.

Wolff, S., M. Perrin, K. Stapelfeldt, G. Duchêne, J. Krist, F. Ménard, D. Padgett, and C. Pinte 2014. "Resolved Scattered Light Images of the Edge-On Protoplanetary Disk ESO Hα 569." Exploring the Formation and Evolution of Planetary Systems 299, 76-77.

Wolff, S., R. I. Dawson, and R. A. Murray-Clay 2012. "Neptune on Tiptoes: Dynamical Histories that Preserve the Cold Classical Kuiper Belt." ApJ 746, 171.

Choquet, É., Milli, J., Wahhaj, Z., Soummer, R., Roberge, A., Augereau, J.-C., Booth, M., Absil, O., Boccaletti, A., Chen, C. H., Debes, J. H., del Burgo, C., Dent, W. R. F., Ertel, S., Girard, J. H., Gofas-Salas, E., Golimowski, D. A., Gómez González, C. A., Brendan Hagan, J., Hibon, P., Hines, D. C., Kennedy, G. M., Lagrange, A.-M., Matrà, L., Mawet, D., Mouillet, D., N'Diaye, M., Perrin, M. D., Pinte, C., Pueyo, L., Rajan, A., Schneider, G., **Wolff, S.**, and Wyatt, M. 2017. "First Scattered-light Images of the Gas-rich Debris Disk around 49 Ceti." ApJL, 834, L12

Rameau, J., Follette, K. B., Pueyo, L., Marois, C., Macintosh, B., Millar-Blanchaer, M., Wang, J. J., Vega, D., Doyon, R., Lafrenière, D., Nielsen, E. L., Bailey, V., Chilcote, J. K., Close, L. M., Esposito, T. M., Males, J. R., Metchev, S., Morzinski, K. M., Ruffio, J.-B., **Wolff, S. G.**, Ammons, S. M., Barman, T. S., Bulger, J., Cotten, T., De Rosa, R. J., Duchene, G., Fitzgerald, M. P., Goodsell, S., Graham, J. R., Greenbaum, A. Z., Hibon, P., Hung, L.-W., Ingraham, P., Kalas, P., Konopacky, Q., Larkin, J. E., Maire, J., Marchis, F., Oppenheimer, R., Palmer, D., Patience, J., Perrin, M. D., Poyneer, L., Rajan, A., Rantakyrö, F. T., Marley, M. S., Savransky, D., Schneider, A. C., Sivaramakrishnan, A., Song, I., Soummer, R., Thomas, S., Wallace, J. K., Ward-Duong, K., and Wiktorowicz, S. 2017. "An Optical/Near-infrared Investigation of HD 100546 b with the Gemini Planet Imager and MagAO." AJ, 153, 244

Rajan, A., Rameau, J., De Rosa, R. J., Marley, M. S., Graham, J. R., Macintosh, B., Marois, C., Morley, C., Patience, J., Pueyo, L., Saumon, D., Ward-Duong, K., Ammons, S. M., Arriaga, P., Bailey, V. P., Barman, T., Bulger, J., Burrows, A. S., Chilcote, J., Cotten, T., Czekala, I., Doyon, R., Duchêne, G., Esposito,

T. M., Fitzgerald, M. P., Follette, K. B., Fortney, J. J., Goodsell, S. J., Greenbaum, A. Z., Hibon, P., Hung, L.-W., Ingraham, P., Johnson-Groh, M., Kalas, P., Konopacky, Q., Lafrenière, D., Larkin, J. E., Maire, J., Marchis, F., Metchev, S., Millar-Blanchaer, M. A., Morzinski, K. M., Nielsen, E. L., Oppenheimer, R., Palmer, D., Patel, R. I., Perrin, M., Poyneer, L., Rantakyrö, F. T., Ruffio, J.-B., Savransky, D., Schneider, A. C., Sivaramakrishnan, A., Song, I., Soummer, R., Thomas, S., Vasisht, G., Wallace, J. K., Wang, J. J., Wiktorowicz, S., and **Wolff, S.** 2017. "Characterizing 51 Eri b from 1-5 μm: a partly-cloudy exoplanet." arXiv:1705.03887

Follette, K. B., Rameau, J., Dong, R., Pueyo, L., Close, L. M., Duchene, G., Fung, J., Leonard, C., Macintosh, B., Males, J. R., Marois, C., Millar-Blanchaer, M. A., Morzinski, K. M., Mullen, W., Perrin, M., Spiro, E., Wang, J., Ammons, S. M., Bailey, V. P., Barman, T., Bulger, J., Chilcote, J., Cotten, T., De Rosa, R. J., Doyon, R., Fitzgerald, M. P., Goodsell, S. J., Graham, J. R., Greenbaum, A. Z., Hibon, P., Hung, L.-W., Ingraham, P., Kalas, P., Konopacky, Q., Larkin, J. E., Maire, J., Marchis, F., Metchev, S., Nielsen, E. L., Oppenheimer, R., Palmer, D., Patience, J., Poyneer, L., Rajan, A., Rantakyro, F. T., Savransky, D., Schneider, A. C., Sivaramakrishnan, A., Song, I., Soummer, R., Thomas, S., Vega, D., Wallace, J. K., Ward-Duong, K., Wiktorowicz, S., and **Wolff, S.** 2017. "Complex Spiral Structure in the HD 100546 Transitional Disk as Revealed by GPI and MagAO." arXiv:1704.06260

Chilcote, J., Pueyo, L., De Rosa, R. J., Vargas, J., Macintosh, B., Bailey, V. P., Barman, T., Bauman, B., Bruzzone, S., Bulger, J., Burrows, A. S., Cardwell, A., Chen, C. H., Cotten, T., Dillon, D., Doyon, R., Draper, Z. H., Duchêne, G., Dunn, J., Erikson, D., Fitzgerald, M. P., Follette, K. B., Gavel, D., Goodsell, S. J., Graham, J. R., Greenbaum, A. Z., Hartung, M., Hibon, P., Hung, L.-W., Ingraham, P., Kalas, P., Konopacky, Q., Larkin, J. E., Maire, J., Marchis, F., Marley, M. S., Marois, C., Metchev, S., Millar-Blanchaer, M. A., Morzinski, K. M., Nielsen, E. L., Norton, A., Oppenheimer, R., Palmer, D., Patience, J., Perrin, M., Poyneer, L., Rajan, A., Rameau, J., Rantakyrö, F. T., Sadakuni, N., Saddlemyer, L., Savransky, D., Schneider, A. C., Serio, A., Sivaramakrishnan, A., Song, I., Soummer, R., Thomas, S., Wallace, J. K., Wang, J. J., Ward-Duong, K., Wiktorowicz, S., and **Wolff, S.** 2017. "1-2.4 & μm Near-IR Spectrum of the Giant Planet & beta; Pictoris b Obtained with the Gemini Planet Imager." AJ,

153, 182

Nielsen, E. L., De Rosa, R. J., Wang, J., Rameau, J., Song, I., Graham, J. R., Macintosh, B., Ammons, M., Bailey, V. P., Barman, T. S., Bulger, J., Chilcote, J. K., Cotten, T., Doyon, R., Duchêne, G., Fitzgerald, M. P., Follette, K. B., Greenbaum, A. Z., Hibon, P., Hung, L.-W., Ingraham, P., Kalas, P., Konopacky, Q. M., Larkin, J. E., Maire, J., Marchis, F., Marley, M. S., Marois, C., Metchev, S., Millar-Blanchaer, M. A., Oppenheimer, R., Palmer, D. W., Patience, J., Perrin, M. D., Poyneer, L. A., Pueyo, L., Rajan, A., Rantakyrö, F. T., Savransky, D., Schneider, A. C., Sivaramakrishnan, A., Soummer, R., Thomas, S., Wallace, J. K., Ward-Duong, K., Wiktorowicz, S. J., and **Wolff, S.** 2016. "Dynamical Mass Measurement of the Young Spectroscopic Binary V343 Normae AaAb Resolved With the Gemini Planet Imager." AJ, 152, 175

Millar-Blanchaer, M. A., Wang, J. J., Kalas, P., Graham, J. R., Duchêne, G., Nielsen, E. L., Perrin, M., Moon, D.-S., Padgett, D., Metchev, S., Ammons, S. M., Bailey, V. P., Barman, T., Bruzzone, S., Bulger, J., Chen, C. H., Chilcote, J., Cotten, T., De Rosa, R. J., Doyon, R., Draper, Z. H., Esposito, T. M., Fitzgerald, M. P., Follette, K. B., Gerard, B. L., Greenbaum, A. Z., Hibon, P., Hinkley, S., Hung, L.-W., Ingraham, P., Johnson-Groh, M., Konopacky, Q., Larkin, J. E., Macintosh, B., Maire, J., Marchis, F., Marley, M. S., Marois, C., Matthews, B. C., Oppenheimer, R., Palmer, D., Patience, J., Poyneer, L., Pueyo, L., Rajan, A., Rameau, J., Rantakyrö, F. T., Savransky, D., Schneider, A. C., Sivaramakrishnan, A., Song, I., Soummer, R., Thomas, S., Vega, D., Wallace, J. K., Ward-Duong, K., Wiktorowicz, S., and **Wolff, S.** 2016. "Imaging an 80 au Radius Dust Ring around the F5V Star HD 157587." AJ, 152, 128

Ruffio, J.-B., Macintosh, B., Wang, J. J., Pueyo, L., Nielsen, E. L., De Rosa, R. J., Czekala, I., Marley, M. S., Arriaga, P., Bailey, V. P., Barman, T., Bulger, J., Chilcote, J., Cotten, T., Doyon, R., Duchêne, G., Fitzgerald, M. P., Follette, K. B., Gerard, B. L., Goodsell, S. J., Graham, J. R., Greenbaum, A. Z., Hibon, P., Hung, L.-W., Ingraham, P., Kalas, P., Konopacky, Q., Larkin, J. E., Maire, J., Marchis, F., Marois, C., Metchev, S., Millar-Blanchaer, M. A., Morzinski, K. M., Oppenheimer, R., Palmer, D., Patience, J., Perrin, M., Poyneer, L., Rajan, A., Rameau, J., Rantakyrö, F. T., Savransky, D., Schneider, A. C., Sivaramakrishnan, A., Song, I., Soummer, R., Thomas, S., Wallace, J. K., Ward-Duong, K., Wiktorowicz, S., and **Wolff, S.** 2017. "Improving and Assessing Planet Sen-

sitivity of the GPI Exoplanet Survey with a Forward Model Matched Filter." arXiv:1705.05477

Nielsen, E. L., De Rosa, R. J., Rameau, J., Wang, J. J., Esposito, T. M., Millar-Blanchaer, M. A., Marois, C., Vigan, A., Ammons, S. M., Artigau, E., Bailey, V. P., Blunt, S., Bulger, J., Chilcote, J., Cotten, T., Doyon, R., Duchêne, G., Fabrycky, D., Fitzgerald, M. P., Follette, K. B., Gerard, B. L., Goodsell, S. J., Graham, J. R., Greenbaum, A. Z., Hibon, P., Hinkley, S., Hung, L.-W., Ingraham, P., Jensen-Clem, R., Kalas, P., Konopacky, Q., Larkin, J. E., Macintosh, B., Maire, J., Marchis, F., Metchev, S., Morzinski, K. M., Murray-Clay, R. A., Oppenheimer, R., Palmer, D., Patience, J., Perrin, M., Poyneer, L., Pueyo, L., Rafikov, R. R., Rajan, A., Rantakyrö, F. T., Ruffio, J.-B., Savransky, D., Schneider, A. C., Sivaramakrishnan, A., Song, I., Soummer, R., Thomas, S., Wallace, J. K., Ward-Duong, K., Wiktorowicz, S., and **Wolff, S.** 2017. "Evidence that the Directly-Imaged Planet HD 131399 Ab is a Background Star." arXiv:1705.06851

Johnson-Groh, M., Marois, C., De Rosa, R. J., Nielsen, E. L., Rameau, J., Blunt, S., Vargas, J., Ammons, S. M., Bailey, V. P., Barman, T. S., Bulger, J., Chilcote, J. K., Cotten, T., Doyon, R., Duchêne, G., Fitzgerald, M. P., Follette, K. B., Goodsell, S., Graham, J. R., Greenbaum, A. Z., Hibon, P., Hung, L.-W., Ingraham, P., Kalas, P., Konopacky, Q. M., Larkin, J. E., Macintosh, B., Maire, J., Marchis, F., Marley, M. S., Metchev, S., Millar-Blanchaer, M. A., Oppenheimer, R., Palmer, D. W., Patience, J., Perrin, M., Poyneer, L. A., Pueyo, L., Rajan, A., Rantakyrö, F. T., Savransky, D., Schneider, A. C., Sivaramakrishnan, A., Song, I., Soummer, R., Thomas, S., Vega, D., Wallace, J. K., Wang, J. J., Ward-Duong, K., Wiktorowicz, S. J., and **Wolff, S.** 2017. "Integral Field Spectroscopy of the Low-mass Companion HD 984 B with the Gemini Planet Imager." AJ, 153, 190

Millar-Blanchaer, M. A., J. J. Wang, P. Kalas, J. R. Graham, G. Duchêne, E. L. Nielsen, M. Perrin, D.-S. Moon, D. Padgett, S. Metchev, S. M. Ammons, V. P. Bailey, T. Barman, S. Bruzzone, J. Bulger, C. H. Chen, J. Chilcote, T. Cotten, R. J. De Rosa, R. Doyon, Z. H. Draper, T. M. Esposito, M. P. Fitzgerald, K. B. Follette, B. L. Gerard, A. Z. Greenbaum, P. Hibon, S. Hinkley, L.-W. Hung, P. Ingraham, M. Johnson-Groh, Q. Konopacky, J. E. Larkin, B. Macintosh, J. Maire, F. Marchis, M. S. Marley, C. Marois, B. C. Matthews, R. Oppenheimer, D. Palmer, J. Patience, L. Poyneer, L. Pueyo, A. Rajan, J. Rameau, F. T. Rantakyrö, D. Savransky, A. C. Schneider, A. Sivaramakrishnan, I. Song,

R. Soummer, S. Thomas, D. Vega, J. K. Wallace, K. Ward-Duong, S. Wiktorowicz, and **S. Wolff** 2016. "Imaging an 80 au Radius Dust Ring around the F5V Star HD 157587." AJ 152, 128.

Wang, J. J., J. R. Graham, L. Pueyo, P. Kalas, M. A. Millar-Blanchaer, J.-B. Ruffio, R. J. De Rosa, S. M. Ammons, P. Arriaga, V. P. Bailey, T. S. Barman, J. Bulger, A. S. Burrows, A. Cardwell, C. H. Chen, J. K. Chilcote, T. Cotten, M. P. Fitzgerald, K. B. Follette, R. Doyon, G. Duchêne, A. Z. Greenbaum, P. Hibon, L.-W. Hung, P. Ingraham, Q. M. Konopacky, J. E. Larkin, B. Macintosh, J. Maire, F. Marchis, M. S. Marley, C. Marois, S. Metchev, E. L. Nielsen, R. Oppenheimer, D. W. Palmer, R. Patel, J. Patience, M. D. Perrin, L. A. Poyneer, A. Rajan, J. Rameau, F. T. Rantakyrö, D. Savransky, A. Sivaramakrishnan, I. Song, R. Soummer, S. Thomas, G. Vasisht, D. Vega, J. K. Wallace, K. Ward-Duong, S. J. Wiktorowicz, and **S. G. Wolff** 2016. "The Orbit and Transit Prospects for β Pictoris b Constrained with One Milliarcsecond Astrometry." AJ 152, 97.

Esposito, T. M., M. P. Fitzgerald, J. R. Graham, P. Kalas, E. J. Lee, E. Chiang, G. Duchêne, J. Wang, M. A. Millar-Blanchaer, E. Nielsen, S. M. Ammons, S. Bruzzone, R. J. De Rosa, Z. H. Draper, B. Macintosh, F. Marchis, S. A. Metchev, M. Perrin, L. Pueyo, A. Rajan, F. T. Rantakyrö, D. Vega, and **S. Wolff** 2016. "Bringing 'The Moth' to Light: A Planet-sculpting Scenario for the HD 61005 Debris Disk." AJ 152, 85.

Konopacky, Q. M., J. Rameau, G. Duchêne, J. C. Filippazzo, P. A. Giorla Godfrey, C. Marois, E. L. Nielsen, L. Pueyo, R. R. Rafikov, E. L. Rice, J. J. Wang, S. M. Ammons, V. P. Bailey, T. S. Barman, J. Bulger, S. Bruzzone, J. K. Chilcote, T. Cotten, R. I. Dawson, R. J. De Rosa, R. Doyon, T. M. Esposito, M. P. Fitzgerald, K. B. Follette, S. Goodsell, J. R. Graham, A. Z. Greenbaum, P. Hibon, L.-W. Hung, P. Ingraham, P. Kalas, D. Lafrenière, J. E. Larkin, B. A. Macintosh, J. Maire, F. Marchis, M. S. Marley, B. C. Matthews, S. Metchev, M. A. Millar-Blanchaer, R. Oppenheimer, D. W. Palmer, J. Patience, M. D. Perrin, L. A. Poyneer, A. Rajan, F. T. Rantakyrö, D. Savransky, A. C. Schneider, A. Sivaramakrishnan, I. Song, R. Soummer, S. Thomas, J. K. Wallace, K. Ward-Duong, S. J. Wiktorowicz, and **S. G. Wolff** 2016. "Discovery of a Substellar Companion to the Nearby Debris Disk Host HR 2562." ApJL 829, L4.

Draper, Z. H., G. Duchêne, M. A. Millar-Blanchaer, B. C. Matthews, J. J. Wang,

P. Kalas, J. R. Graham, D. Padgett, S. M. Ammons, J. Bulger, C. Chen, J. K. Chilcote, R. Doyon, M. P. Fitzgerald, K. B. Follette, B. Gerard, A. Z. Greenbaum, P. Hibon, S. Hinkley, B. Macintosh, P. Ingraham, D. Lafrenière, F. Marchis, C. Marois, E. L. Nielsen, R. Oppenheimer, R. Patel, J. Patience, M. Perrin, L. Pueyo, A. Rajan, J. Rameau, A. Sivaramakrishnan, D. Vega, K. Ward-Duong, and **S. G. Wolff** 2016. "The Peculiar Debris Disk of HD 111520 as Resolved by the Gemini Planet Imager." ApJ 826, 147.

Rameau, J., E. L. Nielsen, R. J. De Rosa, S. C. Blunt, J. Patience, R. Doyon, J. R. Graham, D. Lafrenière, B. Macintosh, F. Marchis, V. Bailey, J. K. Chilcote, G. Duchene, T. M. Esposito, L.-W. Hung, Q. M. Konopacky, J. Maire, C. Marois, S. Metchev, M. D. Perrin, L. Pueyo, A. Rajan, D. Savransky, J. J. Wang, K. Ward-Duong, **S. G. Wolff**, S. M. Ammons, P. Hibon, P. Ingraham, P. Kalas, K. M. Morzinski, R. Oppenheimer, F. T. Rantakyearö, and S. Thomas 2016. "Constraints on the Architecture of the HD 95086 Planetary System with the Gemini Planet Imager." ApJL 822, L29.

Mazoyer, J., A. Boccaletti, Eacute;. Choquet, M. D. Perrin, L. Pueyo, J.-C. Augereau, A.-M. Lagrange, J. Debes, and **S. G. Wolff** 2016. "A Symmetric Inner Cavity in the HD 141569A Circumstellar Disk." ApJ 818, 150.

Choquet, É., M. D. Perrin, C. H. Chen, R. Soummer, L. Pueyo, J. B. Hagan, E. Gofas-Salas, A. Rajan, D. A. Golimowski, D. C. Hines, G. Schneider, J. Mazoyer, J.-C. Augereau, J. Debes, C. C. Stark, **S. Wolff**, M. N'Diaye, and K. Hsiao 2016. "First Images of Debris Disks around TWA 7, TWA 25, HD 35650, and HD 377." ApJL 817, L2.

Hung, L.-W., G. Duchêne, P. Arriaga, M. P. Fitzgerald, J. Maire, C. Marois, M. A. Millar-Blanchaer, S. Bruzzone, A. Rajan, L. Pueyo, P. G. Kalas, R. J. De Rosa, J. R. Graham, Q. Konopacky, **S. G. Wolff**, S. M. Ammons, C. H. Chen, J. K. Chilcote, Z. H. Draper, T. M. Esposito, B. Gerard, S. Goodsell, A. Greenbaum, P. Hibon, S. Hinkley, B. Macintosh, F. Marchis, S. Metchev, E. L. Nielsen, R. Oppenheimer, J. L. Patience, M. D. Perrin, F. T. Rantakyrö, A. Sivaramakrishnan, J. J. Wang, K. Ward-Duong, and S. J. Wiktorowicz 2015. "First Scattered-light Image of the Debris Disk around HD 131835 with the Gemini Planet Imager." ApJL 815, L14.

De Rosa, R. J., E. L. Nielsen, S. C. Blunt, J. R. Graham, Q. M. Konopacky, C. Marois, L. Pueyo, J. Rameau, D. M. Ryan, J. J. Wang, V. Bailey, A. Chontos, D. C. Fabrycky, K. B. Follette, B. Macintosh, F. Marchis, S. M. Ammons,

P. Arriaga, J. K. Chilcote, T. H. Cotten, R. Doyon, G. Duchêne, T. M. Esposito, M. P. Fitzgerald, B. Gerard, S. J. Goodsell, A. Z. Greenbaum, P. Hibon, P. Ingraham, M. Johnson-Groh, P. G. Kalas, D. Lafrenière, J. Maire, S. Metchev, M. A. Millar-Blanchaer, K. M. Morzinski, R. Oppenheimer, R. I. Patel, J. L. Patience, M. D. Perrin, A. Rajan, F. T. Rantakyrö, J.-B. Ruffio, A. C. Schneider, A. Sivaramakrishnan, I. Song, D. Tran, G. Vasisht, K. Ward-Duong, and **S. G. Wolff** 2015. "Astrometric Confirmation and Preliminary Orbital Parameters of the Young Exoplanet 51 Eridani b with the Gemini Planet Imager." ApJL 814, L3.

Kalas, P. G., A. Rajan, J. J. Wang, M. A. Millar-Blanchaer, G. Duchene, C. Chen, M. P. Fitzgerald, R. Dong, J. R. Graham, J. Patience, B. Macintosh, R. Murray-Clay, B. Matthews, J. Rameau, C. Marois, J. Chilcote, R. J. De Rosa, R. Doyon, Z. H. Draper, S. Lawler, S. M. Ammons, P. Arriaga, J. Bulger, T. Cotten, K. B. Follette, S. Goodsell, A. Greenbaum, P. Hibon, S. Hinkley, L.-W. Hung, P. Ingraham, Q. Konapacky, D. Lafreniere, J. E. Larkin, D. Long, J. Maire, F. Marchis, S. Metchev, K. M. Morzinski, E. L. Nielsen, R. Oppenheimer, M. D. Perrin, L. Pueyo, F. T. Rantakyrö, J.-B. Ruffio, L. Saddlemyer, D. Savransky, A. C. Schneider, A. Sivaramakrishnan, R. Soummer, I. Song, S. Thomas, G. Vasisht, K. Ward-Duong, S. J. Wiktorowicz, and **S. G. Wolff** 2015. "Direct Imaging of an Asymmetric Debris Disk in the HD 106906 Planetary System." ApJ 814, 32.

Macintosh, B., J. R. Graham, T. Barman, R. J. De Rosa, Q. Konopacky, M. S. Marley, C. Marois, E. L. Nielsen, L. Pueyo, A. Rajan, J. Rameau, D. Saumon, J. J. Wang, J. Patience, M. Ammons, P. Arriaga, E. Artigau, S. Beckwith, J. Brewster, S. Bruzzone, J. Bulger, B. Burningham, A. S. Burrows, C. Chen, E. Chiang, J. K. Chilcote, R. I. Dawson, R. Dong, R. Doyon, Z. H. Draper, G. Duchêne, T. M. Esposito, D. Fabrycky, M. P. Fitzgerald, K. B. Follette, J. J. Fortney, B. Gerard, S. Goodsell, A. Z. Greenbaum, P. Hibon, S. Hinkley, T. H. Cotten, L.-W. Hung, P. Ingraham, M. Johnson-Groh, P. Kalas, D. Lafreniere, J. E. Larkin, J. Lee, M. Line, D. Long, J. Maire, F. Marchis, B. C. Matthews, C. E. Max, S. Metchev, M. A. Millar-Blanchaer, T. Mittal, C. V. Morley, K. M. Morzinski, R. Murray-Clay, R. Oppenheimer, D. W. Palmer, R. Patel, M. D. Perrin, L. A. Poyneer, R. R. Rafikov, F. T. Rantakyrö, E. L. Rice, P. Rojo, A. R. Rudy, J.-B. Ruffio, M. T. Ruiz, N. Sadakuni, L. Saddlemyer, M. Salama, D. Savransky, A. C. Schneider, A. Sivaramakrishnan, I. Song, R. Soummer, S. Thomas,

G. Vasisht, J. K. Wallace, K. Ward-Duong, S. J. Wiktorowicz, **S. G. Wolff**, and B. Zuckerman 2015. "Discovery and spectroscopy of the young jovian planet 51 Eri b with the Gemini Planet Imager." Science 350, 64-67.

Wang, J. J., J. R. Graham, L. Pueyo, E. L. Nielsen, M. Millar-Blanchaer, R. J. De Rosa, P. Kalas, S. M. Ammons, J. Bulger, A. Cardwell, C. Chen, E. Chiang, J. K. Chilcote, R. Doyon, Z. H. Draper, G. Duchêne, T. M. Esposito, M. P. Fitzgerald, S. J. Goodsell, A. Z. Greenbaum, M. Hartung, P. Hibon, S. Hinkley, L.-W. Hung, P. Ingraham, J. E. Larkin, B. Macintosh, J. Maire, F. Marchis, C. Marois, B. C. Matthews, K. M. Morzinski, R. Oppenheimer, J. Patience, M. D. Perrin, A. Rajan, F. T. Rantakyrö, N. Sadakuni, A. Serio, A. Sivaramakrishnan, R. Soummer, S. Thomas, K. Ward-Duong, S. J. Wiktorowicz, and **S. G. Wolff** 2015. "Gemini Planet Imager Observations of the AU Microscopii Debris Disk: Asymmetries within One Arcsecond." ApJL 811, L19.

Millar-Blanchaer, M. A., J. R. Graham, L. Pueyo, P. Kalas, R. I. Dawson, J. Wang, M. D. Perrin, D.-S. moon, B. Macintosh, S. M. Ammons, T. Barman, A. Cardwell, C. H. Chen, E. Chiang, J. Chilcote, T. Cotten, R. J. De Rosa, Z. H. Draper, J. Dunn, G. Duchêne, T. M. Esposito, M. P. Fitzgerald, K. B. Follette, S. J. Goodsell, A. Z. Greenbaum, M. Hartung, P. Hibon, S. Hinkley, P. Ingraham, R. Jensen-Clem, Q. Konopacky, J. E. Larkin, D. Long, J. Maire, F. Marchis, M. S. Marley, C. Marois, K. M. Morzinski, E. L. Nielsen, D. W. Palmer, R. Oppenheimer, L. Poyneer, A. Rajan, F. T. Rantakyrö, J.-B. Ruffio, N. Sadakuni, L. Saddlemyer, A. C. Schneider, A. Sivaramakrishnan, R. Soummer, S. Thomas, G. Vasisht, D. Vega, J. K. Wallace, K. Ward-Duong, S. J. Wiktorowicz, and **S. G. Wolff** 2015. "Beta Pictoris' Inner Disk in Polarized Light and New Orbital Parameters for Beta Pictoris b." ApJ 811, 18.

Perrin, M. D., G. Duchene, M. Millar-Blanchaer, M. P. Fitzgerald, J. R. Graham, S. J. Wiktorowicz, P. G. Kalas, B. Macintosh, B. Bauman, A. Cardwell, J. Chilcote, R. J. De Rosa, D. Dillon, R. Doyon, J. Dunn, D. Erikson, D. Gavel, S. Goodsell, M. Hartung, P. Hibon, P. Ingraham, D. Kerley, Q. Konapacky, J. E. Larkin, J. Maire, F. Marchis, C. Marois, T. Mittal, K. M. Morzinski, B. R. Oppenheimer, D. W. Palmer, J. Patience, L. Poyneer, L. Pueyo, F. T. Rantakyrö, N. Sadakuni, L. Saddlemyer, D. Savransky, R. Soummer, A. Sivaramakrishnan, I. Song, S. Thomas, J. K. Wallace, J. J. Wang, and **S. G. Wolff** 2015. "Polarimetry with the Gemini Planet Imager: Methods, Performance at First Light,

and the Circumstellar Ring around HR 4796A." ApJ 799, 182.

Chilcote, J., T. Barman, M. P. Fitzgerald, J. R. Graham, J. E. Larkin, B. Macintosh, B. Bauman, A. S. Burrows, A. Cardwell, R. J. De Rosa, D. Dillon, R. Doyon, J. Dunn, D. Erikson, D. Gavel, S. J. Goodsell, M. Hartung, P. Hibon, P. Ingraham, P. Kalas, Q. Konopacky, J. Maire, F. Marchis, M. S. Marley, C. Marois, M. Millar-Blanchaer, K. Morzinski, A. Norton, R. Oppenheimer, D. Palmer, J. Patience, M. Perrin, L. Poyneer, L. Pueyo, F. T. Rantakyrö, N. Sadakuni, L. Saddlemyer, D. Savransky, A. Serio, A. Sivaramakrishnan, I. Song, R. Soummer, S. Thomas, J. K. Wallace, S. Wiktorowicz, and **S. Wolff** 2015. "The First H-band Spectrum of the Giant Planet β Pictoris b." ApJL 798, L3.

Ingraham, P., M. S. Marley, D. Saumon, C. Marois, B. Macintosh, T. Barman, B. Bauman, A. Burrows, J. K. Chilcote, R. J. De Rosa, D. Dillon, R. Doyon, J. Dunn, D. Erikson, M. P. Fitzgerald, D. Gavel, S. J. Goodsell, J. R. Graham, M. Hartung, P. Hibon, P. G. Kalas, Q. Konopacky, J. A. Larkin, J. Maire, F. Marchis, J. McBride, M. Millar-Blanchaer, K. M. Morzinski, A. Norton, R. Oppenheimer, D. W. Palmer, J. Patience, M. D. Perrin, L. A. Poyneer, L. Pueyo, F. Rantakyrö, N. Sadakuni, L. Saddlemyer, D. Savransky, R. Soummer, A. Sivaramakrishnan, I. Song, S. Thomas, J. K. Wallace, S. J. Wiktorowicz, and **S. G. Wolff** 2014. "Gemini Planet Imager Spectroscopy of the HR 8799 Planets c and d." ApJL 794, L15.

Macintosh, B., J. R. Graham, P. Ingraham, Q. Konopacky, C. Marois, M. Perrin, L. Poyneer, B. Bauman, T. Barman, A. S. Burrows, A. Cardwell, J. Chilcote, R. J. De Rosa, D. Dillon, R. Doyon, J. Dunn, D. Erikson, M. P. Fitzgerald, D. Gavel, S. Goodsell, M. Hartung, P. Hibon, P. Kalas, J. Larkin, J. Maire, F. Marchis, M. S. Marley, J. McBride, M. Millar-Blanchaer, K. Morzinski, A. Norton, B. R. Oppenheimer, D. Palmer, J. Patience, L. Pueyo, F. Rantakyro, N. Sadakuni, L. Saddlemyer, D. Savransky, A. Serio, R. Soummer, A. Sivaramakrishnan, I. Song, S. Thomas, J. K. Wallace, S. Wiktorowicz, and **S. Wolff** 2014. "First light of the Gemini Planet Imager." Proceedings of the National Academy of Science 111, 12661-12666.

Reggiani, M., S. P. Quanz, M. R. Meyer, L. Pueyo, O. Absil, A. Amara, G. Anglada, H. Avenhaus, J. H. Girard, C. Carrasco Gonzalez, J. Graham, D. Mawet, F. Meru, J. Milli, M. Osorio, **S. Wolff**, and J.-M. Torrelles 2014. "Discovery of a Companion Candidate in the HD 169142 Transition Disk and the Possibility of Multiple

Planet Formation." ApJL 792, L23.

Macintosh, B. A., A. Anthony, J. Atwood, B. Bauman, A. Cardwell, K. Caputa, J. Chilcote, R. J. De Rosa, D. Dillon, R. Doyon, J. Dunn, D. Erickson, M. P. Fitzgerald, D. T. Gavel, R. Galvez, S. Goodsell, J. Graham, A. Z. Greenbaum, M. Hartung, P. Hibon, P. Ingraham, D. Kerley, Q. Konopacky, K. Labrie, J. Larkin, J. Maire, F. Marchis, C. Marois, M. Millar-Blanchaer, K. Morzinski, A. Nunez, R. Oppenheimer, D. Palmer, J. Pazder, M. Perrin, L. A. Poyneer, L. Pueyo, C. Quiroz, F. Rantakyro, V. Reshetov, L. Saddlemyer, N. Sadakuni, D. Savransky, A. Serio, A. Sivaramakrishnan, M. Smith, R. Soummer, S. Thomas, J. K. Wallace, J. Wang, J. Weiss, S. Wiktorowicz, and **S. G. Wolff** 2014. "The Gemini planet imager: first light and commissioning." Proc. SPIE 9148, 91480J.

Greenbaum, A. Z., A. Cheetham, A. Sivaramakrishnan, P. Tuthill, B. Norris, L. Pueyo, N. Sadakuni, F. Rantakyrö, P. Hibon, S. Goodsell, M. Hartung, A. Serio, A. Cardwell, L. Poyneer, B. Macintosh, D. Savransky, M. D. Perrin, **S. Wolff**, P. Ingraham, and S. Thomas 2014. "Gemini planet imager observational calibrations X: non-redundant masking on GPI." Proc. SPIE 9147, 91477B.

Maire, J., P. J. Ingraham, R. J. De Rosa, M. D. Perrin, A. Rajan, D. Savransky, J. J. Wang, J.-B. Ruffio, **S. G. Wolff**, J. K. Chilcote, R. Doyon, J. R. Graham, A. Z. Greenbaum, Q. M. Konopacky, J. E. Larkin, B. A. Macintosh, C. Marois, M. Millar-Blanchaer, J. Patience, L. A. Pueyo, A. Sivaramakrishnan, S. J. Thomas, and J. L. Weiss 2014. "Gemini planet imager observational calibrations VI: photometric and spectroscopic calibration for the integral field spectrograph." Proc. SPIE 9147, 914785.

Ingraham, P., J.-B. Ruffio, M. D. Perrin, **S. G. Wolff**, Z. H. Draper, J. Maire, F. Marchis, and V. Fesquet 2014. "Gemini planet imager observational calibrations III: empirical measurement methods and applications of high-resolution microlens PSFs." Proc. SPIE 9147, 91477K.

Draper, Z. H., C. Marois, **S. Wolff**, M. Perrin, P. J. Ingraham, J.-B. Ruffio, F. T. Rantakyro, M. Hartung, and S. J. Goodsell 2014. "Gemini planet imager observational calibrations IX: least-squares inversion flux extraction." Proc. SPIE 9147, 91474Z.

Perrin, M. D., J. Maire, P. Ingraham, D. Savransky, M. Millar-Blanchaer, **S. G. Wolff**, J.-B. Ruffio, J. J. Wang, Z. H. Draper, N. Sadakuni, C. Marois, A. Rajan, M. P. Fitzgerald, B. Macintosh, J. R. Graham, R. Doyon, J. E. Larkin, J. K. Chilcote, S. J. Goodsell, D. W. Palmer, K. Labrie, M. Beaulieu, R. J. De Rosa, A. Z. Green-

baum, M. Hartung, P. Hibon, Q. Konopacky, D. Lafreniere, J.-F. Lavigne, F. Marchis, J. Patience, L. Pueyo, F. T. Rantakyrö, R. Soummer, A. Sivaramakrishnan, S. Thomas, K. Ward-Duong, and S. Wiktorowicz 2014. "Gemini Planet Imager observational calibrations I: Overview of the GPI data reduction pipeline." Proc. SPIE 9147, 91473J.

Rodney, S. A., A. G. Riess, L.-G. Strolger, T. Dahlen, O. Graur, S. Casertano, M. E. Dickinson, H. C. Ferguson, P. Garnavich, B. Hayden, S. W. Jha, D. O. Jones, R. P. Kirshner, A. M. Koekemoer, C. McCully, B. Mobasher, B. Patel, B. J. Weiner, S. B. Cenko, K. I. Clubb, M. Cooper, A. V. Filippenko, T. F. Frederiksen, J. Hjorth, B. Leibundgut, T. Matheson, H. Nayyeri, K. Penner, J. Trump, J. M. Silverman, V. U, K. Azalee Bostroem, P. Challis, A. Rajan, **S. Wolff**, S. M. Faber, N. A. Grogin, and D. Kocevski 2014. "Type Ia Supernova Rate Measurements to Redshift 2.5 from CANDELS: Searching for Prompt Explosions in the Early Universe." AJ 148, 13.

Soummer, R., M. D. Perrin, L. Pueyo, Eacute;. Choquet, C. Chen, D. A. Golimowski, J. Brendan Hagan, T. Mittal, M. Moerchen, M. N'Diaye, A. Rajan, **S. Wolff**, J. Debes, D. C. Hines, and G. Schneider 2014. "Five Debris Disks Newly Revealed in Scattered Light from the Hubble Space Telescope NICMOS Archive." ApJL 786, L23.

Perrin, M. D., E. Choquet, C. Chen, J. Debes, D. Golimowski, J. B. Hagan, D. C. Hines, T. Mittal, M. Moerchen, M. N'Diaye, L. Pueyo, I. N. Reid, G. Schneider, **S. Wolff**, and R. Soummer 2014. "Newly Seen Debris Disks from the HST NICMOS Archive." Exploring the Formation and Evolution of Planetary Systems 299, 354-355.

Duchêne, G., K. Stapelfeldt, A. Isella, M. Perrin, F. Ménard, D. Padgett, C. Pinte, **S. Wolff**, J. Krist, A. Ghez, and Q. Konopacky 2014. Panchromatic imaging and modeling of SSTtau J042021+281349: "A new prototypical edge-on protoplanetary disk." Exploring the Formation and Evolution of Planetary Systems 299, 111-112.

Stapelfeldt, K. R., G. Duchêne, M. Perrin, **S. Wolff**, J. E. Krist, D. L. Padgett, F. Ménard, and C. Pinte 2014. "HST Imaging of New Edge-on Circumstellar Disks in Nearby Star-forming Regions." Exploring the Formation and Evolution of Planetary Systems 299, 99-103.

Presentations

Wolff, S. G., Menard, F., Caceres, C., and Lefevre, C. 2017. Placing Limits on the Mass of the DH Tau b Circumplanetary Disk. American Astronomical Society Meeting Abstracts, 229, 345.13

Wolff, S., M. D. Perrin, J. Mazoyer, E. Choquet, R. Soummer, B. Ren, L. Pueyo, J. H. Debes, G. Duchene, C. Pinte, and F. Menard 2016. "An MCMC Circumstellar Disks Modeling Tool." American Astronomical Society Meeting Abstracts 227, 309.05.

Wolff, S. G., M. Perrin, J. Wang,J. R. Graham,L. Pueyo, M. A. Millar-Blanchaer, P. Kalas, E. L. Nielsen, and the GPIES Consortium 2015. "Gemini Planet Imager Observations of the Protoplanetary Disk around the Young Star PDS 66." In the Spirit of Lyot.

Wolff, S., M. D. Perrin, J. Wang, J. R. Graham, L. Pueyo, M. Millar-Blanchaer, P. Kalas, and Gpies Team 2015. "PDS 66 Resolved in Polarimetry with the Gemini Planet Imager." American Astronomical Society Meeting Abstracts 225, 349.05.

Wolff, S., M. D. Perrin, K. R. Stapelfeldt, G. Duchene, F. Menard, D. Padgett, and C. Pinte 2014. "HST Scattered Light Imaging and Modeling of the Edge-On Protoplanetary Disk ESO Halpha 569." American Astronomical Society Meeting Abstracts #223 223, 350.17.

Wolff, S., R. Murray-Clay, and R. Dawson 2011. "Investigating the Dynamical History of the Solar System." Bulletin of the American Astronomical Society 43, 156.10.

Wolff, S., L. Strolger, A. Pease, and A. Gott 2010. "Determining The Progenitors Of Type Ia Supernovae From Their Environments." Bulletin of the American Astronomical Society 42, 430.15.